Study of corona discharges on VHF antennas caused by a natural electrostatic field

Mingtian Wang

To cite this version:

Mingtian Wang. Study of corona discharges on VHF antennas caused by a natural electrostatic field. Electromagnetism. Université Paul Sabatier - Toulouse III, 2014. English. NNT : . tel-00976587

HAL Id: tel-00976587
https://theses.hal.science/tel-00976587

Submitted on 10 Apr 2014

Université
de Toulouse

THÈSE

En vue de l'obtention du

DOCTORAT DE L'UNIVERSITÉ DE TOULOUSE

Délivré par :

Université Toulouse 3 Paul Sabatier (UT3 Paul Sabatier)

Présentée et soutenue par :
Mingtian WANG
le jeudi 03 avril 2014 à 10h30

Titre :

Etude des décharges corona sur des antennes VHF soumises à un champ électrostatique naturel
Study of corona discharges on VHF antennas caused by a natural electrostatic field

---

École doctorale et discipline ou spécialité :
ED GEET : Électromagnétisme et Systèmes Haute Fréquence

Unité de recherche :
ENAC, TELECOM/EMA UPS, LAPLACE, GREPHE

Directeur(s) de Thèse :
M. Jean-Pierre BOEUF
M. Alexandre CHABORY

Jury :
M. Olivier PASCAL - Président du jury
M. Alain REINEIX - Rapporteur
M. Philippe BESNIER - Rapporteur
M. Laïfa BOUFENDI - Examinateur
M. Jean-Pierre BOEUF - Co-Directeur de Thèse
M. Alexandre CHABORY - Co-Directeur de Thèse

Avant propos

Cette thèse a été co-financée par:

- La Direction de la Technique et de l'Innovation de la Direction Générale de l'Aviation Civile (DGAC-DTI)

- La région Midi-Pyrénées

- Le Pôle de Recherche et d'Enseignement Supérieur (PRES) de l'Université de Toulouse

Remerciements

Avant toute chose, je remercie la Direction de la Technique et de l'Innovation de la Direction Générale de l'Aviation civile (DGAC-DTI), la région Midi-Pyrénées et l'Université de Toulouse pour avoir financé cette thèse.

Ce travail a été réalisé au sein du groupe de recherche Électromagnétisme et Antennes (EMA) du Laboratoire de TELECOM de l'École Nationale de l'Aviation Civile (ENAC) sous la direction de Monsieur Alexandre CHABORY en collaboration avec le Laboratoire Plasma et Conversion d'Energie (LAPLACE) de l'Université Paul Sabatier sous la direction de Monsieur Jean-Pierre BOEUF.

Je tiens ici à remercier très chaleureusement Monsieur Alexandre CHABORY, enseignant-chercheur à l'ENAC, et Monsieur Jean-Pierre BOEUF, directeur de recherche au LAPLACE qui, encadrant ce travail, ont partagé avec moi leur immense savoir scientifique, et m'ont imprégné de leur patience, de leur rigueur et de leur curiosité. C'est particulièrement le cas pour Monsieur CHABORY. C'est lui qui a dû me supporter le plus grand nombre d'heures. Ses idées brillantes m'ont été d'un très grand secours au long de mon travail. De plus, mon manuscrit n'aurait pas eu la même qualité sans son aide. Je remercie aussi Monsieur BOEUF pour son aide pour améliorer mon manuscrit et pour son immense connaissance dans le domaine des plasmas, sur lequel je savais peu de chose avant ce travail.

J'adresse mes sincères remerciements à Monsieur Alain REINEX, Directeur de Recherche

de l'institut XLIM de l'Université de Limoges, et à Monsieur Philippe BESNIER, Directeur de Recherche de l'Institut d'Electronique et de Télécommunications de Rennes (IETR), pour avoir bien voulu accepter d'être rapporteur de ce manuscrit.
Je remercie également Monsieur Olivier PASCAL, Professeur de l'Université Paul Sabatier, d'avoir présidé le jury.
Que Monsieur Laïfa BOUFENDI, Professeur au laboratoire GREMI de l'Université d'Orléans, soit chaleureusement remercié pour avoir accepté de faire partie du jury.

Je voudrais remercier Monsieur Bernard SOUNY, ancien chef du laboratoire de l'ENAC. Une grande partie de mes recherches se sont basées sur ses travaux antérieurs.
Je remercie sincèrement Monsieur Philippe ARTAUT, chef de la subdivision Électromagnétisme et Signal (ELS) du département Sciences et Ingénierie de la Navigation Aérienne (SINA) de l'ENAC, pour son aide sur les mesures effectuées sur le pylône de Champcueil.
Monsieur Thierry CALLEGARI du LAPLACE a participé aux mesures effectuées au LAPLACE. Je l'en remercie très chaleureusement.
Mes remerciements vont aussi à l'ensemble du groupe EMA, qui m'a apporté un soutien sans faille.

Contents

Introduction

1 Context

1.1 Aeronautical telecommunications

In civil aviation, communications between airplane pilots and air traffic controllers are of primary importance to guarantee the flight safety. Voices and digital data are transmitted *via* radiocommunication systems, mainly in the VHF aeronautical band [1]. Ground stations equipped with VHF antennas are used to receive the radio signals from the pilots and transmit them to the air traffic controllers, and *vice versa*.

In radiocommunications, the signal to be transmitted is modulated and then radiated by the transmitting antenna. It travels through space, is captured by the receiving antenna, and is at last demodulated. The link budget and the radio horizon limit the range of VHF aeronautical communications to few hundreds kilometers [2]. Besides, there are many physical phenomena that may alter the radio signal while propagating through space. VHF aeronautical telecommunication signals may notably be interfered by signals radiated by other electronic devices or by natural sources of noise.

A particular interference noise has been observed at some ground stations operated by the French civil aviation authority (DGAC). This interference noise, that can sometimes disrupt dialogues between pilots and air traffic controllers, has been experienced many times, notably at Champcueil near Paris. Identifying the origin of this interference and studying its properties are essential tasks.

Measurements have been performed to determine the origin of these interferences. They have shown that the origin is probably electrostatic discharges, particularly corona discharges caused by a strong local electrostatic field that may be explained by weather conditions [3, 4].

1.2 Corona discharges and their effects on VHF communications

Corona discharges are a type of electrostatic discharges that occur at places where there is a strong non-uniform electrostatic field [5, 6]. The places where corona discharges usually occur include sharp edges, sharp tips, and thin lines [5, 7]. An example of corona discharges is the St. Elmo's fire appearing on top of the masts of sailing ships during thunderstorms.

Interferences due to corona discharges have been observed in several domains, such as high-voltage transmission lines [8], in-flight aircrafts [9], ground pylons for television broadcasting [10]. Compared with other types of discharges, e.g. electrostatic discharges (ESD) and lightning, less literature exists on corona interferences. In the following parts, the existing cases are listed and the way they interfere in VHF communications is explained.

Corona discharges often occur on high-voltage transmission lines because of the relatively thin radius of the lines and their high potential. This phenomenon is studied by many authors [8, 11, 12, 13, 14, 15] because they cause power losses. Besides the power losses, corona discharges also generate a wide band interference (from DC to VHF) [8, 13, 16, 17].

Corona discharges are also well-studied for the onboard radio systems of high-speed aircrafts [7, 9]. In the 1940s, interferences on the signals of radiocommunication and navigation systems have been observed [18]. Measurements have been performed and they have shown that, while flying, aircrafts are charged by the triboelectric effect when they are struck by precipitation particles [18, 19, 20, 21, 22, 23]. The potential of the aircraft is increased to a high level and the electrostatic field can be very strong. Hence, corona discharges occur at the onboard antennas and at the other extremities of the aircraft. These studies have led to the invention of the wick discharger that is mounted on aircrafts to reduce the interference level [21]. More recently, research works have focused on corona discharges on composite aircrafts [24].

Corona discharge interferences are also experienced on the ground, more particularly on pylons. These corona discharges introduce a wide band interference so that television broadcasting and amateur radio are impaired [10, 25, 26]. Specific arrangements of the pylons and antennas have been proposed to reduce the interference level [10, 25].

For the ground stations of civil aviation radiocommunications, the antennas that are impaired by electrostatic discharges are mounted on top or on the upper part of pylons (tens of meters high). Corona discharges on the pylon are probably caused by a strong electrostatic field of natural origin. To develop a model to predict quantitatively the interference level observed at the VHF antennas would be helpful. This is the topic of this Ph.D. thesis.

2 Objective

The main objective of this thesis is to develop a model to predict quantitatively the interference level induced by corona discharges at VHF antennas for a known pylon geometry and ambient electrostatic field.

In order to achieve this objective, we need to realize the following goals:

- to prove that corona discharges are the origin of the interferences observed at the ground stations;
- to localize where corona discharges occur on pylons;
- to study the characteristics of corona discharges and to find a model that can represent their radiation in the VHF band;
- to evaluate the interference level introduced by corona discharges at the antenna ports, and compare the results with the measurements performed at the Champcueil ground station.

3 Contributions

To achieve the objectives, the work has been divided into different parts. For each part, we develop models based on the physics with consistent hypotheses that are numerically tested. During this process, the following contributions are proposed:

- We compare the measurements of both the ambient electrostatic field and the VHF interferences to confirm the origin of the interference noise.
- We localize the places on the pylon where corona discharges most likely occur *via* an electrostatic simulation based on the finite elements method. The electrostatic simulation estimates the electrostatic field around the pylon and the antennas for a given ambient electrostatic field. From the simulation results, a criterion is determined to evaluate where corona discharges most likely occur.
- We propose and validate an elementary dipole model to represent the radiation of corona discharges in the frequency domain. The amplitude of the elementary

dipole is estimated by means of a deterministic and a statistical approaches according to the characteristics of corona discharges.

- We evaluate the interference levels introduced by corona discharges at the antenna ports by means of simulations in the frequency domain based on the method of the moments. The simulation results are compared with the measurement results collected at the Champcueil ground station.

4 Outline

This Ph.D. thesis is organized as follows:

Chapter 1 describes the interference phenomenon and its origin. At first, we present the civil aviation telecommunication system. Then the interference phenomenon is described. Its possible origins are listed and analyzed one by one for the Champcueil case. To confirm the analysis, simultaneous measurements of the ambient electrostatic fields and the VHF interferences are presented. As a result, the origin of the interferences is identified.

Chapter 2 presents the mechanism and characteristics of corona discharges. The differences between positive and negative discharges are explained. Some essential characteristics of corona discharges, such as the pulse form, the pulse amplitude, and the repetition rate are listed for both types of discharges.

Chapter 3 presents the electrostatic simulations to localize the places where corona discharges may occur. At first, the basic equations governing corona discharge ignition and the numerical method for the electrostatic simulations are presented. Then, we make some simplifications to render the problem amenable by the Finite elements method. At last, for the Champcueil case, the electrostatic field around the pylon is evaluated *via* electrostatic simulations, and a criterion to determine where corona discharges most likely occur is proposed.

Chapter 4 presents the model used to represent corona discharges for the simulations in the frequency domain. An elementary dipole model is proposed. Its capability to represent the radiation of corona discharges in the VHF aeronautical band is verified. Then, by means of a deterministic and a statistical approaches, we determine the amplitude of the elementary dipole according to the characteristics of corona discharges in the VHF band.

Chapter 5 describes simulations in the frequency domain to evaluate the interference level introduced by corona discharges at the antenna ports. At first, models of antennas are presented and tested to have realistic performances. Secondly, we estimate the interferences introduced by corona discharges for each possible discharge location. Thirdly, we compute the interferences introduced by corona discharges occurring simultaneously in different locations. At last, the model is validated through simulations that are compared with the measurement results collected at the Champcueil station.

Chapter 1

The interference phenomenon and its origin

The aim of this chapter is firstly to describe the interference phenomenon observed at VHF receiving ground stations of civil aviation and secondly to find its origin. At first, the radiocommunication systems used in civil aviation are presented. Then the interference phenomenon is described and analyzed. Possible origins of the interference are examined. Experimental results are shown to confirm the origin at the end of the chapter.

1.1 The civil aviation radiocommunication system

The civil aviation radiocommunication system is used for air traffic control, *i.e.*, transmitting messages and data between aircrafts and the ground. The mainly used frequency band is the VHF band. Other bands are also used such as the UHF band for Search and Rescue, inter-pilots communications, and the HF band for long distance communications.

The International Civil Aviation Organization (ICAO) has published the international standards for civil aviation. Annex 10 Volume 3 defines the technical standards for aeronautical communication systems [1].

1.1.1 VHF aeronautical links

The Very High Frequency (VHF) band is the range of radio frequency from 30 MHz to 300 MHz. In France, VHF civil aviation radiocommunications are between 118MHz and 137MHz. This frequency band is split into narrow-band channels of 25kHz for digital signals and 8.33kHz for analog signals to permit plural simultaneous communications. In this Ph.D. thesis, we note:

- B_{a} the total VHF band used for civil aviation communications;
- B_{c} any voice channel of bandwidth 8.33kHz in B_{a}.

We cite as an example the following channels reserved in France in Table 1.1.

Frequency (MHz)	Functions
118 - 121.4	National and international mobile aeronautical services
121.5	Distress and emergency frequency
121.6 - 121.9916	Groud communications between airports
122 - 123.05	National mobile aeronautical service
123.1	International Search and Rescue frequency
123.15 - 123.4416	National mobile aeronautical service
123.45	Air-air communications
123.4583 - 123.6917	National mobile aeronautical service
123.7- 129.6916	National and international mobile aeronautical services
129.7 - 130.8916	National mobile aeronautical services
130.9 - 131.7166	National and international mobile aeronautical services
131.725	ACARS: Digital data transmission
131.7333 - 136.875	National and international mobile aeronautical services
136.9 - 137	Digital mobile aeronautical services

Table 1.1: Reserved channels in France.

The VHF aeronautical links are used for communications between aircrafts and the ground for distances up to several hundred kilometers (figure 1.1). It can be a transmission of the voice or digital messages. Two systems exist for the transmission of digital messages, namely Aircraft Communications Addressing and Reporting System (ACARS) and VHF Data Link Mode 2 (VDL 2) [1]. Both ACARS and the new generation VDL 2 work in the VHF band between 118MHz and 136.975MHz. The data

transmitted by ACARS and VDL include maintenance data, weather information, air traffic management, etc.
Besides air-ground radiocommunications, other systems of civil aviation also work in the VHF band such as the conventional radio navigation system. This is the case for VOR/DME (VHF Omnidirectional Range and Distance Measuring Equipment). They are assigned radio channels between 108MHz and 117.95MHz.

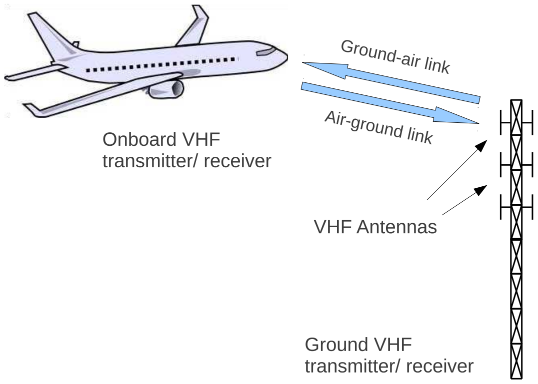

Figure 1.1: Scheme of the air-ground and ground-air link.

1.1.2 Synoptic of the radiocommunications

A synoptic of a radiocommunication is presented in Figure 1.2.

In radiocommunications, the signal to be transmitted (the voice) is modulated by a VHF carrier. Then, the modulated signal is emitted by the transmitting antenna, and it travels through space, where it may be altered by different physical phenomena. After that, it is got by the receiving antenna, and demodulated by the receiver.

For the radiocommunications of civil aviation, the type of modulation used is the amplitude modulation (AM): a high-frequency signal (the carrier) has its amplitude modulated in proportion with the signal to be transmitted (low frequency).

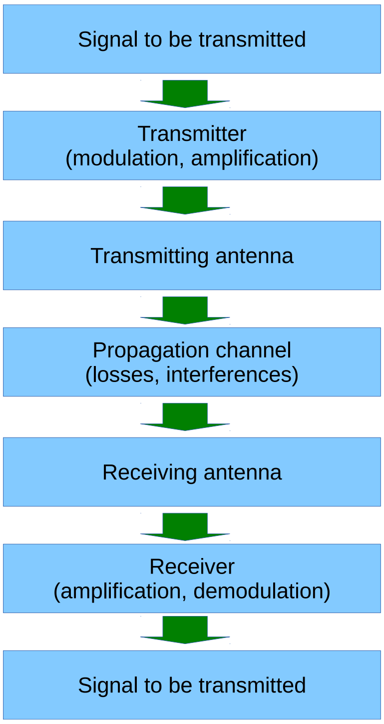

Figure 1.2: Synoptic of a simple radiocommunication system.

The analog AM signal can easily be disturbed by other radiations [27]. Indeed, if there is any interference source in the transmission, a noise always exists after demodulation. Compared with analog signals, digital transmissions are less sensitive to noise.

1.1.3 Transmitter and receiver

With the input data, the transmitter generates the modulated signal. From [1], the recommended radiated power must be such as to provide a field strength of $75\mu\mathrm{V/m}$, which corresponds to a power density of $-139\mathrm{dBm/m}^2$ within the operational coverage of the station [1]. This corresponds to an emitted power of $15 \sim 50\mathrm{W}$ for the transmitter. This can be demonstrated by reminding that the gain G can be expressed as [28]

$$G = \frac{2\pi \|\mathbf{E}\|^2 d^2}{P_{\mathrm{E}} Z_0}, \tag{1.1}$$

where d is the distance between the antenna and the observation point, $\mathbf{E}$ is the electric field at the observation point, Z_0 is the impedance of free space and P_{E} is the input power of the antenna. Therefore P_{E} can be expressed as

$$P_{\mathrm{E}} = \frac{2\pi d^2 \|\mathbf{E}\|^2}{Z_0 G}. \tag{1.2}$$

Applying this expression for an omni-directional antenna ($G = 1$) and a minimal field strength of 75μV/m, the radiated power should be between 8.44 and 15W for a ground station having a coverage range between 300 and 400km. Thus, taking into account the losses (attenuation by atmospheric gases and hydrometeors, ...), an emitted power of $15 \sim 50$W should be enough to guaranty the link.

The receiver recovers the signals contained in the received signal. For civil aviation communications, the important characteristic of the receiver include the frequency stability and the sensitivity.

1.1.4 Antennas

The antennas used at ground stations for civil aviation radiocommunications are VHF antennas with some special requirements:

- Radiation pattern: in order to insure the communications with aircrafts in all directions, the VHF antennas used at ground stations should be omnidirectional in the horizontal plane. Because the aircrafts fly at different altitudes and their distances from the station are different, the antennas should have a large enough beamwidth in the vertical plane. A typical value for our application is a halfpower beamwidth larger than 60 degrees.
- Polarization: the polarization for VHF aeronautical radiocommunications is vertical, thus the antennas are vertically polarized.

1.1.5 Propagation channel

While the signal is propagating in air, different physical phenomena limit the range of the radiocommunication. To study the interference at the ground station, it is necessary to understand the phenomena in the propagation channel. They are presented in this section.

1.1.5.a Maximal propagation range

In the VHF band and for aeronautical radiocommunications, the propagation is line-of-sight. Because of the spherical shape of the Earth, the line-of-sight path is limited by the optical horizon. Thus the aircrafts cannot be too far from the ground station. (see Figure 1.3 (a))

The line-of-sight path is influenced by the atmosphere. Because the refractive index of air n decreases with the altitude h, radiowaves are refracted when they propagate in the atmosphere at different altitudes. The radiowaves thus do not propagate in a straight line, but along a bent path (see Figure 1.3 (b)). That implies that radiowaves propagate further than the geometrical optical horizon, thus the propagation range is not limited by the optical horizon, but by the radio horizon [29].

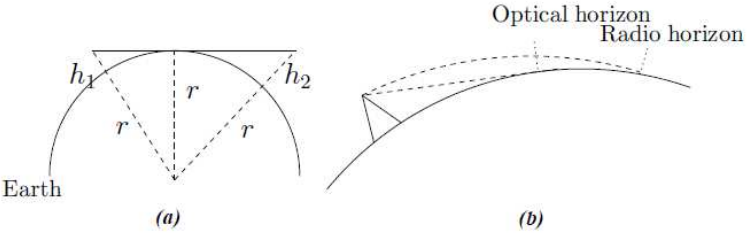

Figure 1.3: Limit of the propagation range: (a) optical horizon; (b) radio horizon.

As shown in Figure 1.3 (a), the optical horizon range d_{opt} can be evaluated from a simple geometric calculation

$$d_{\text{opt}} = \sqrt{(r+h_1)^2 - r^2} + \sqrt{(r+h_2)^2 - r^2} = \sqrt{2rh_1 + h_1^2} + \sqrt{2rh_2 + h_2^2}, \tag{1.3}$$

where r is the radius of the Earth, h_1 and h_2 are the altitudes of the transmitting and receiving antennas, respectively. Because $h_1 \ll r$ and $h_2 \ll r$, we have

$$d_{\mathrm{opt}} \simeq \sqrt{2rh_1} + \sqrt{2rh_2} = \sqrt{2r}(\sqrt{h_1} + \sqrt{h_2}), \tag{1.4}$$

In the standard atmosphere, the calculation of the radio horizon range d_{rad} can be approximately done by pretending the Earth has a fictive radius r' with $r' = 4r/3$ [29]. The radiowaves can then be treated as if they were propagating along straight lines in a homogeneous atmosphere ($\frac{dn}{dh} = 0$) [29]. Hence, the range limit due to the radio horizon can be determined by an equation similar to (1.4), with r replaced by $r' = 4r/3$. Because the Earth radius is $r \simeq 6400\mathrm{km}$, the range limit due to the radio horizon can be calculated as

$$d_{\mathrm{rad}} \simeq 4131(\sqrt{h_1} + \sqrt{h_2}), \tag{1.5}$$

where d_{rad}, h_1 and h_2 are in meters [29]. For example, we consider an antenna of a ground station installed on a 30m-high pylon, and an onboard antenna at a height of 10000m. In this case, the range of the direct link d_{rad} is about 436km.

1.1.5.b Link budget

The link budget is a calculation taking all the gains and losses into account to evaluate the quality of a link. It can be expressed as [2]

$$P_{\mathrm{R}}|_{\mathrm{dBW}} = P_{\mathrm{T}}|_{\mathrm{dBW}} + G_{\mathrm{T}}|_{\mathrm{dBi}} + L_{\mathrm{T}}|_{\mathrm{dBW}} + L_{\mathrm{FS}}|_{\mathrm{dBW}} + G_{\mathrm{R}}|_{\mathrm{dBi}} + L_{\mathrm{R}}|_{\mathrm{dBW}} + L_{\mathrm{M}}|_{\mathrm{dBW}}, \tag{1.6}$$

with the following notations:

- P_{R} received power;
- P_{T} power delivered by the transmitter;
- G_{T} gain of the transmitting antenna;
- G_{R} gain of the receiving antenna;

- L_{T} transmitter losses;
- L_{FS} free space losses;
- L_{R} receiver losses;
- L_{M} other losses (attenuation of hydrometeor, polarization mismatch of antennas, etc).

The free space losses describe the decrease of the signal strength with distance. They can be expressed as

$$L_{\mathrm{FS}}|_{\mathrm{dB}} = 20 \log_{10} \frac{\lambda}{4\pi d}, \tag{1.7}$$

with d the distance from the transmitting antenna, λ the wavelength. For a signal at a frequency of 120MHz ($\lambda = 2.5$m) propagating over 300km, the free space losses are -123dB.

1.1.5.c Multipath

The receiving antenna may receive signals propagating along different paths. This includes the signal along the direct path which is the main one, the signal reflected over the ground or other objects such as buildings, and the signals diffracted by the edges of buildings or other objects. These phenomena are called multipath (see Figure 1.4). Compared with the direct path, the other signals have the same frequency but have different phases and amplitudes.

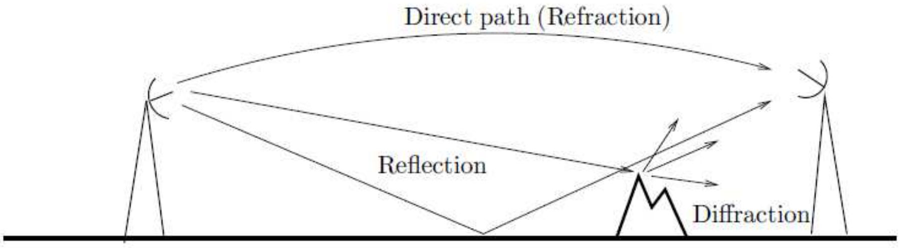

Figure 1.4: Multipath effect.

If there is any large obstructions, such as hills or buildings, between the transmitter and the receiver, the main path (direct path) may be cut off. This phenomenon is called shadowing. In this case, the receiver may still get part of the signal due to diffractions by edges.

1.1.5.d Interference

While the radiowaves propagate in free space, they are perturbed by different sources of interferences, thus the signals received by the receiving antenna become noisy. There are different types of interference sources. Some sources are other electric devices radiating VHF waves [30, 31]. Some natural phenomena also disturb civil aviation communications such as electric discharges. Electrostatic discharges include lightning, arc and corona discharges. They radiate electromagnetic waves in a large frequency band, including the VHF band [9, 32, 33].

The objective of this Ph.D. thesis is to identify and analyze the origin of an interference phenomenon. There are several possible sources that may cause this interference. We will list the possible sources and analyze them in Section 1.3.

1.1.6 Conclusion

The civil aviation communication system has been presented in this section. We have seen that the radiocommunication signals can be disturbed during propagation. In the following section, an interference phenomenon observed in a ground station will be presented.

1.2 Interference phenomenon at the Champcueil station

The interference phenomenon has been observed at different receiving ground stations for civil aviation communications [7]. The phenomenon observed at the ground station located in Champcueil, south of Paris, is presented and analyzed as an example.

1.2.1 Champcueil ground station

The Champcueil ground station is a ground station operated by the French civil aviation authority. The ground station and the pylon are presented in Figure 1.5.

Figure 1.5: Champcueil ground station.

The pylon is 40m high, with a triangular section of 2 meters. It is equipped with 3 UHF antennas, a dish antenna for microwave transmission, and 2 types of VHF antennas: ground-plane antennas and circular arrays of dipoles with reflectors. The positions of the antennas are presented in Figure 1.6.

The ground-plane antennas used at the Champcueil station are presented in Figure 1.7. They are of type GPLB II A, produced by the Radio Frequency System company. They are vertically polarized and omni-directional in azimuth (see Appendix B).

The circular arrays of dipoles with reflectors are presented in Figure 1.8. They are pro-

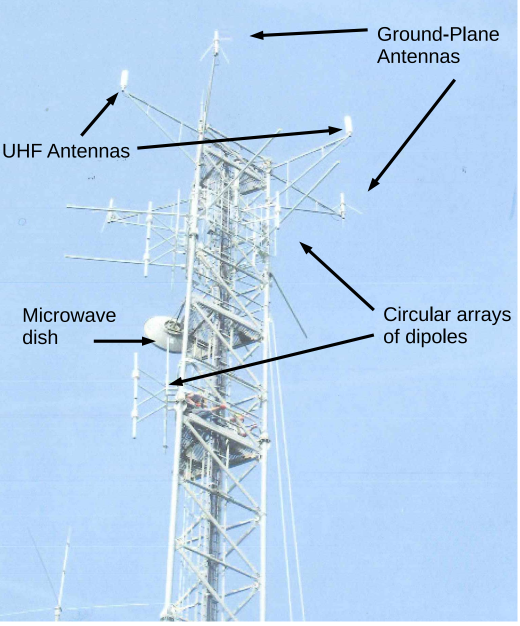

Figure 1.6: Pylon of the Champcueil station.

duced by the Kathrein Company (see AppendixC). An entire circular array is composed of 3 panels, each panel consists of 2 dipoles and a metallic reflector. The total 6 dipoles are fed by a power splitter.

1.2.2 Interference phenomenon measurement

An interference phenomenon has been observed several times at the Champcueil station when there are clouds passing above the ground station. There may be rain or not.

In this Ph.D. thesis, we consider the noise-per-voice-channel, *i.e.* the noise power on a bandwidth B_{c}, which corresponds to the bandwidth of a vocal communication. In Figure 1.9, the power measured is the average value of the noise-per-voice-channel in the VHF aeronautical band B_{a}.

The ambient noise level is about -122dBm. The maximal noise received at the port of the ground-plane antenna reaches -97dBm, which is about 25dB stronger than the

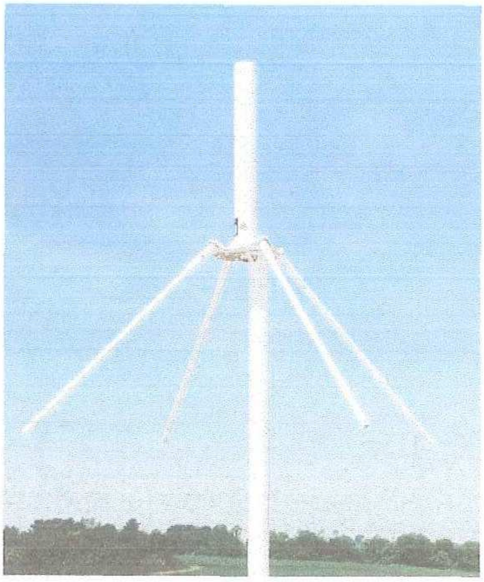

Figure 1.7: Ground-plane antenna used at the Champcueil station.

ambient noise. At the same moment, the noises received at the ports of the upper and lower circular arrays are -112dBm and -120dBm, respectively. These noises last for more than 30 minutes ($5:27 \sim 6:05$).

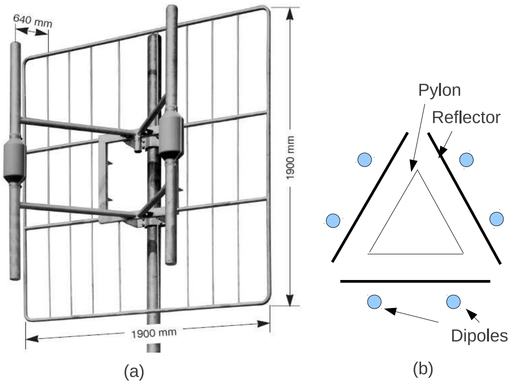

Figure 1.8: Circular array of dipoles with reflectors used at the Champcueil station: (a) a panel; (b) circular array.

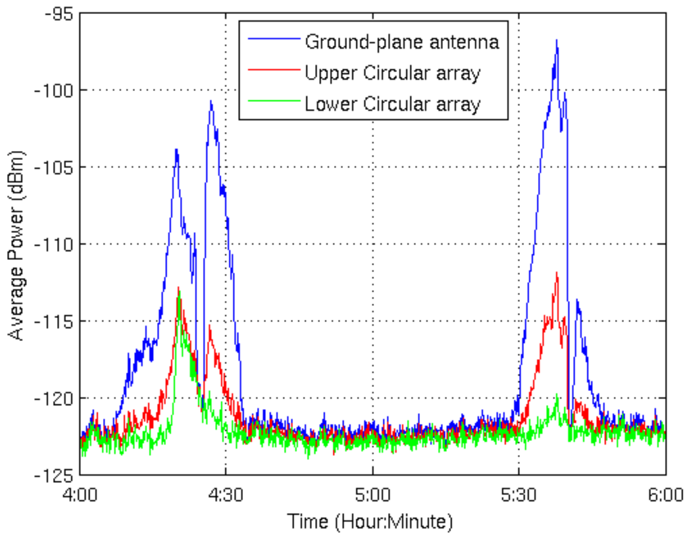

Figure 1.9: Average noise-per-voice-channel received at the different antennas on August 2, 2007.

1.3 Possible reasons for the interferences

The possible reasons for the interferences can be listed in either man-made or natural type. The man-made type includes other ground stations, devices radiating VHF signals and the defects of the device. The natural type includes lightnings and low-power electrostatic discharges. To find the origin of the interferences, these different sources will be presented and analyzed separately.

1.3.1 Ducting phenomenon

Because of the limit bandwidth B_a, identical voice channels of bandwidth 8.33kHz are used at different stations which are far enough from each other (see Figure 1.10(a)). For example, there are 2 ground stations Station 1 and Station 2 that communicate on the same channel. They are located far from each other and their operational coverages are limited by the radio horizon. Normally, an aircraft which communicates with Station 1 would not receive the signal at the same frequency from Station 2.

However, under certain weather conditions, the lower atmosphere may duct the signal by refraction (see Figure 1.10 (b)), the signals propagate beyond the original radio horizon and the new radio horizon is largely extended (see Figure 1.10 (c)) [29]. Hence during communications with the local station (Station 1), an aircraft can receive a transmission from another station (Station 2) at the same frequency, which is supposed to be blocked by the original radio horizon. In a similar way, in case of ducting, a ground station may also receive unexpected transmissions from an aircraft far away from it.

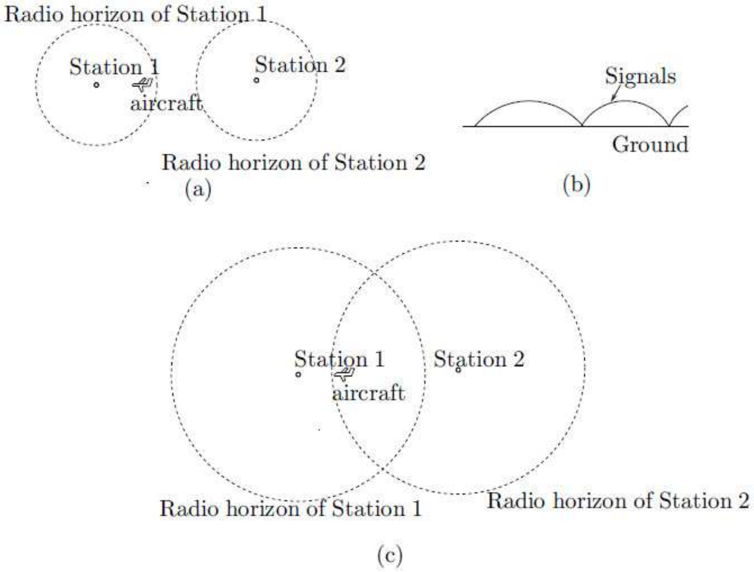

Figure 1.10: Ducting phenomenon: (a) operational coverage of ground stations in normal condition; (b) guiding layer and ducting; (c) operational coverage in ducting conditions.

When the ducting phenomenon occurs, it can be easily identified because the ducting signal is also demodulated. The pilots or the controllers who meet this phenomenon may easily recognize that they are listening unwanted voices from others. The audio records of the noise received at Champcueil station show that the noise is not another voice communication, thus the ducting phenomenon is not the origin of the interferences.

1.3.2 Devices radiating VHF signals

Many equipments and devices radiate VHF signals while functioning, such as computers, engines, etc. There are international standards on electromagnetic compatibility (EMC) for different products to limit the electromagnetic disturbances and to suggest a level of immunity to the disturbances. According to the CISPR (Special International Committee on Radio Interference) Product Standards published by the International Electrotechnical Commission (IEC) [30], the field strength of waves radiated by industrial and scientific equipments should not exceed $30\text{dB}\mu\text{V} \cdot \text{m}^{-1}$ in the frequency band between 30MHz and 230MHz, measured in a position which is 10m from the equipment [30].

On August 2 2007, the maximal noise level received is about -97dBm on the ground-plane antenna (see Figure1.9). With a simple calculation of link budget, we can find that if this noise were generated by a device radiating VHF signals, one possible source is a device, which respects the CISPR standards, at a distance shorter than 20.4m from the antenna. Reminding that the ground-plane antenna is installed on top of a 40m high pylon, this type of radiating devices is not possible to be the interference source. Another possible source is a device located farther than the previous one, which amplitude exceeds the CISPR Standards. For example, a device located 200m away with a radiation level 6.5 times larger than CISPR standards can cause such a noise level.

If a device radiating VHF signals is the origin of the interference phenomenon, the radiating device could be easily identified. At the Champcueil station, measurements have been performed using a directive antenna to identify the radiating source within and around the station. The results have shown that no such device exists near the station. Thus the possibility that devices radiating VHF signals are the origin of the interference phenomenon observed at the Champcueil station is weak.

1.3.3 Low-power electrostatic discharges

The electrostatic discharges radiate signals in a large frequency band including the VHF band [13, 33]. The discharges occur when the local electrostatic field is strong enough. Some electrostatic discharges from different origins have been studied as interference sources for different applications [9, 10, 17, 34, 35]. These possible sources are listed and analyzed in the following parts.

1.3.3.a Precipitation static

The precipitation-static noise is a general class of interference that mainly disables the radiocommunication system of aircrafts when they are impacted by precipitation particles [18]. There are four mechanisms that generate the noise.

The first one is that the high-speed aircraft is charged by triboelectric charging when precipitation particles strike the aircraft and its potential increases to a high value. A noise is generated by corona discharges which occur at the onboard antennas and at other extremities of the aircraft [7, 18]. Corona discharge is a kind of electrostatic discharge that will be presented in the following chapter.

A second type of precipitation static noise is generated by streamer discharges which occur across insulator surfaces to relieve the charge accumulated by triboelectric charging [9, 36]. A high-resistance conductive coating over the insulator surface can drain away the charges, and prevents the rising of voltage and the discharge.

The precipitation static noise include a third type. When the aircraft is charged by triboelectric charging, the unbonded metal sections of aircraft may have different potentials. The potential difference will rise until electrostatic discharges occur over the gap between the sections [9, 36].

These three types of precipitation static noise occurs because the flying aircrafts are at high speed, and they are insulated from other objects. They are charged by the triboelectric effect and their potentials rise to a high enough level to discharge. This is not the case for the pylon that is fixed on the ground. Hence these types of precipitation static noise does not occur at ground stations.

The last type of precipitation static noise is generated in antennas by the passage of the precipitation particles. The precipitation particles, including water drops and ice crystals, may be charged. When these particles are near enough or impact the antenna, electric discharges occur and noises are generated. Some authors [20, 34] have said that this phenomenon generates only important interferences in the VLF and ELF bands. Besides that, the record of the noise shows that the noise does not always appear simultaneously with precipitation. Thus this noise should not be the origin of the interference observed in the VHF band.

1.3.3.b Electrostatic discharge on high-power transmission lines

Electrostatic noise caused by electric discharges on high-power transmission lines have caused interferences in the radio and television broadcast frequency bands [10, 25, 26]. The transmission lines have a small radius and a high potential, that may be up to few hundreds of kilovolts. Thus the electrostatic field around the transmission lines is high enough to generate electric discharges. Two types of sources are mainly responsible for this interference. The main one is corona discharges distributed along the high-power transmission line and tower hardware. The second one is spark and microspark discharges between gaps on transmission line hardware [13]. Corona noise has been detected at frequencies up to 900MHz, while gap noise has been detected at frequencies up to 8GHz [17]. This phenomenon also causes losses on the transmitted power [11, 37].

There are high-power transmission lines about 1km from Champcueil station. Measurements have been performed at the station to verify if the high-power transmission lines are the origin of the interference. They have used a directive antenna to detect the direction of arrival of the interference signal while the noise was occurring. The results have shown that high-power transmission lines are not the origin of the interference because the interference signal does not come from the direction of the high-power transmission lines.

1.3.3.c Electrostatic discharges caused by the natural electrostatic field

If a charged cloud approaches the pylon, the electrostatic field around the pylon and antennas will rise. When the field is stronger than a critical field, electrostatic discharges, particularly corona discharges will occur [6]. This is the same principle as for the St. Elmo's fire appearing on top of the masts of sailing ships during thunderstorms.

Measurements have been performed [3]. They have shown that electrostatic discharges can cause the interference in the VHF band. Thus they constitute a possible source of the observed interference.

Because corona discharges are caused by a natural electrostatic field, the noise should always be detected simultaneously with a strong local electrostatic field.

1.3.4 Lightning

Lightnings radiate electromagnetic waves in a large frequency band from few kHz to several GHz [38]. Because of the high power of lightnings, the antennas of the ground station may receive a VHF signal radiated by lightnings with a strong amplitude, even if the lightnings are far from the station.

When the interference phenomenon occurs, there are not always simultaneously lightnings near the ground station. Thus lightings near the station are not the origin of the interference phenomenon.

1.3.5 Defects of devices

Defects of the devices, particularly the receiver, can cause the interference phenomenon. They could be easily detected by checking separately the performance of each device and they have not been found at the Champcueil station. Therefore they are not the origin of the interference phenomenon observed.

1.3.6 Conclusion

The possible sources of the interference phenomenon have been listed and analyzed. The results show that the most probable source of the interference is corona discharges caused by the natural electrostatic field. The possibilities for other sources of interferences exist, but they are relatively weak. To confirm this hypothesis, an analysis based on measurements are presented in the following section.

1.4 Measurements to determine the origin

1.4.1 Method of the measurements

From the studies of the previous section, the most probable origin of the interference phenomenon is corona discharges caused by the natural electrostatic field. To further identify and attest the origin, measurements have been performed.
Corona discharges always occur simultaneously with a strong local electrostatic field. Hence if an experiment is performed to measure the electrostatic field around the VHF antennas, and if the results show that there is a correlation between the electrostatic field and the noise, the conclusion that corona discharges are the origin of the interference will be strengthened.

A measurement of the electrostatic field near the VHF antennas has been performed at the Champcueil station. A field mill presented in Section 1.4.2 is used to measure the ambient electrostatic field. The field mill is placed on the station building roof (see Figure 1.11). As mentioned previously, the strength of the electrostatic field and the power received at the antenna ports are recorded simultaneously.

Figure 1.11: Position of the field mill: (a) general view; (b) ground station building; (c) field mill above the chimney.

1.4.2 Field mill

The figure 1.12 presents the structure of a field mill. As the shutter rotates, the electrodes constitutes a capacitor that is alternately exposed and shielded. When the shutter is opening, the area of electrodes exposed to the field increases, the capacitor charges and a charging current is generated. On the other hand, a discharge current can be detected when the shutter is closing, *i.e.* when the exposed area of electrodes decreases. Hence an alternate current is generated with the rotation of the shutter, and the current amplitude is in proportion with the measured electrostatic field. By measuring the alternate current, the electrostatic field is determined.

A measurement in laboratory has been carried out by B. Souny of ENAC to verify that

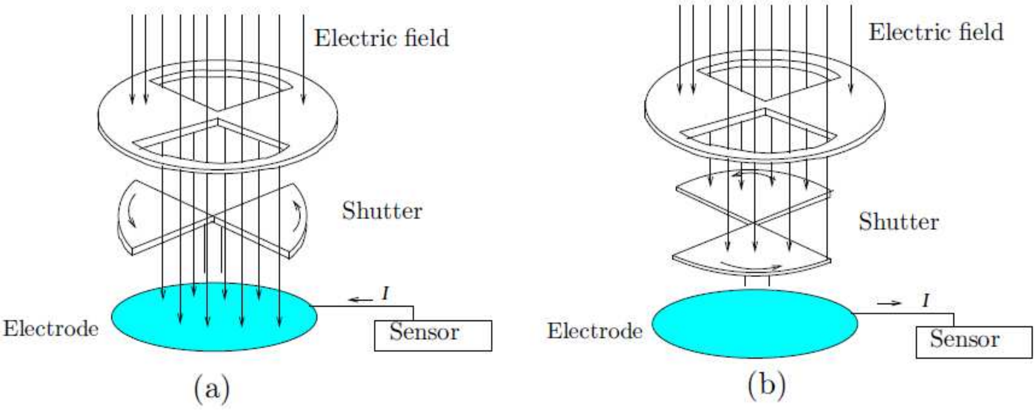

Figure 1.12: Field mill with the shutter: (a) opened; (b) closed.

the field mill does not introduce noise in the VHF band [4]. A VHF halfwave dipole antenna has been used to measure the noise. The measurements have been realized in the 4 configurations shown in Table 1.2. In the measurements, the ambient noise is −118dBm on a voice channel.

Polarization of dipole	Distance from the field mill	Noise-per-voice-channel
Horizontal	10cm	−109dBm
Horizontal	2m	−116dBm
Vertical	10cm	−108dBm
Vertical	2m	−116dBm

Table 1.2: Configurations of measurements performed by B. Souny

The results show that when the field mill is next to the antenna, the noise received is about 10dB stronger than the ambient noise. The polarization of the antenna does not influence the result. When the distance between the field mill and the antenna is larger than 2m, the noise of the field mill is about 2dB stronger than the ambient noise, regardless of the polarization of the antenna.

As a result, considering the position of the field mill in the measurements at the Champcueil station, which is over 30m from the antennas, the field mill should not introduce a noise to the VHF antennas.

Because the field mill is designed to measure the electrostatic field, the high frequency components are filtered out. Hence the VHF field does not influence the result of the field mill.

1.5 Result of the measurement

The measurement lasted several days. An example of the field measured by the field mill on August 2 2007, corresponding to the noise level result shown in Figure 1.9, is presented in Figure 1.13.

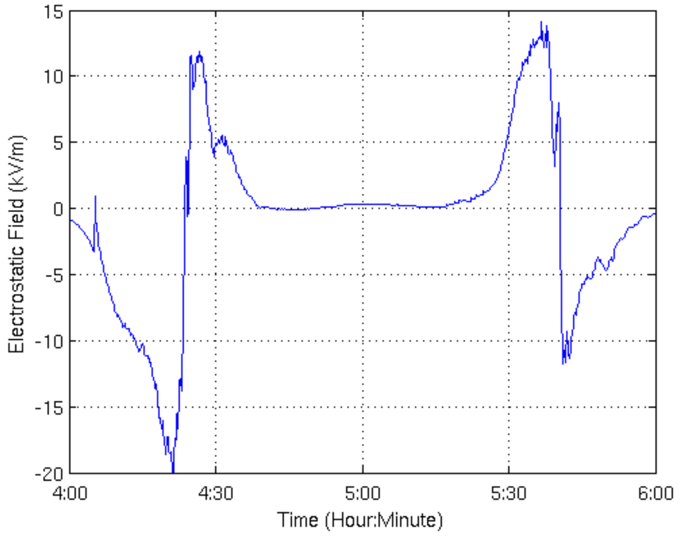

Figure 1.13: Electrostatic field measured by the field mill on August 2 2007.

We observe a strong correlation between this result and the VHF noise presented in Figure 1.9: the noise and the strong electrostatic field appear (at 4:05 and 5:30) and disappear (at 4:35 and 5:50) simultaneously. Their duration are the same. At about 4:25 the electrostatic field changes from negative to positive while the noise level drops to zero. To study the relation between the electrostatic field and the noise level, the correlation coefficient is calculated. For a series of n measurements x_i and y_i, the correlation coefficient r_{xy} is [39]

$$r_{xy} = \frac{\sum_{i=1}^{n}(x_i - \bar{x})(y_i - \bar{y})}{\sqrt{\sum_{i=1}^{n}(x_i - \bar{x})^2 \sum_{i=1}^{n}(y_i - \bar{y})^2}}, \tag{1.8}$$

with $\bar{x}$ and $\bar{y}$ the means of x_i and y_i. The correlation coefficients between the absolute value of the field and the noise received by the antennas are 0.7747, 0.7723 and 0.6037 for the ground-plane antenna, the upper and the lower circular arrays, respectively. Thus there is a strong correlation between the electrostatic field and the noise. This correlation phenomenon has been observed several times during the tests as shown in Appendix A.

The simultaneous appearance of a strong electrostatic field and a noise signal can explain the interference phenomena observed in the VHF band at the Champcueil station. A strong electrostatic field generates electric discharges, particularly corona discharges, around the sharp points, such as the lightning conductor and the antennas. These electric discharges can introduce a noise in the VHF band. Thus the hypothesis that corona discharges are the origin of the interference phenomenon has been attested by measurements.

1.6 Conclusion

The civil aviation VHF radiocommunication system impaired by the interference phenomenon has been presented. We have also shown the interference noise at the Champcueil station. We have listed and analyzed the possible origins for this interference. The noise level and the value of the electrostatic field have been measured simultaneously. The results have shown that there is a strong correlation between a strong electrostatic field and a strong interference. Thus we have confirmed that electric discharges, and particularly corona discharges caused by a strong electrostatic field, are probably the origin of the interference phenomena observed in the VHF band at the Champcueil station.

Chapter 2

Mechanism and characteristics of corona discharges

In the previous chapter, electrostatic discharges, particularly corona discharges have been found as a possible origin of the interference phenomenon observed in Champcueil station. In order to further study the noise, the mechanisms and the characteristics of corona discharges must be understood. In this chapter, the mechanisms of corona discharges are presented. Then their characteristics, including the current shape, the spectrum, the amplitude, are presented for further applications.

2.1 Mechanism of charged particles production

Electrostatic discharges may occur between electrodes at different potentials. Normally, the medium between the electrodes (air in our case) is insulated. Under certain conditions, such as a strong electric field or high temperature, the number of charged particles in the medium can strongly increase. Thus the medium becomes conductive and a discharge current is produced. Therefore the increase of the number of charged particles is the basic of electrostatic discharge. Different mechanisms of charged particles generation will be presented in this section.

2.1.1 Photonionization

A photon has an energy hf, where $h = 6.63 \times 10^{-34}\mathrm{J} \cdot \mathrm{s}$ is the Planck constant and f is the frequency. This energy can liberate electrons from atoms when photons impact atoms. This mechanism is called photoionization.

In the atmosphere, Some gas molecules are ionized by cosmic rays and other natural radiations. Free electrons and positive ions are produced. Because of the thermal motion, recombination may occur during the impact between a free electron and a positive ion. An electron is captured by a positive ion and a new neutral particle is produced. In steady-state, there is an equilibrium between the ionization and the recombination so that the charge density in air remains constant [6].

Because of the photonionization phenomenon, a current is always observed even if the potential difference between the electrodes is very weak. The figure 2.1 presents the voltage-current relation corresponding to the photonionization and the avalanche phenomenon. The latter will be presented in the next section [40].

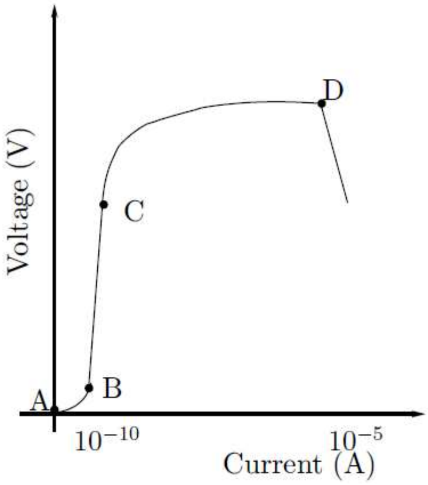

Figure 2.1: Voltage-current characteristics [40].

The Figure 2.1 shows that the curve can be divided into different stages:

- A-B : The electrons and positive ions produced by the cosmic radiation drift to the anode and cathode respectively by the effect of the external electric field (due to the difference of potential). Hence a weak current is generated. If the voltage applied to the electrodes increases, more carriers (electrons and positive ions) will arrive at the electrodes before recombination, so the current will increase. This stage is called the background ionization.
- B-C : At point B, almost all carriers generated by cosmic rays can arrive at the electrodes, so the current remains almost the same while the applied potential is increased. The current is saturated and its amplitude depends on the level of radiation. This stage is called the saturation region.
- C-D : When the potential difference between the electrodes increases beyond point C, the avalanche phenomenon occurs. In this stage, the current rises exponentially with the potential applied. This is called the Townsend discharge [6]. When the discharge current is strong enough, corona discharges occur.

In these stages, the discharges are generally dark. If the voltage applied increases beyond the point D, the discharge will emit light, and a further increase in voltage will lead to arc.

2.1.2 Avalanche

As presented in the previous part, even without potential difference, some atoms are ionized by photons and free electrons are generated. When a potential difference is applied between the electrodes, the charge carriers which appear initially in the system (ionized by radiations) drift to the electrodes (electrons to anode and positive ions to cathode). In this process the electrons collide with the neutral particles. If an electron has acquired enough kinetic energy before the collision, it can ionize a neutral atom. In this impact ionization, additional electrons are released and the neutral atom becomes a positive ion. The new-produced electrons and the initial ones are accelerated by the electric field and collide with other neutral atoms. This process repeats and more free electrons and positive ions are produced. This process is called the electron avalanche.

The avalanche is the main mechanism to generate charged particles [6, 40].

Because the mobilities of electrons and ions are very different, the ions are practically fixed during the drift time of electrons. Hence the electrons and ions are separated. This separation generates an internal electric field which is in the opposite direction of the external field. Because of the electron diffusion, the radial size of the avalanche increases during the electron drift toward the anode. When the electron multiplication in the avalanche reaches a critical value, space charge effects due to the separation of electrons and ions modify the electric field in the avalanche and the avalanche transforms into a streamer (see below). The Figure 2.2 presents the avalanche, and the electric fields $\mathbf{E}_{\text{ext}}$ and $\mathbf{E}_{\text{int}}$, where $\mathbf{E}_{\text{ext}}$ is the external field generated by the potential difference, $\mathbf{E}_{\text{int}}$ is the internal field generated by the separated space charges.

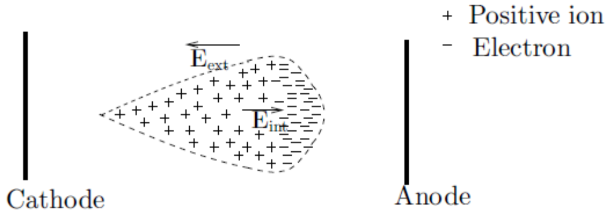

Figure 2.2: Avalanche[6].

2.1.3 Electron emission from the surfaces of electrodes

Besides the electron avalanche, there are different types of electron emissions from the surfaces of electrodes that can also increase the charge density in the medium [40] :

- Thermal electron emission : When a metallic electrode is heated to a certain temperature, some electrons can get enough energy to leave the surface of the electrodes. By the effect of the electric field, these electrons drift to the anode.
- Emission by the effect of field : When a strong enough electric field is applied, approximately 10^8V/m, electrons can be pulled out of the cathode surface.

- Secondary electron emission : Free electrons may be extracted from electrodes while the electrodes are impacted by particles, such as positive ions, excited atoms, electrons and photons. The most important one for our case is the emission produced by the collision between positive ions and the cathode.

2.2 Streamer

In the previous section, the mechanisms of electron production have been presented. In normal conditions, the medium (air) is a dielectric. When the number of carriers (electrons and ions) is increased by avalanche or other mechanisms, the medium becomes conductive. Hence the discharge phenomena occurs.
There are different types of electrostatic discharges. The kind of discharge that occurs depends on many parameters, such as the potential difference, the distance between the electrodes, the pressure, the type of gas between the electrodes, etc. The product of the gas pressure p and the distance between electrodes d is an important parameter [6, 40]. From [6], when pd is high, the discharge phenomenon is different from the one for small pd value. When $pd < 300\text{Torr} \cdot \text{cm}$ ($1\text{Torr} \simeq 1.3 \times 10^{-3}\text{atm}$), the discharge process is steady. When $pd > 10^3\text{Torr} \cdot \text{cm}$ ($1\text{Torr} \simeq 1.3 \times 10^{-3}\text{atm}$), the discharge becomes a quick transient process [6]. In our case, the environment is outdoor. Thus the pressure is of the order of 1 atm (about 10^3Torr), and the distance between electrodes (pylon and cloud) is at least 100m. This corresponds to a high pd. To explain the discharge process in this case, the theory of streamer is presented in this section.

A streamer is a weakly ionized channel formed from the primary avalanche. As presented in Figure 2.2, the electrons generated in avalanches drift to the anode, leaving a trail of slowly-drifting positive ions. These positive ions generate an internal field opposite to the external one. When this internal field is strong enough, of order the external field [6, 41], the electrons near the positive trail are attracted into it, and the positive ion cloud becomes a mixture of positive ions and electrons. The avalanche transforms into a streamer.

A streamer is a conductive channel where the densities of electrons and ions are large and practically equal (quasi-neutral plasma) and the electric field is small (because of its large conductivity). At the tips of the channel the electric field is strongly enhanced due to the presence of strong negative or positive space charge (on the anode and cathode sides, respectively).

The streamer grows in one or two directions towards the electrodes. Because of its relatively high conductivity, it can modify the field and greatly increases the current upon reaching the electrodes. When it reaches the electrodes, it may lead to a spark discharge in the gap.

Some streamers are ignited at the anode surface and propagate to the cathode. These streamers are called cathode-directed or positive. There is also an anode-directed or negative type of streamer [6, 41]. Although the propagation of anode-directed streamers is well understood and is due to the electron drift and multiplication in the high-electric field at the streamer tip on the anode side, the propagation of cathode-directed streamer is more complex and is not due to the propagation of ions toward the cathode (cathode-directed streamers and anode-directed streamers have similar propagation velocities, much larger than the ion drift velocities).

2.2.1 Positive streamer

The positive streamer grows from the anode to the cathode. Figure 2.3 shows the growth of the positive streamer. The atoms excited in the avalanche emit photons. These photons can ionize atoms in the vicinity of the primary avalanche and produce some free electrons (Figure 2.3(a)). These new-generated electrons ignite new avalanches which are called secondary avalanches. The electrons produced in the secondary avalanches are attracted by the positive ions generated by the primary avalanche (Figure 2.3 (b)), and form a quasi-neutral plasma. Ions generated during this process contribute to the propagation of the positive streamer tip toward the cathode and the elongation of the streamer in the cathode direction (Figure 2.3 (c)). This process repeats, and the streamer grows [42].

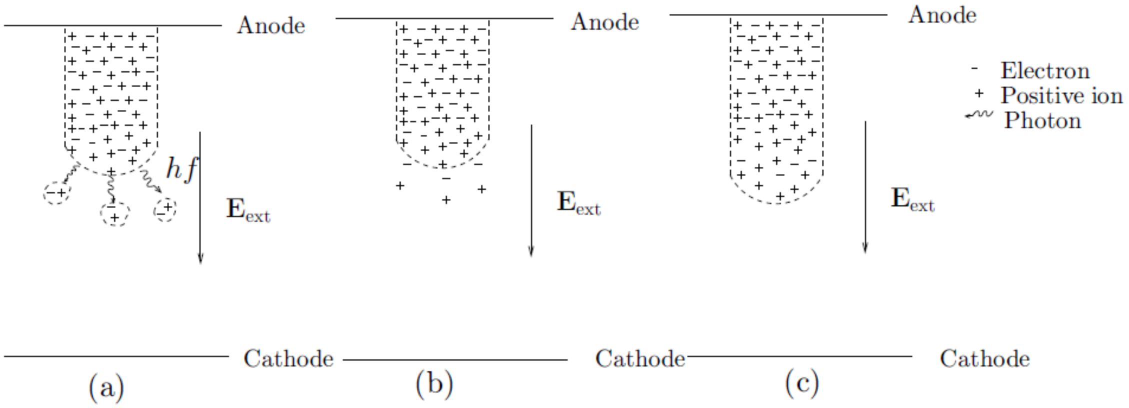

Figure 2.3: Growth of positive streamer: (a) atoms ionized by photons and secondary avalanche; (b) drift of electrons to the steamer; (c) growth of streamer [6].

2.2.2 Negative streamer

The avalanche may sometimes transform into a streamer in a position between the electrodes. This happens when the internal space-charge field reaches the same level as the external field before the avalanche reaches the anode. This kind of streamer grows towards both directions. The mechanism of growth towards cathode is the same as for the positive streamer. For the anode direction, the mechanism is different.

On the anode side, the neutral atoms in vicinity of the primary avalanche are ionized by the multiplication and drift of the electrons at the streamer tip. Photoionization can also contribute to the anode streamer propagation but does not play an essential role (Figure 2.4 (a)). The external field $\mathbf{E}_{\text{ext}}$ attracts the electrons of secondary avalanche away from the primary avalanche, which is the main difference with the positive streamer [6, 43]. By the effect of the external field, the electrons concentrated in the head of the primary avalanche move rapidly to join trails of new-generated ions (Figure 2.4 (b)). The plasma is then formed and the streamer grows (see Figure 2.4 (c)).

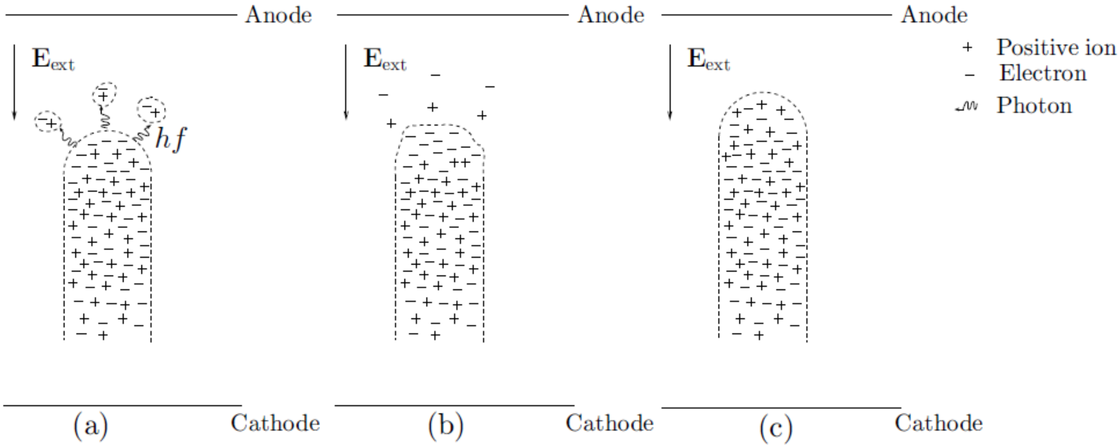

Figure 2.4: Growth of negative streamer: (a) atoms ionized by secondary avalanches and photons; (b) drift of the electrons in the head of streamer toward the new-produced ions; (c) streamer growth [6].

2.3 Corona discharge

When the electric field is strongly non-uniform, corona discharges occur. The electric field near at least one electrode is strong enough to ignite discharges. The field in the rest of the gap is normally much weaker. The electrode with the strong electric field is called the active electrode. This kind of electric field usually occurs when the active electrode has a small radius compared with the other electrode, for example, a point electrode and a plane one, or a line electrode and a cylinder one. (see Figure 2.5).

From Figure 2.5, it is clear that the electric field around the active electrode (electrode 1 in Figure 2.5) is much stronger than the field in the rest of the gap between the electrodes. Because a strong electric field is necessary for avalanches and streamers, corona

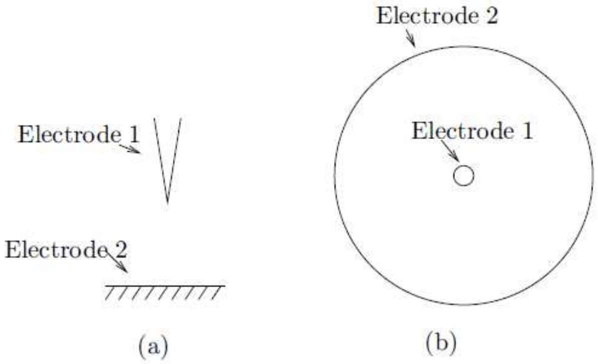

Figure 2.5: Different configurations of corona discharger : (a) point-plane, (b) line-cylinder.

discharges occur near the active electrode. As a result, the ignition of corona discharges depends on the maximal level of the electrostatic field near the active electrode.

The active electrode may be polarized positively or negatively, which means that the active electrode works as the anode or cathode in the system, respectively. This introduces a difference in the generation mechanism of corona discharges. Hence the corona discharges can be divided into 2 groups: positive corona and negative corona [44]. They will be presented in the following section.

2.3.1 Mechanisms of corona discharges

2.3.1.a Positive corona discharge

The positive corona discharges ignite in the region where the electrostatic field is strong, *i.e.* near the active electrode (anode). The avalanches are ignited by the strong electric field near the anode and then transforms into positive streamers if the electric field or applied voltage is large enough (positive corona streamers). Photons are emitted from the heads of the streamers, which are the regions of plasma. These photons ionize the atoms in the vicinity of the plasma surfaces, so that secondary avalanches occur and the positive streamers grow. The growths of positive streamers stop at a certain distance from the cathode because when the positive streamers grow to places far away from the anode, the electric field is too weak to maintain the avalanches, and the streamers stop growing. Hence the avalanches and the plasma concentrate just in the vicinity of the anode [6, 41, 44, 45].

The electrons of the plasma are attracted to the anode and a current is generated. At the same time the positive ions accumulate around the anode. These positive ions form a positive layer and produces an electric field opposite to the external field inside the layer. Hence the total field decreases and the avalanches stop, then the current decreases. The formation of positive corona streamers is therefore associated with a current pulse. After that the ions of the positive layer are pulled away by the electric force and the positive layer disappears. The total electric field restores to ignite new avalanches, so that a new cycle begins. The corona current is thus a series of pulses [6, 41, 45].

2.3.1.b Negative corona discharge

The negative corona discharges ignite around the cathode, where the electric field is strong. Avalanches begin under the effect of the electric field. Positive ions, which present in the vicinity of the cathode, enhance the local field, and electrons are pushed away to the anode.

The avalanches then transform into negative streamers, and the negative streamers grow (just towards the anode), as the process presented in Section 2.2.2. The growth of negative streamers stops somewhere between the electrodes, as for positive corona. The avalanches and the plasma concentrate also around the active electrode, the cathode.

The current shape of negative corona discharge is a pulse. The positive ions are attracted to the cathode while the electrons are pushed away rapidly. Hence the electron density around the cathode is low, and there is no negative layer formed to reduce the external electric field, unlike for the positive corona discharge. When the electrons are pushed to a place far from the cathode, the electric field decreases and the electrons attach with the neutral molecules to form negative ions. These negative ions produce an electric field that weakens the total field. The multiplication of avalanches and the corona current decreases. After that, the negative ions are pushed further to the anode, the external field is restored and a new cycle begins [6, 41, 44, 45].

2.3.2 Characteristics of corona discharges

The definition and the mechanism of corona discharges have been presented in the previous sections. To study the radiation features of corona discharges, it is necessary to provide its characteristics, such as the critical field of ignition, the current shape, the spectrum and the repetition rate of pulses. These characteristics are described in this section.

2.3.2.a The critical field of ignition

The critical field of ignition, or the corona inception field, is the electric field at the surface of the active electrode from which the corona discharges occur. If the electric field around the active electrode is stronger than the critical field, corona discharges develop. This parameter is important in our case because we will compare the electric field with the critical field to identify the places where corona discharges most likely occur.

Peek has proposed an empirical formula for the critical field $||\mathbf{E_c}||$ in air between coaxial cylinders. To simplify the presentation, we note $E = ||\mathbf{E}||$. The Peek formula is given by [46]

$$E_\mathrm{c} = E_0\delta\left(1 + \frac{0.308}{\sqrt{\delta r}}\right), \tag{2.1}$$

where $E_0 = 31\mathrm{kV/cm}$, r is the radius of the conductor in cm, δ is the ratio of air density to the normal density corresponding to $p = 760$ Torr and $T = 25°\mathrm{C}$.

The Peek formula has been proposed for the coaxial cylinder configuration [46]. In the literature, this formula is also used for other configurations, such as wire-plane, wire-wire, and point-plane configurations. In our case, the Peek formula will also be used. The details will be presented in Section 3.5.

2.3.2.b Corona discharge current

The corona discharge current is a series of pulses. Many measurements to study the corona current pulses have been done [14, 16, 47, 48, 49]. Some empirical expressions have been suggested to represent the positive and negative corona pulse shapes [13, 16, 17, 49].

For positive corona discharge, a series of measurements has been performed in [49] with a line-cylinder configuration. The outer cylinder is 122cm long with a 40cm diameter. The potential difference between the electrodes varies between 41 and 58kV. Besides, different line electrodes which diameter varies between 1.31 and 5.94mm are used. The measurement results show that for different voltages or different wire sizes, the shape of the pulse does not vary. The pulse current $i_\mathrm{p}(t)$ can be expressed by means of a double-exponential as

$$i_\mathrm{p}(t) = K i_\mathrm{max}(e^{-\alpha t} - e^{-\beta t}), \tag{2.2}$$

where i_max is the maximal current of the corona pulse, α and β are constants, and K is a coefficient depending on α and β. The measurement results in [49] suggest $\alpha = 0.0105\mathrm{ns}^{-1}$, $\beta = 0.03465\mathrm{ns}^{-1}$ and $K = 2.41$. Hence the positive corona current is a series of pulses with a rise time (time for the current to grow from 10% to its 90% of maximal amplitude) about 30ns and a fall time (time for the current to drop from 90% to 10%) of about 250ns. Figure 2.6 shows the normalized pulses of corona current.

For negative corona discharge, measurements have also been performed in [49]. The configuration of measurements is the same as for positive corona, except that the polarity of the electrodes is reversed. The measurement results have shown that the negative pulse is also a double-exponential with different parameters. In [49], the measurements yield

$\alpha = 0.0383\text{ns}^{-1}$, $\beta = 0.083\text{ns}^{-1}$, and $K = 3.6$. The pulse of negative corona is shorter and steeper than the pulse of positive corona. Its rise time is about 10ns and its fall time is about 70ns.

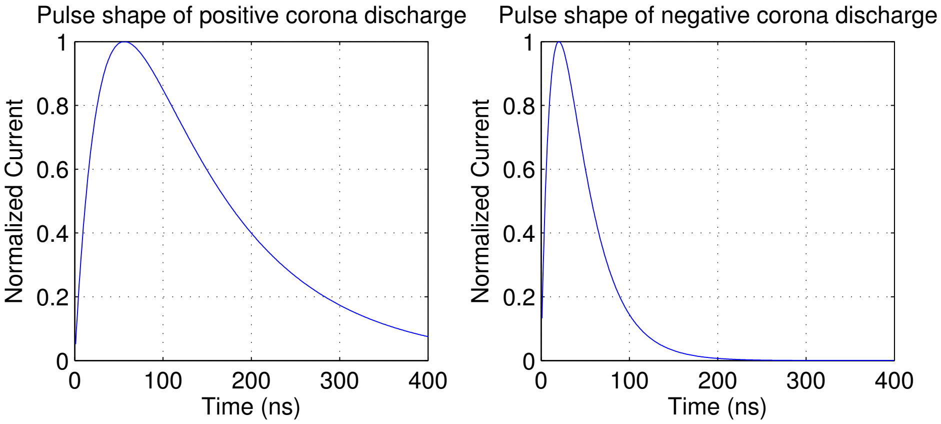

Figure 2.6: Pulses of positive and negative corona discharges.

2.3.2.c Spectrum

The spectrum of one corona pulse can be obtained by the Fourier transformation of the expression of the corona current. As presented in the previous section, positive and negative corona pulses can be expressed as (2.2) with different parameters, hence the spectrum of a single corona discharge pulse can be calculated. The figure 2.7 presents the normalized spectrum of a single corona discharge pulse.

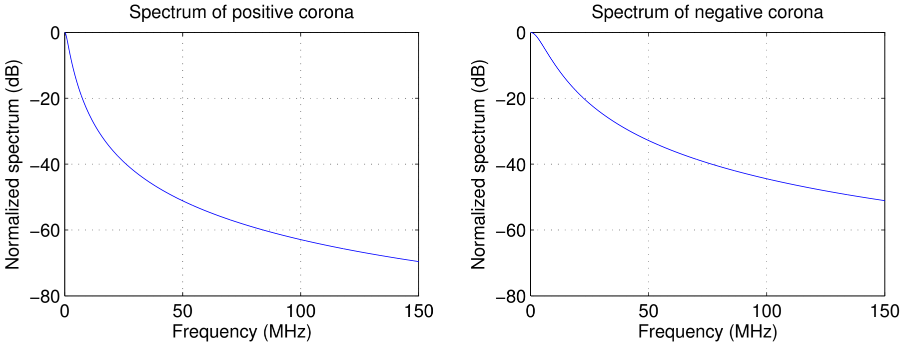

Figure 2.7: Normalized spectrum of a single positive and negative corona pulse(Fourier transformation).

Figure 2.7 shows that the spectrum of a single corona discharge pulse is relatively strong in the low frequency band (< 10MHz). Its amplitude decreases rapidly when the frequency increases. For positive corona discharges, the spectrum in the VHF aeronautical band B_{a} is about 65dB weaker than the low-frequency component ($f = 1$Hz); for negative corona discharges, it is about 50dB weaker. This agrees with the measurement results in [13] and [48].

The spectrum of a single corona pulse will be used in Chapter 4, to determine the radiation level of corona discharges in the VHF band.

2.3.2.d Pulse repetition rate

Corona discharges are a series of pulses [6, 12], of shape given by (2.2). As will be explained in Chapter 4, the repetition rates of the pulses are important for obtaining the average radiated power of corona discharges in the VHF band.

Measurements have been performed to determine the pulse repetition rate [48, 49, 50]. We list the minimal and maximal repetition rates in Table 2.1. In this table, it should be noticed that all the measurements do not correspond to the same configuration: in [50], the point-plane configuration is used. The distance between the point and the plane electrode is 11cm and the radius of the point is 0.04mm. In [48], the line-cylinder configuration is used, with a wire of diameter 18mm and a cylinder of diameter 0.5m. In [49], the configuration is also line-cylinder but the diameter of the line electrode is 2.62mm and the diameter of the cylinder is 40cm.

Type of corona		Potential difference (kV)	Repetition rate (kHz)
Positive	min	7	0.1 [50]
	max	4	3.7 [50]
Negative	min	20	1 [48]
	max	54	92 [49]

Table 2.1: Repetition rates of corona discharges.

From Table 2.1, we can conclude that the repetition rate is much higher for negative corona discharges than for positive discharges.

2.3.2.e Amplitude of corona pulses

The amplitude of corona pulses increases with the voltage applied to the electrodes [16, 17, 48, 49]. The amplitude of pulses depends on many parameters such as the type and the size of the electrodes [49], the configuration of measurement, the humidity of air [48], etc. When the potential difference between the electrodes is weak so that the electrostatic field is near the critical field of ignition, corona pulses are very weak, of order few micro Ampere or less [6]. Table 2.2 shows the measurement results of some corona pulses, both strong and weak, in the line-cylinder configuration with different parameters.

Line Diameter (cm)	Cylinder radius (cm)	Polarization	Applied voltage (kV)	Pulse amplitude (mA)
2.4	75	Positive	80	21 [13]
1.8	25	Positive	60.0	2.4 [48]
1.8	25	Negative	60.0	0.8 [48]
0.46	20	Positive	54.0	122 [49]
0.46	20	Negative	57.1	54 [49]
0.29	20	Negative	41.0	37 [49]

Table 2.2: Amplitude of corona pulses.

Table 2.2 shows that the amplitude of positive corona pulses can exceed 100mA. For negative corona pulses, the maximal level is about 50mA. With the same geometry of electrodes and the same level of potential difference between the electrodes, we observe that the amplitude of positive corona pulses are twice stronger.

2.3.2.f Size of the corona discharges

Corona discharges occur at the places where there is a strong non-uniform field, so that corona discharges currents concentrate in a narrow region around the active electrode. Outside this region, the charge carriers diffuse and drift to the other electrode and the current density is much lower. The measurement results presented in [51, 52, 53, 54] suggest that the dimension of the zones with a strong corona current density is about few centimeters.

2.3.3 Summary of corona discharges characteristics

In the previous sections, some characteristics of corona discharges have been studied. They will be used to determine the radiation level of corona discharges in the VHF band in Chapter 4. To conclude, positive and negative corona discharges have different characteristics that are listed in Table 2.3.

Characteristics	Positive corona	Negative corona
Rise time (ns)	30	10
Fall time (ns)	200	70
Pulse Current (mA)	[2, 120]	[1, 50]
Repetition rate (kHz)	[0.1, 4]	[1, 100]
Size of corona current region	few cm	few cm

Table 2.3: Summary of corona discharge characteristics.

2.4 Conclusion

In this chapter, the mechanism of positive and negative corona discharges has been presented. The different characteristics of positive and negative corona discharges including the critical field of ignition, the current waveform, the spectrum, the pulse repetition rate, the zone in which corona current concentrates, and the amplitude of the pulses have been described. They will be used in the following chapters.

Chapter 3

Electrostatic simulations

In the previous chapters, the interference phenomenon and its possible origin have been shown. The aim of this Ph.D. thesis is to evaluate the noise level introduced by corona discharges. Hence, we must localize the places where corona discharges most certainly occur. A method on that purpose will be developed in this chapter.

As presented in the previous chapter, corona discharges occur in the places where the electrostatic field is strong enough to pass the ignition field. Thus we perform electrostatic simulations to evaluate the electric field around the pylon. Then, the places where the corona discharges occur can be localized.
The simulations are realized *via* the Finite Element Method. This method is used to numerically solve partial differential equations with appropriate boundary conditions.

In Section 3.1, the basic electrostatic equations are developed. In Section 3.2, the numerical method used to realize the simulations is presented. Some hypotheses are proposed to render the problem consistent with numerical simulations in Section 3.3. These hypotheses are tested and a test case is constructed in Section 3.4. In Section 3.5, we propose a criterion to localize corona discharges. Finally, in Section 3.6, simulation results are analyzed and the places where corona discharges occur are localized.

3.1 Basic equations

As presented in Chapter 2, corona discharges occur at the places where the electrostatic field is strong enough. Due to the geometry of the pylon, the field is strongly non-uniform. Thus, it will only pass the ignition field in a limited number of areas. Thus, the level of the electrostatic field around the pylon can be used to identify the locations where corona discharges occur.

From Maxwell-Gauss equation, we have

$$\nabla \cdot \mathbf{D} = \rho(t), \tag{3.1}$$

where $\rho(t)$ is the charge density in the medium and $\mathbf{D}$ is the electric displacement field. The electric displacement field $\mathbf{D}$ can be written as

$$\mathbf{D} = \varepsilon \mathbf{E}, \tag{3.2}$$

where ε is the permittivity of the medium, and $\mathbf{E}$ is the electric field. In electrostatic, the electric field $\mathbf{E}$ can be written by means of an electric potential V such that

$$\mathbf{E} = -\nabla V. \tag{3.3}$$

Therefore we have

$$\nabla \cdot (\varepsilon \nabla V) = -\rho(t). \tag{3.4}$$

For the boundary conditions, we consider 2 electrodes, the charged cloud and the ground, on which the potential V_0 and V_{ground} are constant (see Figure 3.1).

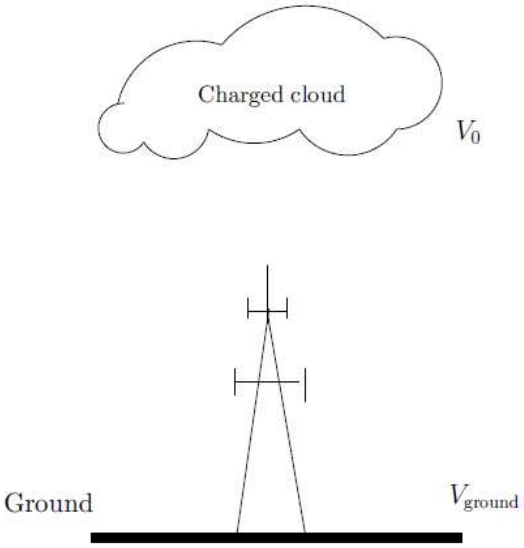

Figure 3.1: Electrostatic configuration.

3.2 Finite element method

To numerically solve the equation (3.4), we use the COMSOL software based on the Finite Element Method (FEM). We here give the main characteristics and constraints of this method.

The FEM is a technique used to numerically solve partial differential equations (PDE) with associated boundary conditions in a bounded domain [55, 56]. The unknown function satisfying the partial differential equations is V in our case. The basic steps for finite element analysis are [55, 56, 57, 58]:

- To mesh the given domain into a set of finite elements. In 3D, these finite elements are usually tetrahedrons.
- To construct the weak form of the PDE. The weak form can be understood as a formulation of the projection of the equation onto test functions.
- To approximate the solution as a weighted sum of basis functions, that is

$$V = \sum_{n=1}^{N} a_n V_n, \tag{3.5}$$

where a_n are unknown coefficients, V_n are the basis functions, and N is the number of basis functions. A basis function is generally assigned to each element. The test functions are also projected into a space of size N.

- To derive the finite element equations by substituting the approximate solution into the weak form. The weak form is then transformed into a sparse linear system of size N and of unknown a_n.
- To solve the linear system to find a_n, from which we obtain an approximate numerical solution of the partial differential equation.

From the FEM steps, a large domain yields an important number of elements, and thus a long computation time.

3.3 Formulation and simplification for the FEM simulation

Equation (3.4) has been presented in the previous section. Our objective is to numerically solve this equation. To achieve this goal, we adapt the formulation by means of simplifications to render the problem amenable by the FEM. They are presented in this section.

3.3.1 Simplification of the equations

To solve (3.4), the charge density $\rho(t)$ is required. To simplify the model, we evaluate the electrostatic field just before the discharges occur. At this moment the electrostatic field is so strong that corona discharges will occur. Because the discharges have not started yet in the atmosphere around the pylon, there are only charges ionized by cosmic ray, which are negligible. Thus the electrostatic field is just caused by the two electrodes: the charged cloud and the pylon. We can therefore make the hypothesis that there are no free charges in the atmosphere around the pylon in the simulation, that is $\rho(t) = 0$.

Hence, (3.4) becomes

$$\nabla \cdot (\varepsilon \nabla V) = 0. \tag{3.6}$$

3.3.2 Ground electrode

The boundary conditions impose a constant potential difference between the charged cloud and the ground. We here represent the charged cloud and the ground by the sky and the ground electrodes, respectively. They have a simple geometry so that the simulation is as simple as possible.

The ground electrode includes the ground and the metallic pylon. We suppose that the ground is flat without any objects except the pylon. Hence the ground can be represented by a plane. The potential at the ground electrode is a constant. Because only the potential difference between the electrodes is required to uniquely define the problem, we can set the potential of one electrode to zero. We here choose the potential of the ground electrode to be zero.

The real pylon is a complex structure. For example, the pylon of the ground station at Champcueil is made of metallic tubes (see Figure 1.6). It is therefore necessary to simplify the model of the pylon to save computation time. Because of the Faraday cage effect, the field inside the pylon is very weak, and it has a small influence on the electric field outside the pylon. Hence, the pylon is simplified to a solid metallic structure (see Figure 3.2), with the antennas installed on its surfaces. Because the pylon is constructed with conductive materials and grounded, its potential is the same as the ground.

3.3.3 Sky electrode

As presented in the previous section, the charged cloud is represented by a sky electrode in the simulation. We suppose that the charged cloud is above the pylon, and it covers a

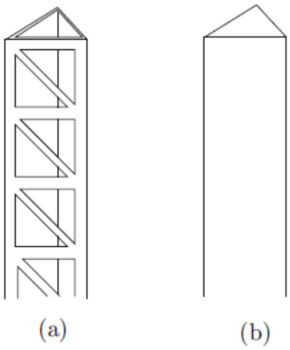

Figure 3.2: Model of the pylon: (a) original pylon; (b) solid metallic structure.

very large area. In our model, the charged clouds are represented by a planar electrode at a certain altitude with a certain potential. This electrode occupies the entire upper surface of the computation domain. This hypothesis will be tested in Section 3.4.3.b.

We here define the ambient field that corresponds to the electrostatic field between the planar sky electrode and the planar ground electrode (see Figure 3.3), *i.e.*, without the influence of the pylon.

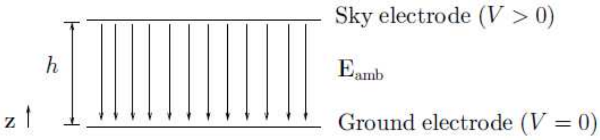

Figure 3.3: Ambient field.

The field between the sky and the ground electrodes is similar to the electric field in a parallel-plate capacitor, that is uniform. Hence, if the potential at the ground electrode is zero, the potential at the cloud electrode can be calculated as

$$V_0 = -(\mathbf{E}_{\text{amb}} \cdot \mathbf{z})h, \tag{3.7}$$

where V_0 is the potential at the cloud electrode, $\mathbf{E}_{\text{amb}}$ is the ambient field, $\mathbf{z}$ is the unit vertical vector from the ground to the sky, and h is the altitude of the sky electrode.

3.3.4 Lateral boundaries

The Finite Element Method, used here to numerically solve the equations, requires a finite computation domain. We choose the computation domain as a rectangular box with the pylon in the center of the lower surface. The upper and lower surfaces are the sky electrode and the ground, respectively. On these surfaces the potential are constant and known. On the vertical planes (lateral boundaries), no boundary conditions are specified by the physics, but they are required by the FEM. We therefore suppose that the lateral boundaries are located far enough from the pylon, so that the perturbation yielded by the pylon is negligible. As shown in the previous section, the electrostatic field **E** at the boundaries is thus similar to the electric field in a parallel-plate capacitor: the electric field lines are vertical. Finally, the boundary condition on the lateral boundaries can be expressed as

$$\mathbf{E} \cdot \mathbf{n} = 0, \tag{3.8}$$

where **n** is the normal vector to the vertical boundaries (see Figure 3.4). With (3.3), (3.8) can be written as

$$\frac{\partial V}{\partial \mathbf{n}} = 0. \tag{3.9}$$

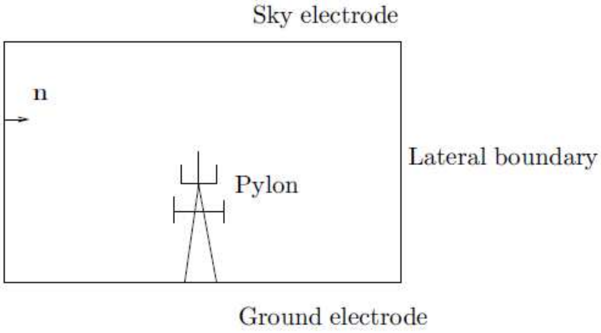

Figure 3.4: Lateral boundaries of the computation domain.

3.3.5 Ground station building

In practical applications, there may be some other objects near the pylon. If such objects exist, their heights must always be significantly smaller than the pylon, so that the VHF antenna radiation is not perturbed, *i.e.* remains omni-directional in azimuth. For example, at the Champcueil ground station, the building of the ground station is next to the pylon (see Figure 1.5). Its height is about 7m, which is small compared to the 40m high pylon. We therefore ignore the presence of such objects in the simulation because of the shielding effect of the pylon. With this simplification, we can assume that $\varepsilon = \varepsilon_0$ in the entire computation domain, where ε_0 is the vacuum permittivity. Finally, (3.4) is simplified as

$$\nabla^2 V = -\frac{\rho(t)}{\varepsilon_0}, \tag{3.10}$$

and (3.6) can be expressed as

$$\nabla^2 V = 0. \tag{3.11}$$

3.3.6 Simplified model for 3D simulations

With the hypotheses mentioned previously, we have defined a model for the electrostatic simulation. The equation to be solved is (3.11) in a rectangular box domain. The boundary conditions associated with the equation imply that the potential on the upper and lower surfaces are constant. On the lateral boundaries, (3.9) is satisfied. The pylon is located in the middle of the lower surface, as part of the ground electrode. The ground station building is ignored.

3.4 Model test

In Section 3.3, the formulation and simplification for the 3D simulation have been presented. In this section, we verify if this model can correctly represent the real case. To do so, we firstly consider the Champcueil ground station as a test case. Then, the different hypotheses are tested one by one.

3.4.1 Test case

We consider the Champcueil ground station as a test case. Its characteristics are as follows:

- The computation volume is a box. The lateral boundaries are located 40m from the pylon.
- The charged cloud is represented by a planar sky electrode at an altitude of 100m. The potential at the sky electrode is set to $V_0 = 2 \cdot 10^6$V.
- The ground station building is ignored.
- The pylon is simplified as a solid metallic structure.

The geometry of this test case is displayed in Figure 3.5.

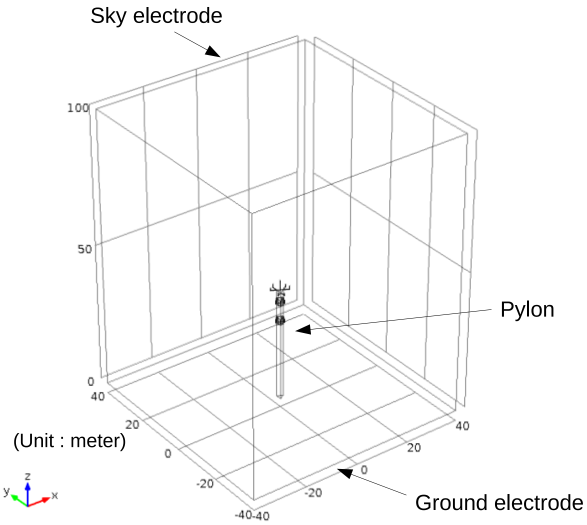

Figure 3.5: Simulation configuration in 3D.

The electrostatic simulation results are presented in Figure 3.6.

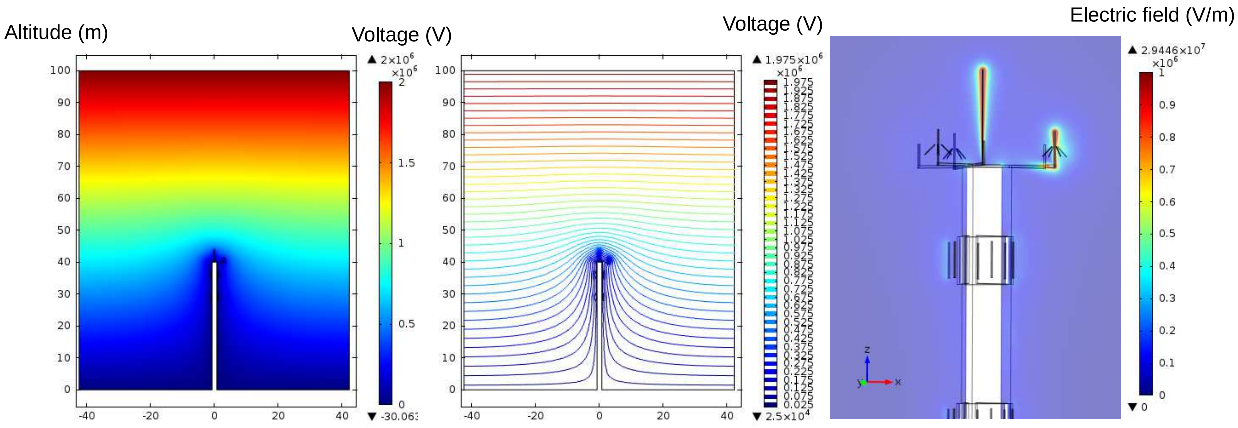

(a) (b) (c)

Figure 3.6: Simulation results in a vertical plane including the lightning conductor and a ground-plane antenna: (a) potential; (b) equi-potential lines and (c) electric field around the top of the pylon.

The simulation results show that the boundary conditions are satisfied (Figure 3.6(a) and (b)). As predicted, the electric field on top of the pylon is very strong, especially on the lighting conductor and the upper antennas. The test case seems to be physically correct.

With a standard desktop computer, the computation time of this simulation is about 15 minutes.

3.4.2 Method of validations

In the previous section, a test case has been proposed. We now want to test the different hypotheses. To achieve this, in this section, we propose a method to quantitatively evaluate their impacts on the accuracy by means of comparison with reference results.

More precisely, we here choose to compare the potentials along the segments marked in red in Figure 3.7. These segments are located along the axis of the antennas and the lightning conductor. The potentials obtained on these segments with the test case are displayed in Figure 3.8.

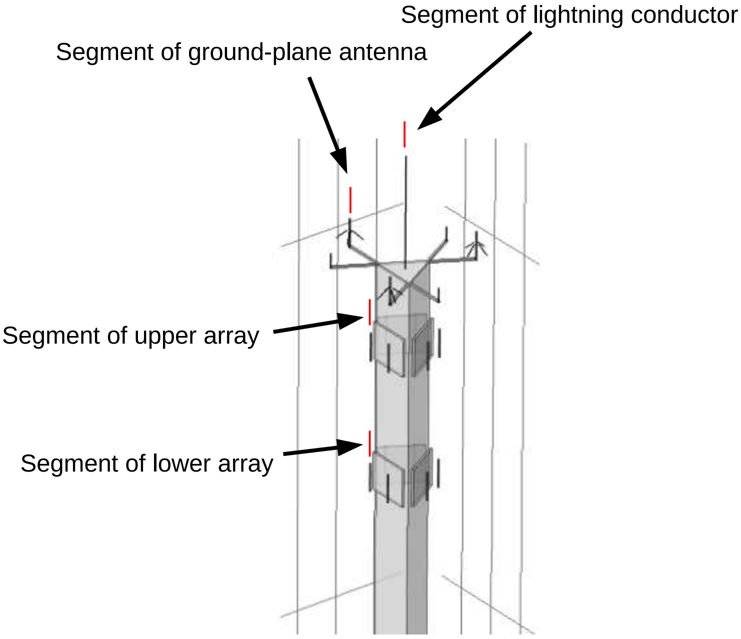

Figure 3.7: Segments where the potentials are compared.

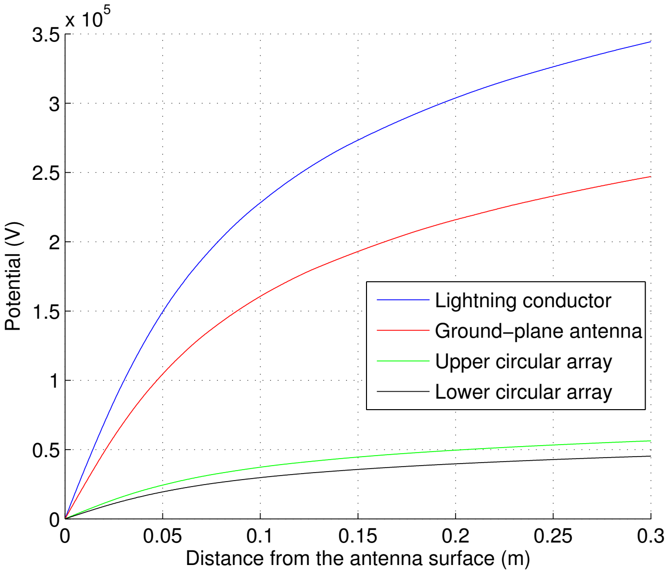

Figure 3.8: Potential along the different segments.

To describe quantitatively the difference between a simulation and a reference results, we define a normalized root mean square (rms) difference ϵ in a specified segment as

$$\epsilon = \sqrt{\frac{\sum_{i=1}^{n} \left[V(x_i) - V_{\mathrm{ref}}(x_i)\right]^2}{\sum_{i=1}^{n} V_{\mathrm{ref}}(x_i)^2}}, \tag{3.12}$$

where x_i is the position along the specified segment, n is the number of sampling points, $V(x_i)$ and $V_{\mathrm{ref}}(x_i)$ are a simulation and a reference results, respectively. We here choose $n = 100$. For $\epsilon < 0.05$, we consider that simulation results are in good agreement.

In the following section, we will apply this method to verify the following hypotheses:

- position of the lateral boundaries;
- shape and height of the sky electrode;
- removal of the building of the ground station;
- simplification of the pylon.

Note that a reference result will be defined for each simulation.

3.4.3 Tests of the hypotheses

3.4.3.a Lateral boundaries

In this section, we test the hypothesis for the position of the lateral boundaries. For the test case based on the Champcueil station, the lateral boundaries are assumed to be located 40m from the pylon.

In Section 3.3.4, we have shown that the boundary conditions at the lateral boundaries impose the electric field lines to be vertical, which can be expressed as (3.9). By the principle of image for Neauman boundary conditions, this corresponds to join image pylons (see Figure 3.9) [59].

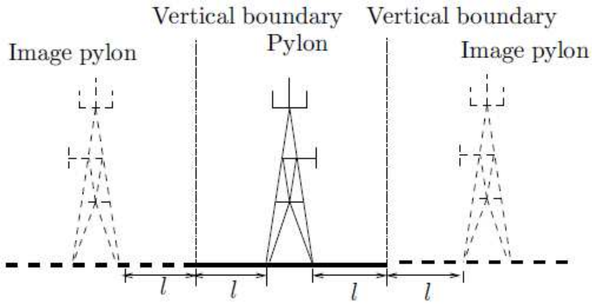

Figure 3.9: Vertical boundary and image pylon.

If the lateral size is too small, the real pylon is not far enough from its images, so that the potential around the real pylon is inevitably influenced by the images.
On the other hand, because the FEM is used to numerically solve the problem, the volume of the computation domain influences the computation time (see Section 3.2). The larger the computation domain, the longer the computation time.

Because opposite suggestions have been proposed for the location of the lateral boundaries, some simulations in 3D are necessary to obtain a trade-off for the lateral boundary position. The method of simulation is that we keep the other parameters and change the distance from the pylon to the vertical boundary l. The distances l that are tested are 10m, 20m, 30m...70m and 100m.
We here define the reference case as the case with $l = 100$m. This case should be the most accurate because its lateral boundaries are the farthest so that their influences should be the weakest.

The normalized rms differences ϵ as a function of l in all the segments are shown in Figure 3.10.

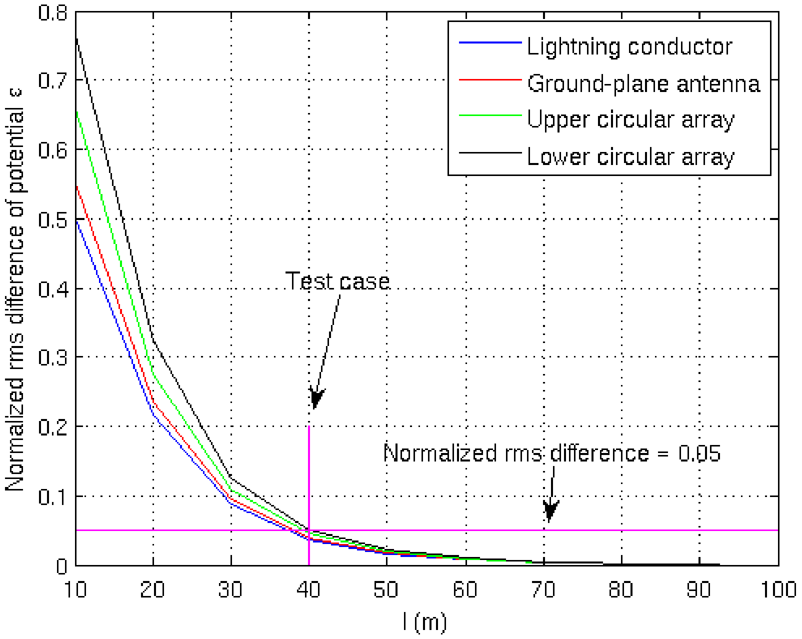

Figure 3.10: Normalized rms difference ϵ for different lateral size of the computation domain.

The Figure 3.10 shows that for $l \geq 40$m, we always have $\epsilon < 0.05$ in all the compared segments. Hence the case with $l = 40$m is the smallest one for which the simulation is in agreement with the reference.

3.4.3.b Sky electrode

In this section, we test the hypothesis for the shape and the height of the sky electrode. In the test case, the sky electrode is assumed to be represented by a planar electrode at an altitude of 100m. Firstly, we verify the shape of the electrode representing a charged cloud. Then, we test its altitude.

For the shape of the electrode, we perform electrostatic simulations to verify that when we use a different shape for the sky electrode, we can always end up with an equivalent configuration with a planar electrode. The initial sky electrode (charged cloud) is supposed to be of semi-spherical shape at an altitude of 500m. The simulation results are displayed in Figure 3.11.

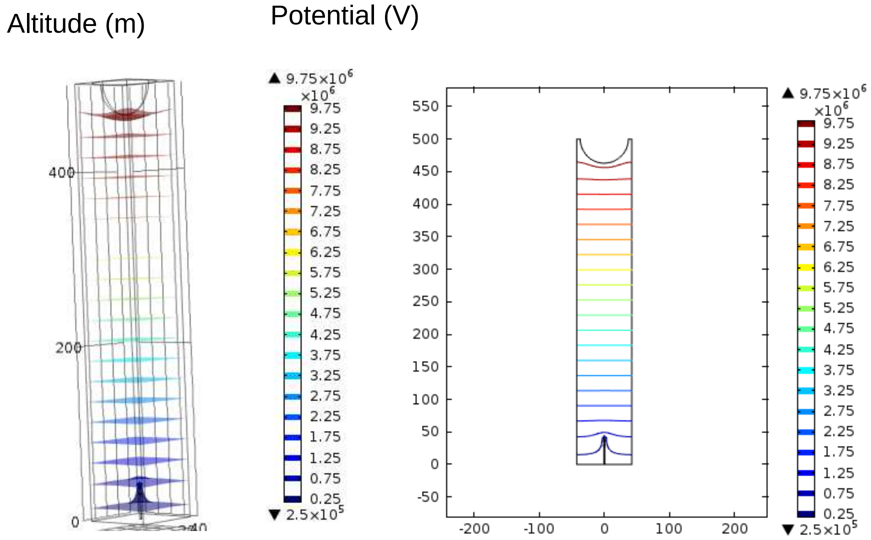

(a)

(b)

Figure 3.11: Equipotential surfaces for a charged cloud at 500m: (a) 3D; (b) vertical plane.

Figure 3.11 shows that the shape of the equipotential surfaces are similar to the electrode shape when they are near, but when they are far enough, the they become planar.
Due to the equivalence principle [59], we can replace the initial electrode by any equipotential surface with a proper potential. We can conclude that the charged cloud can be represented by a planar electrode located far enough from the pylon.

Now that the shape of the sky electrode is known, the altitude of the sky electrode h is tested. Figure 3.11 shows that when the equipotential surface is too close to the ground, its shape is influenced by the ground electrode and is thus no longer a plane. Hence the altitude h should be adjusted so that the computation volume is the smallest while keeping a satisfying accuracy.

To determine the altitude h of the sky electrode, we modify h while keeping the other

parameters unchanged. The different value of the altitude h are 60m, 70m... 100m, 120m, 160m and 200m. Note that when the altitude of the sky electrode is modified, the potential at the sky electrode is also modified according to (3.7) so that the ambient field remains constant.
We here define the reference as the case with h = 200m. This case is the most accurate because the influence of the ground is the weakest.

The normalized rms difference ϵ as a function of h is presented in Figure 3.12.

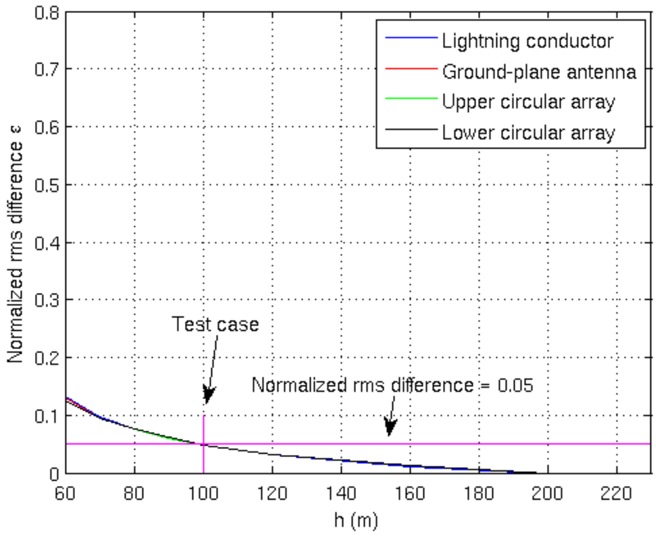

Figure 3.12: Normalized rms difference ϵ as a function of the sky electrode height h in different segments.

The comparison shows that for $h \geq 100$m, we have $\epsilon < 0.05$ so that the simulations are in agreement with the reference. As a result, the case with $h = 100$m can provide satisfying simulation results with the smallest computation domain.

3.4.3.c Building of the ground station

In this section, we test the hypothesis for the removal of the ground station building.

We use the test case to simulate the case without the building. Then we add the building of the ground station to examine its influence. Note that for the latter simulation, the equation to be solved is the equation (3.6) because the materials of the building are taken into account.

Figure 1.5 shows the building of the Champcueil ground station. We suppose that its width, length and height are 18m, 12m and 7m, respectively. This building is located about 5m from the pylon. It is made of brick with a relative permittivity ε_r of about 4.5 [60]. The modified case with the building is presented in Figure 3.13. The simulation results for the potential are displayed in Figure 3.14.

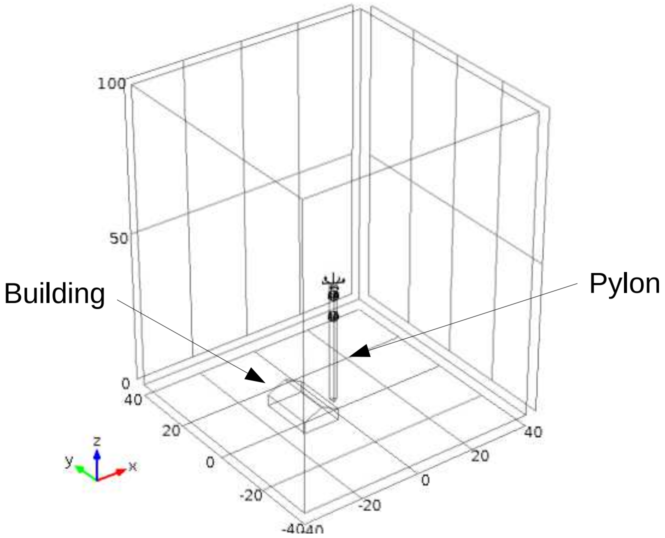

Figure 3.13: Configuration including the pylon and the building.

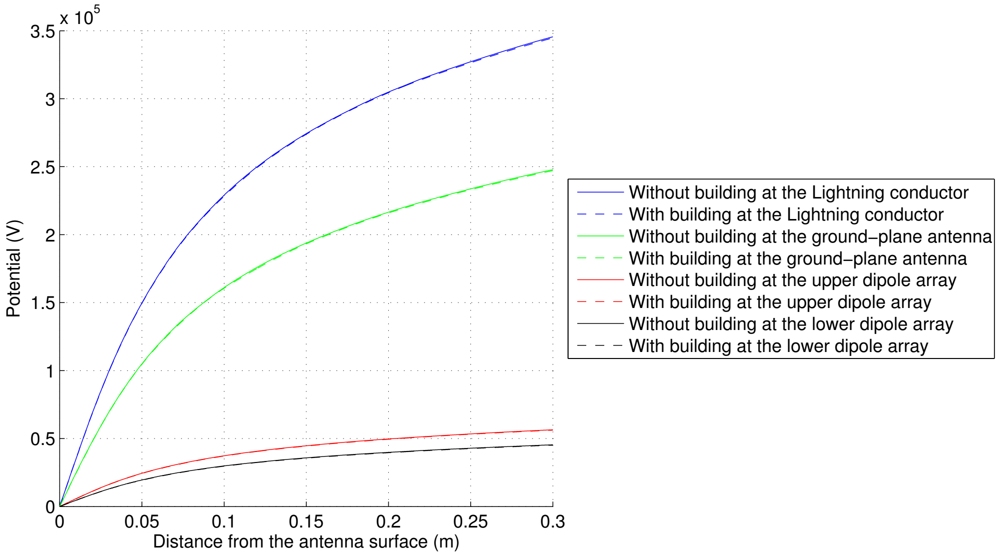

Figure 3.14: Potential with and without the ground station building in different segments.

The normalized rms differences ϵ between the cases with and without the building are presented in Table 3.1.

Lightning conductor	Ground-plane antenna	Dipole of upper circular array	Dipole of lower circular array
0.0021	0.0030	0.0049	0.0067

Table 3.1: Normalized rms difference ϵ between the cases with and without the ground station building in different segments.

The result shows that along the 4 segments, the value of ϵ does not exceed the criterion, so that the simulation results with and without the building are in good agreement. As to conclude, the building of the ground station can be ignored at the Champcueil ground station. This conclusion will also apply to any configuration where the pylon is significantly taller than the surrounding buildings.

3.4.3.d Pylon

In this section, we test the hypotheses that have been made in the test case on the pylon. They consist in assuming that the pylon can be represented by a solid metallic structure.

We perform simulations with the complex and simplified pylons while keeping the other parameters unchanged. The models of pylons are displayed in Figure 3.15.

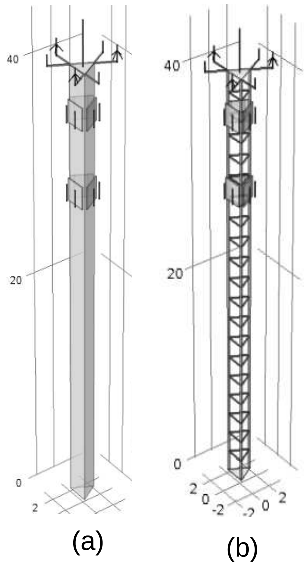

Figure 3.15: Models of the pylon: (a) simplified ; (b) complex.

The simulation results of the potential are presented in Figure 3.16.

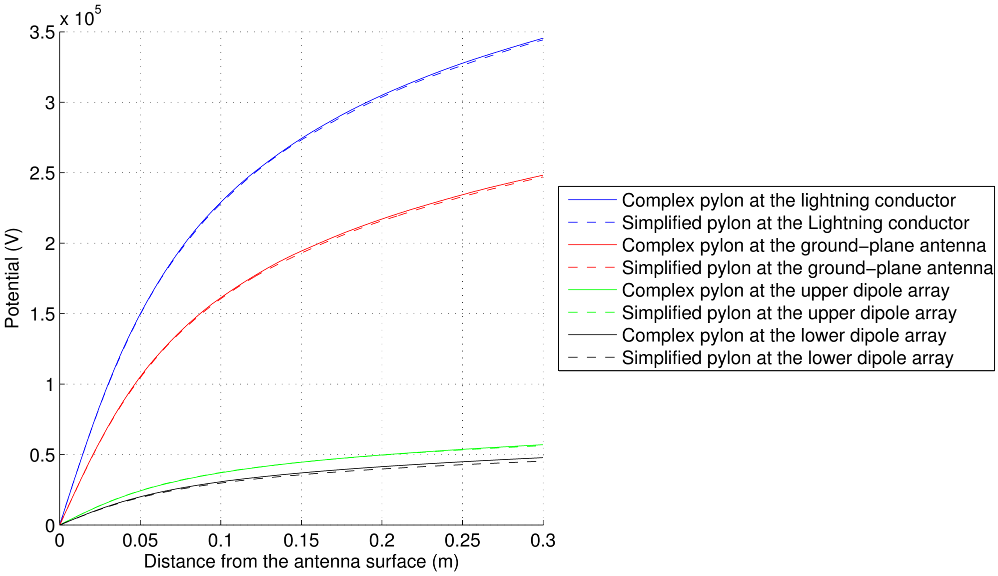

Figure 3.16: Potentials for the complex and simplified pylon.

The results of ϵ are presented in Table 3.2.

Lightning conductor	Ground-plane antenna	Dipole of upper circular array	Dipole of lower circular array
0.0039	0.0059	0.0061	0.0470

Table 3.2: Normalized rms difference of potential ϵ between the cases with the simplified and complex pylons in different segments.

The comparisons show that in the 4 segments, the difference ϵ does not exceed the criterion. Thus, we conclude that the simulation results with both pylons are in agreement.

3.4.3.e Conclusion

The model proposed in Section 3.3.6 and the corresponding hypotheses have been tested. We can finally conclude that the test case of Champcueil station proposed in Section 3.4.1 can be used for the electrostatic simulations.

3.5 Critical field of ignition

3.5.1 Principle

In the previous section, a model has been proposed to compute the electrostatic field. In this section, we propose a criterion on the computed electrostatic field to localize the places where corona discharges occur. These locations correspond to places where the electrostatic field is stronger than a critical value.

The strongest electrostatic fields occur near the sharp parts of objects, so that corona discharges most likely occur at these places. From their small radius of curvature r_{edge} (see Figure 3.17 (a)), the Peek formula (2.1) is often used to estimate an approximate value of the critical field of ignition at the surface of the sharp parts.

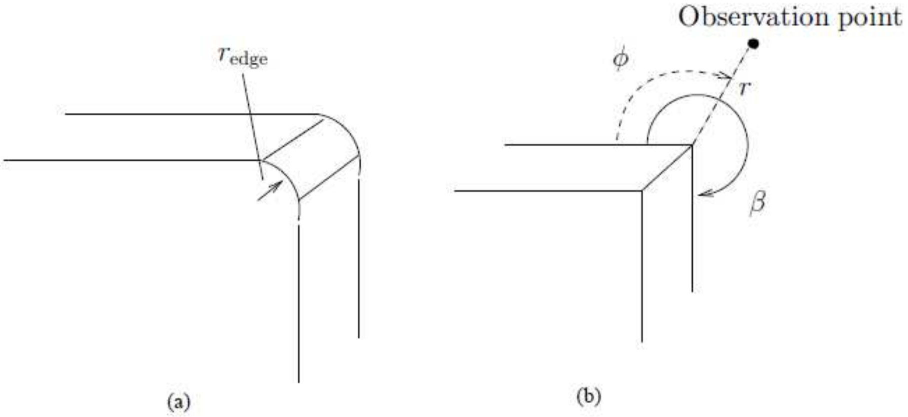

Figure 3.17: Different between: (a) a real edge and (b) a perfect edge.

However, in the electrostatic simulations presented previously in this chapter, these sharp parts are modeled as perfect edges (see Figure 3.17 (b)). There is a singularity for the electric field at the perfect edge. Thus we cannot compute the field at the edge and compare its value with the Peek formula result.

We propose here a method to determine which edges discharge for a given ambient field from the electrostatic simulation. This method is based on a theoretical analysis of the field behavior near the edge. From the critical field E_c given by the Peek formula (2.1) at the surface of the real edge, we deduce a critical field E_cd at a distance d from the edge. Then we assume that the electrostatic simulation provides an accurate field at a short distance d from the edge. By comparing this critical field with the computed field at a distance d, we determine whether an edge discharges.

3.5.2 Asymptotic field expression near the edge

Consider a perfect edge composed by two conducting plates, as shown in Figure 3.17(b). The edge angle is β. The two plates are at zero potential. The analysis in [61] shows that the electrostatic field $\mathbf{E}$ is oriented along $\hat{\phi}$, *i.e.* $\mathbf{E} = E_\phi \hat{\phi}$. Furthermore, E_ϕ and the potential V near the perfect edge are equal to

$$V(r,\phi) = \sum_{n=1}^{N} A_n \sin\left(\frac{n\pi}{\beta}\phi\right) r^{n\pi/\beta}, \tag{3.13}$$

$$E_\phi(r,\phi) = -\sum_{n=1}^{N} A_n \frac{n\pi}{\beta} \cos\left(\frac{n\pi}{\beta}\phi\right) r^{n\pi/\beta-1}, \tag{3.14}$$

with (r,ϕ) the cylindrical coordinates of the observation point (see Figure 3.17 (b)) and A_n coefficients depending on the excitation of the system [61]. The zone being studied is near the perfect edge so that the values of r are small. In this case the term with the lowest power of r ($n=1$) is dominant. Asymptotically, When $r \to 0$, V and E_ϕ can be replaced by

$$V \sim A_1 \sin\left(\frac{\pi}{\beta}\phi\right) r^{\pi/\beta}, \qquad E_\phi \sim -A_1 \frac{\pi}{\beta} \cos\left(\frac{\pi}{\beta}\phi\right) r^{\pi/\beta-1}. \tag{3.15}$$

3.5.3 Definition of the criterion

In the previous section, the variation of the electrostatic field near edges has been shown. In this section we will estimate the critical field E_cd at a distance d from the critical field at the surface of the edge.

Because the field varies as $r^{\pi/\beta-1}$, the electrostatic field at the surface of a real edge (which radius of curvature is known) E_{edge} can be estimated from the field at a point M located at d from the real edge E_{d}. The formula can be expressed as

$$\frac{E_{\mathrm{edge}}}{E_{\mathrm{d}}} = \left(\frac{r_{\mathrm{edge}}}{d}\right)^{\pi/\beta-1} . \tag{3.16}$$

The initial criterion for the ignition of corona discharges is: discharges occur at edges where the electric field at the edge E_{edge} is stronger than the critical field E_{c} obtained by means of the Peek formula. Equivalently, we can replace this criterion by another one that is consistent with our simulation: discharges occur if $E_{\mathrm{d}} > E_{\mathrm{cd}}$ with

$$E_{\mathrm{cd}} = \left(\frac{d}{r_{\mathrm{edge}}}\right)^{\frac{\pi}{\beta}-1} E_c, \tag{3.17}$$

where $E_{\mathrm{c}} = E_0\delta\left(1 + \frac{b_0}{\sqrt{\delta r_{\mathrm{edge}}}}\right)$, $b_0 = 0.308\mathrm{cm}^{1/2}$ and $E_0 = 31\mathrm{kV/cm}$ are constants, δ the ratio of air density to the normal density corresponding to $p = 760$ Torr and $T = 25°\mathrm{C}$.

With this criterion, whether corona discharges occur at an edge can be verified directly with the computed electrostatic field at a distance d from the edge.

3.5.4 Applications

A criterion has been developed in the previous section. Now we want to determine the numerical value of E_{cd} that can be applied to the Champcueil station case. To determine the value of E_{cd}, the values of r_{edge}, β and d are required.

The edges where corona discharges most likely occur are the circular edges at the ends of the metallic cylindrical components of the VHF antennas. The radius of curvature of these real edges are usually not controlled. We may reasonably assume that they are between 0.1mm and 1mm. Besides, these edges are characterized by a right angle, thus $\beta = 3\pi/2$. As a result, the potential varies as $r^{2/3}$ and the electrostatic field varies as $r^{-1/3}$. There is no singularity for the potential, and a singularity in $r^{-1/3}$ for the electrostatic field at the perfect edge. At last, the value of d is chosen to be 1cm.

With (2.1), we evaluate the critical field of ignition E_c for the real edges with radius of curvature between 0.1mm and 1mm. We also evaluate the values for E_{cd} from (3.16). They are presented in Table 3.3.

Radius of curvature (mm)	Critical field E_{c} at the real edge (MV/m)	E_{cd} for $d = 1$cm (MV/m)
1	6.12	2.84
0.5	7.37	2.71
0.2	9.85	2.67
0.1	12.6	2.72

Table 3.3: Critical fields of ignition E_{c} and E_{cd} for different radius of curvature.

Table 3.3 shows that when the radius of curvature of the real edges changes, the critical field of ignition E_{c} at the surface of the real edge is different. However the associated value of E_{cd} are almost the same. This may be explained by the fact that, to generate corona discharges, there should be a layer of a certain thickness (a few millimeters or more) in which the electrostatic field is strong enough to ignite the avalanche. As a result, in the following section, we consider $E_{\mathrm{cd}} = 2.84$MV/m as the critical field at a distance of $d = 1$cm for the ignition of corona discharges.

3.6 Simulation to localize corona discharges

In the previous sections, we have tested the model for the electrostatic simulation, and proposed a criterion to localize corona discharges. In this section, we localize the places where corona discharges occur in our test case *via* electrostatic simulations.

To perform the simulation, the potential difference between the electrodes (the ground and the sky electrodes) is essential. This can be evaluated *via* (3.7) for a known ambient field. We perform simulations for the Champcueil case with the strongest ambient field

because in this case, corona discharges occur at most places.
For the case of Champcueil station, we have used a field mill to measure the electrostatic field. During the measurement, the strongest field $E_{\mathrm{measured}} = 20\mathrm{kV/m}$ occurs at 4:20 on August 2, 2007. Because the field mill is placed near the pylon, the measured electrostatic field may be different from the ambient field. A method to determine the ambient field E_{amb} from the field measured by the field mill E_{measured} is proposed in Appendix D. This method yields $E_{\mathrm{amb}} = E_{\mathrm{measured}}/0.8$, so that the strongest ambient field observed at the Champcueil station is $E_{\mathrm{amb}} = 25\mathrm{kV/m}$.

An analysis of the simulation results with this ambient field shows that the strongest electrostatic fields are at the following locations:

- top of the lightning conductor;
- top of the monopole and end of the downward sticks of the ground-plane antennas;
- top of the UHF antennas;
- upper and lower ends of the dipoles of the circular arrays.

The locations listed above are mostly of cylinder shape. On such structures corona discharges most likely occur at the circular edges located at both ends of the cylinders. Hence, we study the variation of the electric field near these edges along two directions: an axial and a radial directions as indicated in Figure 3.18.
The electric field at these places are displayed in Figure 3.19 and 3.20.

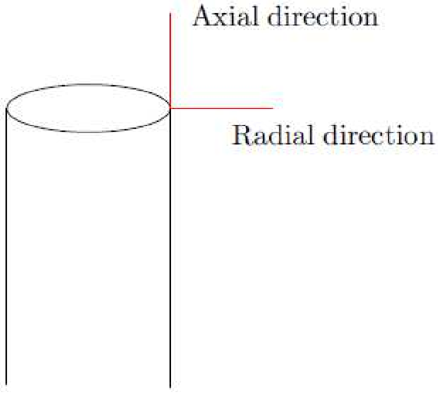

Figure 3.18: Positions on which the electric field around the edges is displayed.

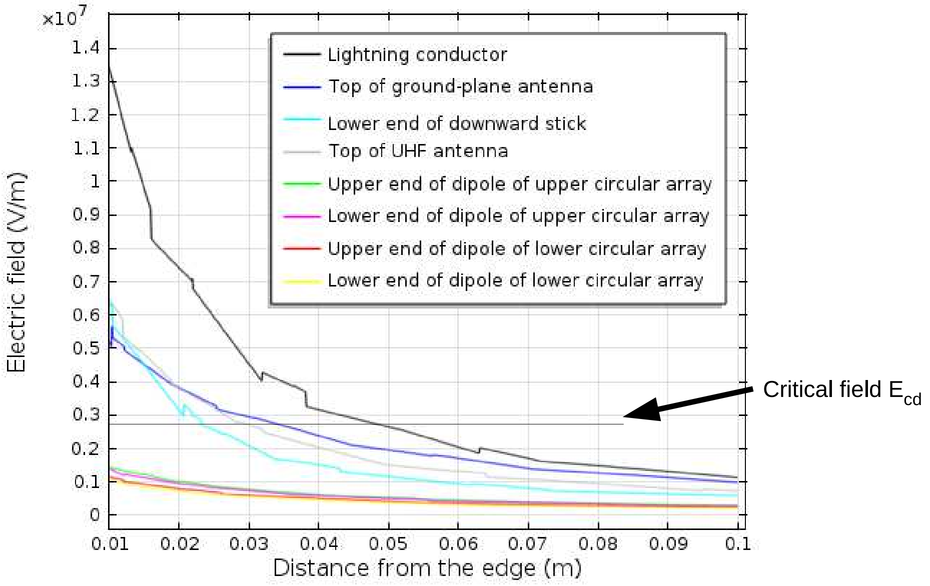

Figure 3.19: Electric field in different places in the axial direction.

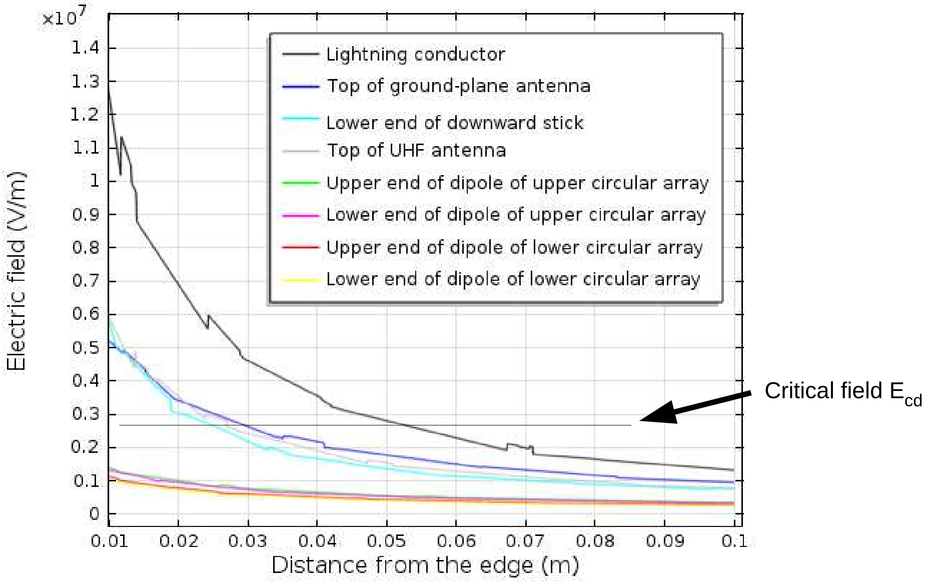

Figure 3.20: Electric field in different places in the radial direction.

Comparing Figure 3.19 and 3.20, we find that the relative difference between the electrostatic fields in the axial and radial directions are smaller than 10%. To simplify the presentation, we can thus limit the study to the electrostatic field in the axial direction.

The electric field at $d = 1$cm from the edges E_d in different places are compared with the corresponding critical field of ignition in Table 3.4.

Location	Electrostatic field E_d at 1cm from the edge (MV/m)	$E_\mathrm{d}/E_\mathrm{cd}$
Top of lightning conductor	13.5	4.75
Top of monopole of ground-plane antenna	5.8	2.04
End of downward stick of ground-plane antenna	6.5	2.28
Top of UHF antenna	6.5	2.28
Upper end of dipoles of upper circular array	1.5	0.53
Lower end of dipoles of upper circular array	1.4	0.49
Upper end of dipoles of lower circular array	1.2	0.42
Lower end of dipoles of lower circular array	1.1	0.39

Table 3.4: Electrostatic field at different locations with an ambient field of 25kV/m.

With this particular ambient field, the critical field of ignition is reached at the following locations:

- top of the lightning conductor;
- tops of monopole of the ground-plane antennas;
- lower ends of downward sticks of the ground-plane antennas;
- tops of the UHF antennas.

For different values of ambient field, the locations where corona discharges occur will change. However, from Table 3.4, we can define groups of locations for which the discharges occur from the same value of ambient field. As expected, these groups are directly related to their positions on the pylon. The higher the position, the weaker the ambient field that triggers discharges. These groups are listed in Table 3.5.

No.	Locations where corona discharges occur simultaneously
1	Top of lightning conductor
2	Top of lightning conductor, Lower ends of downward sticks, Tops of the ground-plane antennas and UHF antennas
3	Top of lightning conductor, Lower ends of downward sticks, Tops of the ground-plane antennas and UHF antennas, End of dipoles of the upper circular array of dipoles, End of dipoles of the lower circular array of dipoles

Table 3.5: Groups of corona discharges occurring simultaneously.

3.7 Conclusion

The problem of localizing the places of corona discharges has been formulated and simplified. A test case has been proposed and tested for the electrostatic simulations. A criterion to localize corona discharges has been developed. The places where corona discharges most likely occur have been determined. Finally, we have defined groups of locations for which the discharges occur from the same value of ambient field.

Chapter 4

Source representing the corona VHF radiation

In Chapter 2, we have presented the physical characteristics of corona discharges. In Chapter 3, the locations where such discharges most likely occur have been estimated *via* electrostatic simulations. To evaluate the interference introduced by these discharges, we need to study their radiation in the aeronautical VHF band. The objective of this chapter is to find a source that can represent this radiation in the VHF band.

In Section 4.1, an elementary dipole model is proposed. We verify its capability to represent corona discharges in the VHF band by simulations. In Section 4.2, the amplitude of the elementary dipole source is studied accordingly with the discharge characteristics. The evaluation is performed *via* a deterministic and a statistical approaches.

4.1 Elementary dipole source

In this section, we present and test an elementary dipole model to represent the radiation of corona discharges. We here work in the frequency domain. Note that in the time and frequency domains, the currents are denoted i and I, respectively.

A localized electric source, also called an elementary dipole, corresponds to a distribution of impressed electric currents in a homogeneous domain Ω of size much smaller than the wavelength λ. Its amplitude is defined by $I\delta\mathbf{l}$ where

$$I\delta\mathbf{l} = \iiint_{\Omega} \mathbf{J}_{\mathrm{e}}(r')d\Omega(r'), \tag{4.1}$$

with $\mathbf{J}_{\mathrm{e}}(r')$ the electric current density. For corona discharges, Ω is the zone in which the corona discharge currents concentrate.

The elementary dipole has already been proposed as a model to represent the radiation of corona discharges in the VHF band [24, 62, 63, 64]. In this section, the radiation of the elementary dipole is explained, and its validity for representing corona discharges is verified.

4.1.1 Radiation of the elementary dipole in-free space

We consider an elementary dipole vertically polarized, *i.e.* oriented along the z axis, and centered at the origin. In spherical coordinates, each component of the fields radiated in free-space by this source are [28]

$$E_r = \zeta \frac{I\delta l e^{-jkr}}{2\pi r^2}\left(1 + \frac{1}{jkr}\right)\cos\theta, \tag{4.2}$$

$$E_\theta = jk\zeta \frac{I\delta l e^{-jkr}}{4\pi r}\left(1 + \frac{1}{jkr} - \frac{1}{k^2 r^2}\right)\sin\theta, \tag{4.3}$$

$$H_\phi = jk \frac{I\delta l e^{-jkr}}{4\pi r}\left(1 - \frac{j}{kr}\right)\sin\theta, \tag{4.4}$$

$$E_\phi = H_r = H_\theta = 0, \tag{4.5}$$

with $k = 2\pi/\lambda$ the wavenumber, ζ the impedance of free space, (r, θ, ϕ) the spherical coordinates of the observation point. Note that the fields radiated by the elementary dipole are proportional to the amplitude $I\delta l$.

When the observation point is in the very near-field region ($kr << 1$), the terms with the highest order of $1/(kr)$ are dominant. Hence, the fields radiated in free-space can be approximated by

$$E_r \simeq -j\zeta \frac{I\delta l e^{-jkr}}{2\pi k r^3} \cos\theta, \tag{4.6}$$

$$E_\theta \simeq -j\zeta \frac{I\delta l e^{-jkr}}{4\pi k r^3} \sin\theta, \tag{4.7}$$

$$H_\phi \simeq \frac{I\delta l e^{-jkr}}{4\pi r^2} \sin\theta, \tag{4.8}$$

$$E_\phi = H_r = H_\theta = 0. \tag{4.9}$$

When the observation point is in the far-field region, the terms in $1/(kr)^2$ and $1/(kr)^3$ are negligible compared to the terms in $1/kr$. Thus, the fields can be approximated by

$$E_\theta \simeq jk\zeta \frac{I\delta l e^{-jkr}}{4\pi r} \sin\theta, \tag{4.10}$$

$$H_\phi \simeq jk \frac{I\delta l e^{-jkr}}{4\pi r} \sin\theta, \tag{4.11}$$

$$E_r \simeq E_\phi = H_r = H_\theta = 0. \tag{4.12}$$

This approximation holds for $kr \gg 1$. To have a relative error less than 0.05, this means that r should be larger than 3λ.

For a frequency of 120MHz, the radiation in the near-field and far-field zones are presented in Figure 4.1 (a) and (b), respectively.

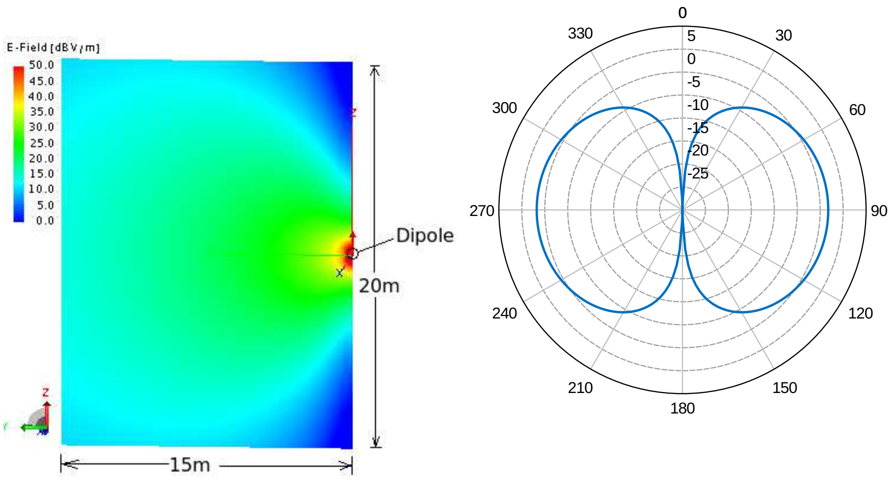

(a) (b)

Figure 4.1: Radiation of an elementary dipole in the vertical plane at a frequency of 120MHz: (a) in the near-field region; (b) in the far-field region.

In our context, corona discharges occur on pylons, notably on the surface of the antennas. The elementary dipoles that represent corona discharges must be placed at these locations. Thus, the radiation of corona discharges must be computed taking into account the near-field coupling between the elementary dipole and the pylon geometry.

4.1.2 Verification of the elementary dipole model

Corona discharges appear in regions where the electrostatic field is strongly non-uniform. This usually corresponds to places near conductors with large curvature such as tips or edges. In this section, the capability of the elementary dipole source to represent the corona discharge radiation is tested.

When corona discharges appear on a sharp active electrode, the currents around the active electrode are as presented in Figure 4.2(a). $\mathbf{J}_{\mathrm{e}}$ is the current density of the discharge, $\mathbf{J}_{\mathrm{es}}$ is the induced surface current density that flows along the active electrode.

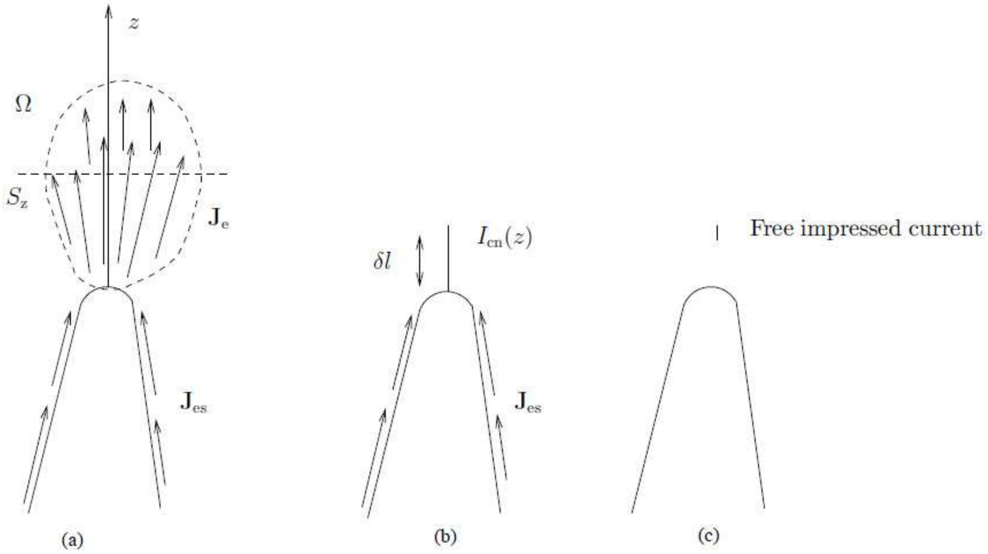

Figure 4.2: Different models of corona currents: (a) real case; (b) impressed current connected to the electrode; (c) free inmpressed current.

To calculate the induced current $\mathbf{J}_{\mathrm{es}}$, two phenomena should be taken into account: the coupling by radiation between the discharge currents $\mathbf{J}_{\mathrm{e}}$ and the electrode, and the current conservation at the top of the electrode.

Corona discharge currents usually concentrate in an area around the active electrode, so that the dimension of the corona region (few centimeters) is much smaller than the wavelength in the VHF band (2 to 3 meters). Hence, the discharge current density $\mathbf{J}_{\mathrm{e}}$ can be represented by an impressed current $I_{\mathrm{cn}}(z)$ connected to the electrode (see Figure 4.2 (b)). This first source is denoted with the subscript *cn* and is given by

$$I_{\mathrm{cn}}(z) = \iint_{S_{\mathrm{z}}} \mathbf{J}_{\mathrm{e}} \cdot \mathrm{d}\mathbf{S}, \tag{4.13}$$

with S_{z} the horizontal plane of height z. The discharge current density is supposed to mainly flow along the vertical direction, so that the impressed current is vertically oriented. Two physical principles determine the variation of $I_{\mathrm{cn}}(z)$ with respect to the distance to the active electrode. Firstly, on top of the electrode, the current conservation should be guaranteed between $\mathbf{J}_{\mathrm{es}}$ and $I_{\mathrm{cn}}(z)$. Secondly, while the current is flowing away from the active electrode, the charge carriers diffuse and drift to the other electrode and the current density reduces towards zero. So does the impressed current $I_{\mathrm{cn}}(z)$. Finally, we choose $I_{\mathrm{cn}}(z)$ as displayed in 4.3(a).

Now we want to verify whether this impressed current can be replaced by another impressed current that is not connected to the electrode, called a free impressed current and denoted $I_{\mathrm{fr}}(z)$. As displayed in 4.2 (c), this free impressed current is in an homogeneous domain of size much smaller than λ. Thus it corresponds to an elementary dipole of amplitude $I\delta l = \int_0^{\delta l} I_{\mathrm{fr}}(z)dz$. For a free impressed current, no conservation law is imposed between $\mathbf{J}_{\mathrm{es}}$ and $I_{\mathrm{fr}}(z)$. We here choose $I_{\mathrm{fr}}(z)$ as displayed in 4.3(b).

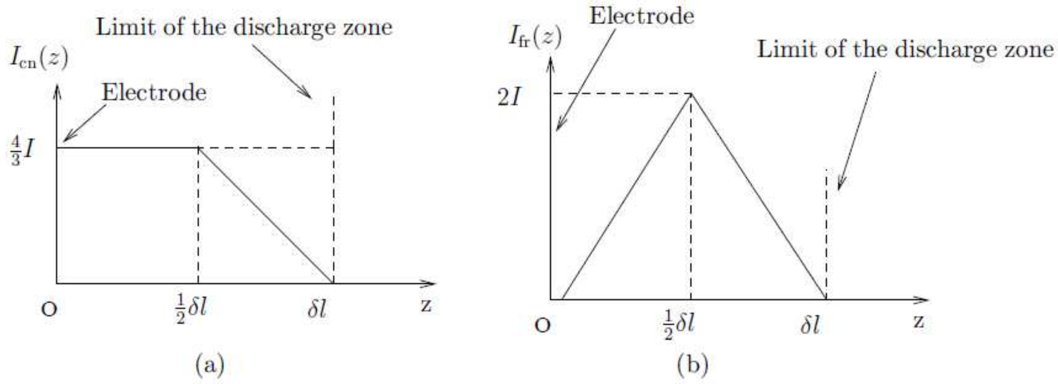

Figure 4.3: Impressed currents: (a) connected to the electrode; (b) not connected.

We perform simulations to verify whether the three previous sources, namely the connected impressed current, the free impressed current and the elementary dipole yield the same radiation. These simulations are realized *via* the commercial software Feko which is mainly based on integral-equations. The integral-equations method will be presented in Section 5.1. They consist in numerically solving the problem to determine the value of $\mathbf{J}_{\mathrm{es}}$. Then the complete radiation is obtained by summing the radiation of the source and $\mathbf{J}_{\mathrm{es}}$.

We here consider the three previous sources placed vertically on top of a metallic halfwave dipole antenna which impedance is matched at 120MHz (see Figure 4.4). To obtain comparable results, the amplitude of the connected/free impressed currents and the elementary dipole are normalized, so that for all of them, we have

$$\int_0^{\delta l} I_{\mathrm{cn}}(z)dz = \int_0^{\delta l} I_{\mathrm{fr}}(z)dz = I\delta l. \tag{4.14}$$

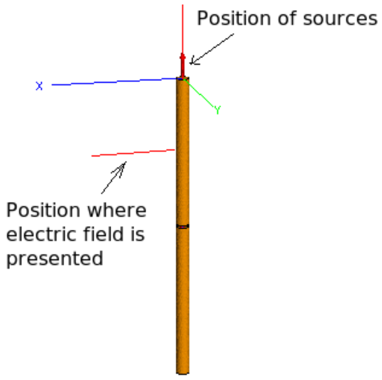

Figure 4.4: Configuration of the simulations.

For the three sources, the electric field in the near-field zone and the power received at the antenna port are displayed in Figure 4.5. The electric field in the near-field zone is presented along a radial line perpendicular to the dipole in the middle of the upper part (see Figure 4.4).

The simulation results show that at the port of the halfwave dipole, the powers received for the three sources are the same. Indeed, the differences are smaller than 0.3dB. The electric fields in the near-field zone is also the same. Thus, we conclude that the impressed current connected to the electrode can be replaced by an elementary dipole with the same amplitude. Hence, the elementary dipole can represent the radiation of corona discharges in the VHF aeronautical band.

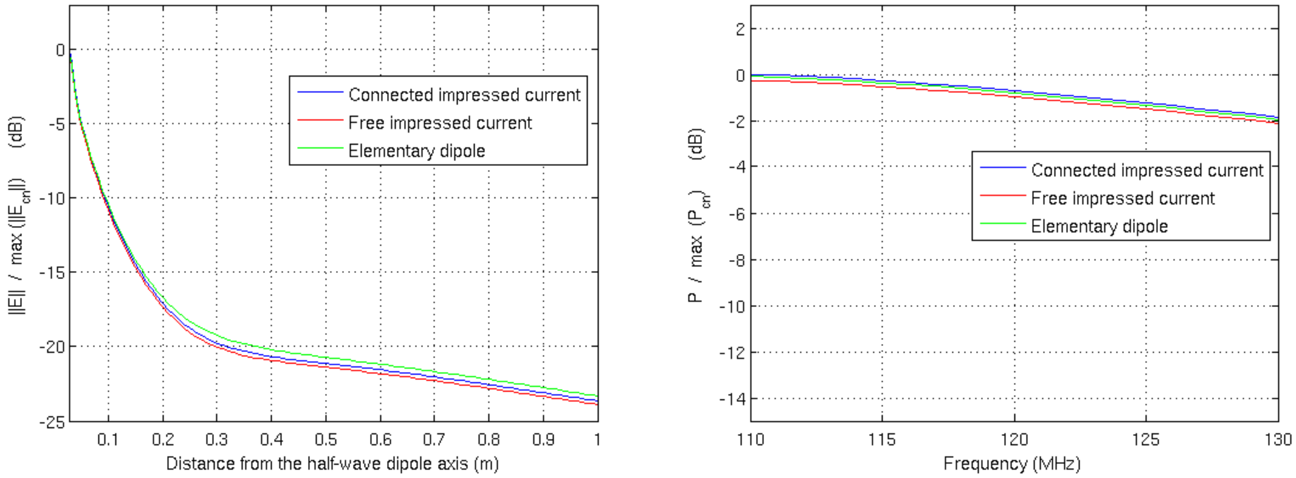

(a) (b)

Figure 4.5: Simulation results for: (a) the electric field in the near-field zone; (b) the power received at the antenna port.

4.2 Spectral characteristics of the corona current

4.2.1 Introduction

In the previous section, the elementary dipole model has been presented and tested. In this section, we determine the spectral properties of the elementary dipole amplitude.

The radiation of corona discharges constitutes a wide-band interference noise. This kind of noise has been widely studied [10, 24, 34]. As many other noises of natural origin, it can be classified as a Class B noise as defined by Middleton [65] because the pulse duration is very short and the radiation of corona discharges is wide-band.

We here study the elementary dipole amplitude at one single discharge location. The effect of several discharge locations will be presented in Section 5.5.

In the time domain, we note $s(t) = i(t)\delta l$ with $i(t)$ the current of a series of corona pulses. The objective of this section is to deduce the characteristics of s in the VHF band from the discharge properties presented in Section 2.3.2. The spectrum of s is characterized by its power spectral density $S_{\mathrm{ss}}(f)$. The mean square value of s on a band B is

$$< s^2 >_B = \int_B S_{\mathrm{ss}}(f) df. \tag{4.15}$$

In the following parts, we estimate the spectral density and the mean square value of s with two different approaches. At first, a deterministic approach is used: we suppose corona discharges are strictly periodic: the amplitude, the pulse shape, the discharge size and the repetition rate remain constant. This approach is not realistic but may be sufficient to determine an approximate mean square value of s. Then we apply a statistical approach by supposing that both the amplitude of corona discharges and the interval between pulses are random variables.

4.2.2 Deterministic approach

As presented in Chapter 2, the current of corona discharges is a series of pulses. Hence, for a single pulse, $s_{\mathrm{p}}(t)$ can be expressed as:

$$s_{\mathrm{p}}(t) = i_{\mathrm{p}}(t)\delta l = K i_{\mathrm{max}} \delta l \left(e^{-\alpha t} - e^{-\beta t}\right), \tag{4.16}$$

with $i_{\mathrm{p}}(t)$ the current of a single pulse, i_{max} the maximal amplitude of the pulse, α, β and K constants. For positive and negative corona, the parameters α, β and K have been presented in Section 2.3.2.b. For the value of δl, in Section 2.3.2.f, we have explained that the dimension of the zone inside which the corona currents concentrate is about few centimeters. We here consider that δl is about 2cm.

In this section, we suppose that the pulses of corona discharges are strictly periodic: their amplitude and period are constant. Thus, $s(t)$ can be expressed as

$$s(t) = \sum_{n \in \mathbb{Z}} s_{\mathrm{p}}(t - nT_{\mathrm{r}}) = \sum_{n \in \mathbb{Z}} i_{\mathrm{p}}\left(t - nT_{\mathrm{r}}\right) \delta l, \tag{4.17}$$

with $T_\mathrm{r} = 1/R_\mathrm{r}$ the period of corona pulses, and R_r the repetition rate of corona discharges. Figure 4.6 shows $s_\mathrm{p}(t)$ and $s(t)$ for negative corona discharges. For positive corona discharges, the pulses are similar but with different amplitude and repetition rate.

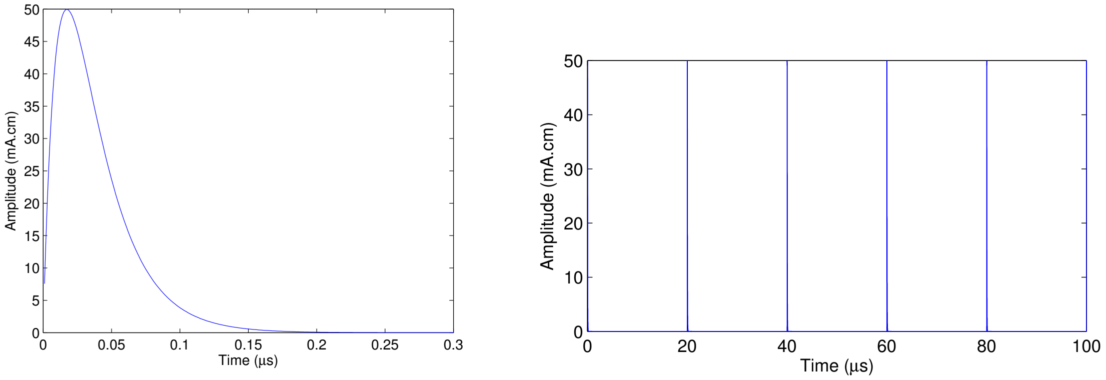

(a) (b)

Figure 4.6: Amplitude of $i\delta l$ for: (a) one pulse; (b) a series of pulses.

The spectrum of $s(t)$, noted $\hat{s}(f)$, can be expressed as

$$\hat{s}(f) = \frac{\hat{s}_\mathrm{p}(f)}{T_\mathrm{r}} \sum_{n\in\mathbb{Z}} \delta\left(f - \frac{n}{T_\mathrm{r}}\right), \tag{4.18}$$

with $\delta(f)$ the Dirac delta function, and $\hat{s}_\mathrm{p}(f)$ the spectrum of one pulse defined by

$$\hat{s}_\mathrm{p}(f) = \int_{-\infty}^{+\infty} s_\mathrm{p}(t) e^{-j2\pi f t} \mathrm{d}t. \tag{4.19}$$

From [66], $S_\mathrm{ss}(f)$ (power spectral density of $s(t)$) can consequently be expressed as

$$S_\mathrm{ss}(f) = \frac{|\hat{s}_\mathrm{p}(f)|^2}{T_\mathrm{r}^2} \sum_{n\in\mathbb{Z}} \delta\left(f - \frac{n}{T_\mathrm{r}}\right), \tag{4.20}$$

The spectrum of a single pulse, that has the same properties as $\hat{s}(f)$, has been studied in Section 2.3.2.c. It is continuous and wide band. Besides, the low frequency part is much stronger than the high frequency part.

The power spectral density of a series of negative corona discharges $S_{\mathrm{ss}}(f)$ is presented in Figure 4.7. Due to the periodicity of s, it is a series of Dirac with a constant frequency sampling. For positive corona discharges, the result is similar but the frequency sampling is shorter due to their longer period.

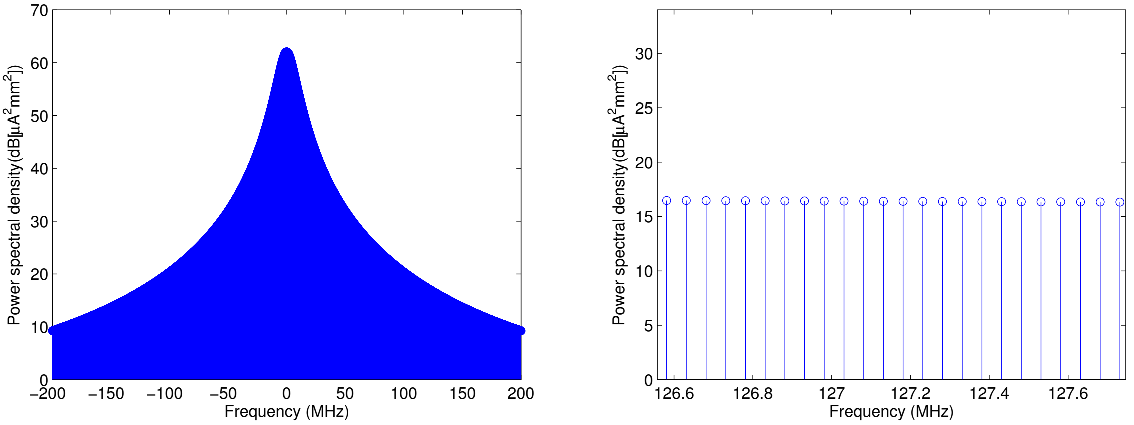

(a) (b)

Figure 4.7: Power spectral density of a series of negative corona discharges $S_{\mathrm{ss}}(f)$ on: (a) a large band; (b) a narrow band.

We now calculate the mean square value of s in the entire VHF aeronautical band B_{a}. For both positive and negative frequencies, from (4.15), we obtain

$$< s^2 >_{B_{\mathrm{a}}} = \int_{B_{\mathrm{a}}} S_{\mathrm{ss}}(f)\mathrm{d}f = \frac{1}{T_{\mathrm{r}}^2} \sum_{\frac{|n|}{T_{\mathrm{r}}} \in B_{\mathrm{a}}} \left| \hat{s}_{\mathrm{p}} \left(\frac{n}{T_{\mathrm{r}}} \right) \right|^2 . \tag{4.21}$$

The average value on a voice communication channel B_{c} is thus

$$< s^2 >_{B_{\mathrm{c}}} = \frac{B_{\mathrm{c}}}{B_{\mathrm{a}}} < s^2 >_{B_{\mathrm{a}}} . \tag{4.22}$$

We have presented the parameters α, β and K of corona discharges in Table 2.3. We here choose the average level of the pulse amplitude and the repetition rate to estimate the RMS value of s in a voice channel B_{c}. The results are presented in Table 4.1.

Parameters	Positive corona	Negative corona
Pulse amplitude (mA)	60	25
Repetition rate (kHz)	2	50
$\sqrt{< s^2 >_{B_\mathrm{c}}}$ (μA · mm)	0.694	3.97

Table 4.1: Root mean square value of $I\delta l$ on a band B_c for corona discharges.

4.2.3 Statistical approach

In the previous section, corona discharge pulses are supposed to be strictly periodic so that both the amplitude and the period of the corona pulses are the same. The spectral density of the noise is thus expressed as a series of Dirac. This hypothesis is not realistic because in reality, neither the amplitude nor the period are constant. In this section we estimate the power spectral density and rms value of $i\delta l$ on a band B_c with a more physical and realistic model.

4.2.3.a Model of the statistical approach

We here consider a series of pulses with random time separations and amplitudes.

In a series of corona pulses, we can assume that there exists a minimal duration between two consecutive pulses. Hence each corona pulse consists in a fixed pulse frame plus a variable pulse separation. This leads to the following statistical model. We consider that the time between pulses is a random variable of mean $T_\mathrm{r} = 1/R_\mathrm{r}$. More precisely, as shown in Figure 4.8, we assume that the pulse frames have the same duration ηT_r with $\eta < 1$. They are separated by inter-arrival times that are described by a Poisson process of parameter λ. This parameter describes the separation time of the pulse events. The initial time of the first pulse also follows a Poisson process of parameter λ. To have a mean period of T_r, we must choose $\lambda = R_\mathrm{r}/(1-\eta)$. The parameter η is here chosen to be 0.9.

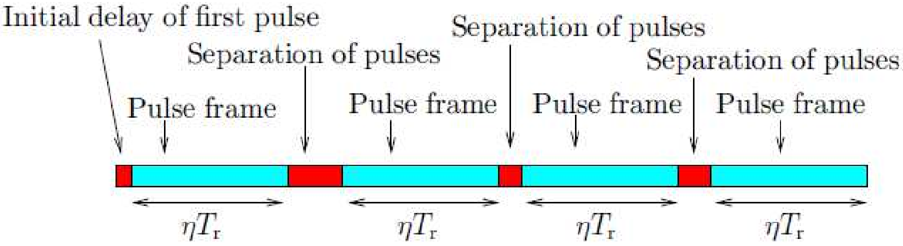

Figure 4.8: Corona pulse series with the statistical approach.

For the amplitude, in [67], it has been shown that the amplitudes of corona discharges are variant and that they roughly obey a Gaussian distribution. Hence, we suppose that the peak values of corona pulses obey a Gaussian distribution, which mean μ is the same as the average pulse amplitude used in Section 4.2.2. The standard deviation σ is chosen to be 10% of the mean amplitude, *i.e.* $\sigma = \mu/10$.

Similarly, we suppose that δl also obeys a Gaussian distribution. Its mean is the value used in Section 4.2.2. Its standard deviation is chosen to be 10% of the mean.

With the previous hypotheses, we can generate discrete time series with variable pulse separations and amplitudes. For a sampling frequency of 1GHz and a duration of 0.01s, an example of such discrete time series for positive discharges is presented in Figure 4.9 (a). For comparison, a purely periodic series with the same repetition rate and average pulse amplitude is presented in Figure 4.9 (b). For negative discharges, the corresponding series are similar but with different amplitudes and repetition rates.

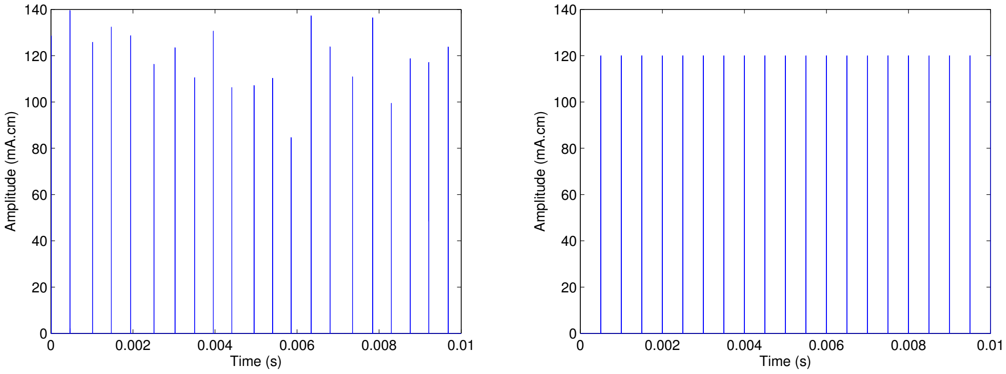

(a) (b)

Figure 4.9: Examples of $s(t)$ of positive discharges with the same pulse repetition rate and average pulse amplitude: (a) statistical series; (b) deterministic series.

4.2.3.b Estimation of the power spectral density *via* the modified periodogram

With the statistical approach, a more realistic spectral density can be computed from the discrete time series.

In the previous section, we have generated a deterministic and a statistical time series. A discrete Fourier transform of these time series could be used to estimate the power spectral density. We use a more efficient method known as the modified periodogram [68]. In this method, the power spectral density is estimated using Welch's overlapped segment averaging estimator: The time series is divided into 8 segments with 50% overlap, and each segment is windowed with a Hamming window. The power spectral density is computed for each segment and the average level of the 8 segments is estimated as the final result. The estimated power spectral densities are presented in Figure 4.10.

For the deterministic case, the power spectral density has been theoretically studied in Section 4.2.2. It is a series of Dirac. The estimator shows the same result but with the influence of the sampling and windowing.

For the statistical case, Figure 4.10 shows that the power spectral density of the statis-

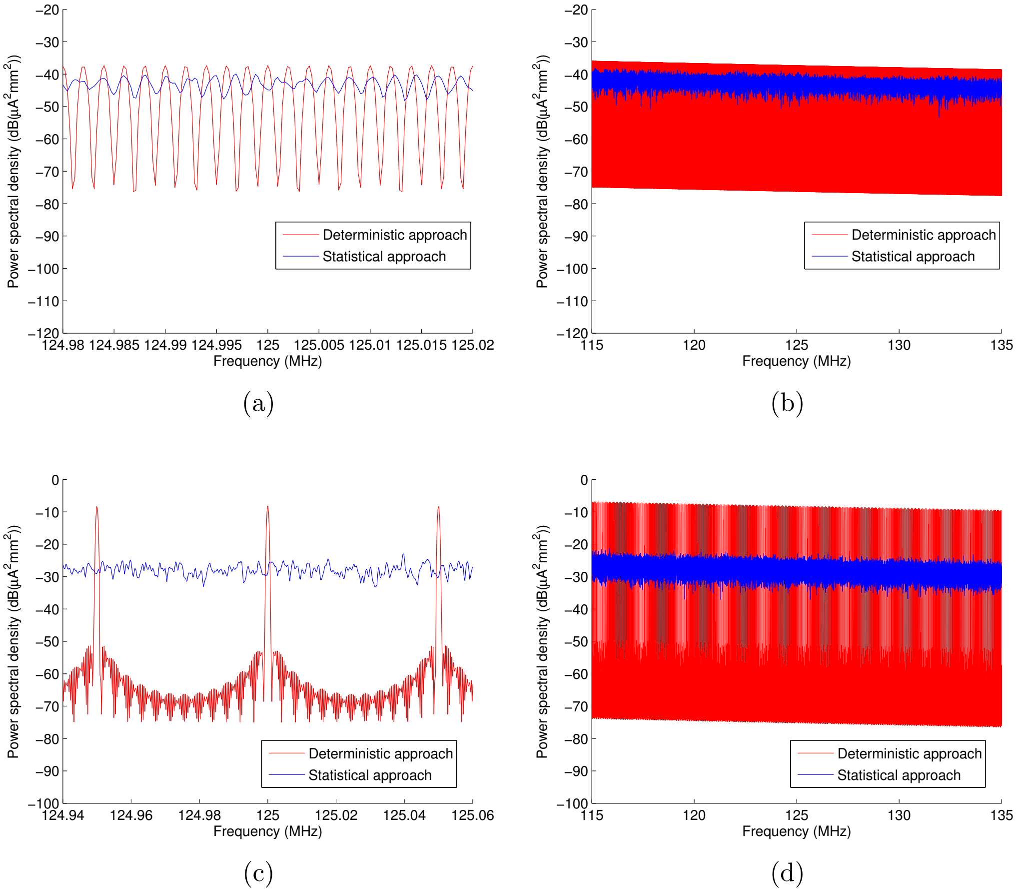

Figure 4.10: Estimation of the power spectral density of corona discharges: (a) positive on a narrow band; (b) positive on the VHF band; (c) negative on a narrow band; (d) negative on the VHF band.

tical series is quasi-constant in the VHF band. The mean square value of s on a voice channel can be estimated *via* (4.15). It is about $0.679\mu\text{A}\cdot\text{mm}$ for corona positive, and $3.82\mu\text{A}\cdot\text{mm}$ for negative corona.

Compared with the deterministic result shown in Section 4.2.2, the differences between the deterministic and the statistical approaches are weak. They are of 0.18dB and 0.33dB for positive and negative corona discharges, respectively. This is because the average values of the pulse amplitudes and separations in the statistical approach correspond to the constant values of these parameters in the deterministic approach.

4.3 Conclusion

We have proposed an elementary dipole source. The elementary dipole model has been presented and tested. It can represent the radiation of corona discharges in the VHF band. The amplitude of the elementary dipole model has been determined *via* a deterministic and a statistical approaches based on the characteristics of corona discharges.

Chapter 5

Simulations in the frequency domain

In Chapter 3, the places where corona discharges most likely occur have been determined. In Chapter 4, it has been shown that, in the VHF band, the radiation of corona discharges can be represented by an elementary electric dipole. In this chapter, the aim is to perform simulations in the frequency domain to estimate the noise power introduced by corona discharges.

To perform the simulations in the frequency domain, we present the numerical method in Section 5.1 and the models for the VHF antennas in Section 5.2. Then, in Section 5.3, we define a reference noise level corresponding to the typical noise induced by classical sources of noise. In Section 5.4, we perform simulations to evaluate the interference level induced by each corona discharge location. At last, the interference levels introduced by corona discharges simultaneously occurring in different locations are presented in Section 5.5.

5.1 Model

5.1.1 Integral-equations method

The numerical method used for the simulations in the frequency domain is the integral-equations method.

The integral-equations method can be used to solve electromagnetic radiation problems. The unknowns of these integral equations are the currents on the surfaces of the radiating or scattering objects. In this chapter, only perfect metallic objects are considered. Boundary conditions should be satisfied, so that on the perfectly conducting surfaces, the tangential component of the electric field should be zero. This electric field can be written as the sum of two components: the incident and the scattered electric field. The incident field is caused by a source on or outside the conducting body while the scattered field is caused by the surface currents. The scattered electric field is expressed as a function of the surface currents *via* integral operators. Hence, the integral equations are formed [28, 69]. By numerically solving these equations, the surface currents are determined. Furthermore, the fields can be estimated at any point of space.

Integral equations can be solved using numerical techniques such as the method of moments [28], which is the method used in Feko.

5.1.2 Wire model

To reduce the computation time, cylinder-like objects can be modeled as thin wires when the 2 following conditions are fullfilled:

- the diameter D is very small compared to the wavelength λ;
- the length L is much longer than D.

In this case, the current density on the cylinder can be assumed oriented along the wire axis [28].

Even if they fullfill the 2 previous conditions, dipole antennas are modeled as cylinders. This is because the antennas are located near the places where corona discharges appear. Thus the antennas and the elementary dipoles are in their respective near-field zone. The computation must therefore precisely account for the near-field coupling, which is very sensitive to the geometry.

5.2 Models of the antennas

5.2.1 Antenna

To estimate the received signals due to the radiation of the elementary dipoles representing corona discharges, antenna models are developed. These models are tuned to approximate the real antennas at the Champcueil station so that they can be used to correctly account for the interferences received by the real antennas. The tuned characteristics include the radiation pattern and the impedance matching.

There are 2 types of VHF antennas used at the Champcueil station: ground-plane antennas and circular arrays of dipoles with reflectors. The models are described in this section.

5.2.1.a Ground-plane antenna

The ground plane antenna is based on a quarter-wavelength monopole mounted above a finite ground plane. The plane is tilted downwards to increase the radiation towards and below the horizontal plane [28]. In practice, as indicated in Figure 1.7, the solid surface of the cone is replaced by radial wires or metallic sticks to reduce the weight and wind resistances. This kind of antenna is nearly omni-directional in the horizontal plane. Its polarization is vertical.

In Champcueil station, the ground-plane antennas are installed on top of the pylon (see Figure 1.6). These antennas are of type GPLB II A. They are produced by the Radio Frequency System company. Their characteristics are described in Appendix B.

In Apprendix B, some parameters of the antenna have been specified, including the total height and the diameters. Some other parameters, mainly the lengths of the monopole and the 4 sticks of the cone, are not specified. They are tuned to have a model with the same performance in the VHF band.

The model of this ground-plane antenna and the parameters are presented in Figure 5.1. The parameters specified in the technical files are marked in red.

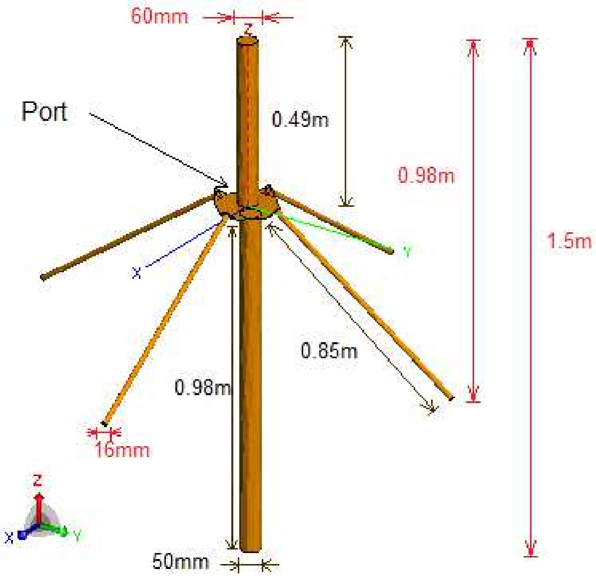

Figure 5.1: Model of the ground-plane antenna.

The Voltage Standing Wave Ratio (VSWR), that characterizes the impedance matching, is presented in Figure 5.2 for a reference impedance of 60Ω. The input impedance of the real antenna is 50Ω in Apprendix B. This slight difference is due to the feeding circuits at the antenna ports that are not included in the model.

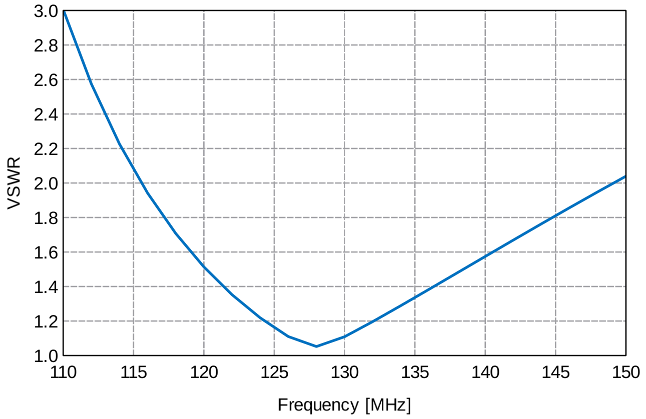

Figure 5.2: Voltage standing wave ratio (VSWR) of the ground-plane antenna in the VHF aeronautical band.

The radiation patterns are presented in Figure 5.3 and 5.4.

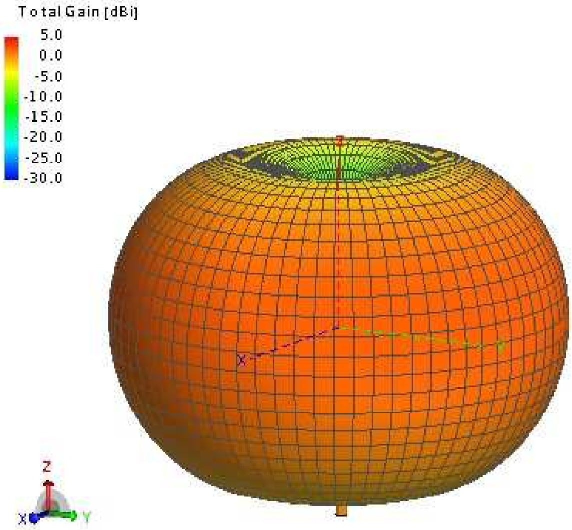

Figure 5.3: Gain pattern (dBi) of the ground-plane antenna model at 128MHz in 3D.

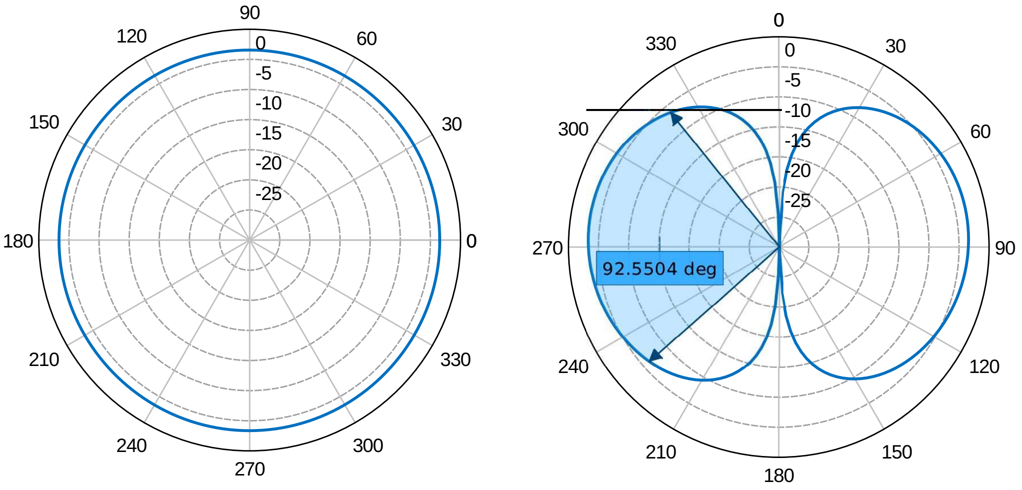

(a) (b)

Figure 5.4: Gain pattern (dBi) of the ground-plane antenna model at 128MHz: (a) horizontal plane; (b) vertical plane.

We compare the performances of the model with the real antenna. The bandwidth is defined as the band inside which the voltage standing wave ratio (VSWR) is less than 2.2 in the technical files in Apprendix B. The comparisons are presented in Table 5.1.

Characteristics	Real antenna	Antenna model
Bandwidth	115-150MHz	114-150MHz
Maximal isotropic gain	2.5 dBi	1.74 dBi
Half-power beam-width in the vertical plane	100 degrees	92.5 degrees
Radiation pattern in the horizontal plane	Omni-directional with ±0.5dB	Omni-directional with ±0.06dB

Table 5.1: Characteristics of the ground-plane antenna: model and real antennas.

The comparison shown in Table 5.1 shows that the performance of the antenna model is similar to the real antenna. The bandwidth of the model is the same as the real one. The maximal gain and the halfpower beamwidth are smaller. This may be explained by the uncertainties on the precise structure of the real antenna.

5.2.1.b Circular array of dipoles with reflectors

Each circular array of dipoles with reflectors used in Champcueil station is composed of 3 identical panels. Each panel consists of 2 dipoles and a metallic reflector (see Figure5.5). The circular arrays of dipoles of the Champcueil station are installed on the upper part of the pylon (see Figure 1.6). They are of type K523031 and they are produced by the Kathrein Company.

Some parameters of the circular array, including the distance between the reflectors and the dipoles, and the sizes of the reflectors are specified in the technical files in Appendix C. We therefore vary the non-specified parameters, including the lengths of the dipoles and the distance between the dipoles (of the same panel), to construct a model with similar performances in the VHF band.

The model of the circular array of dipoles and its parameters are presented in Figure 5.5. The parameters specified in the technical files are marked in red.

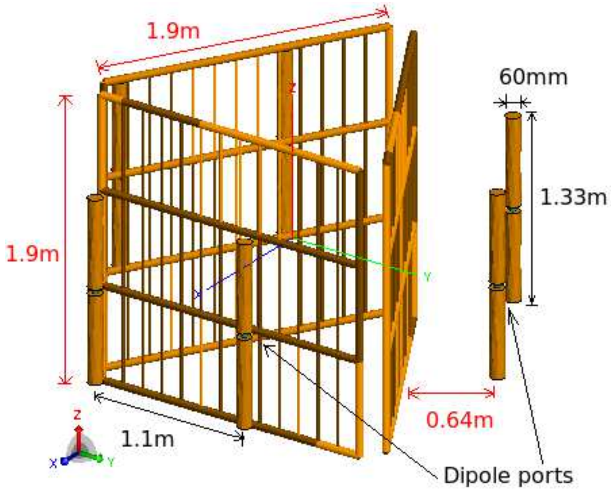

Figure 5.5: Model of the circular array of dipoles.

The total 6 dipoles are fed by power splitters (assumed ideal) so that they are fed with equi-amplitude and in phase signals. The power received by the circular array of dipoles is the power at the port of the antenna, which is the sum of the power received by the 6 dipoles.

The VSWR is presented in Figure 5.6 for a reference impedance of 140Ω. In Apprendix C, the input impedance of the circular array of dipoles is 50Ω. This may be explained by the fact that neither the power splitters nor the antenna feeding are included in the model.

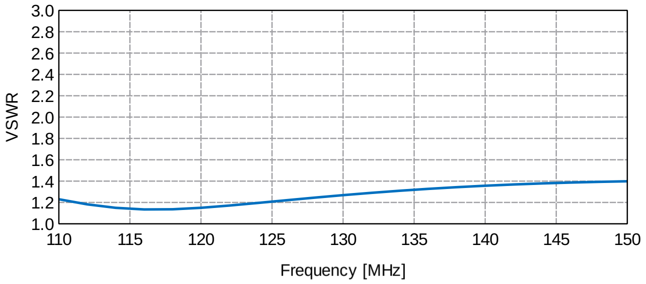

Figure 5.6: VSWR of the circular array of dipoles in the VHF aeronautical band.

The radiation patterns are presented in Figure 5.7, 5.8.

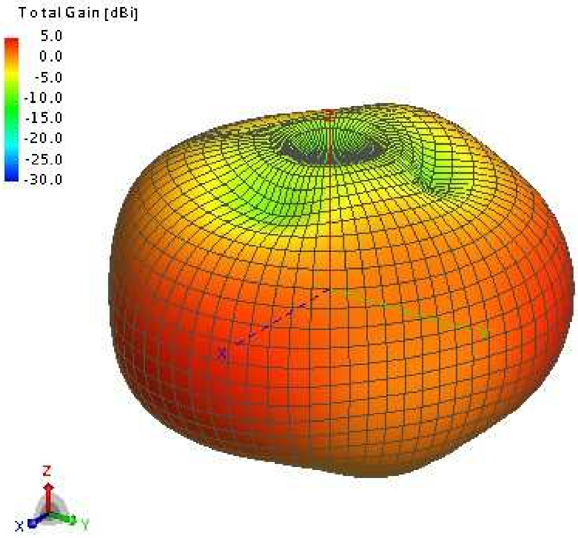

Figure 5.7: Gain pattern (dBi) of the circular array of dipoles model at 128MHz in 3D.

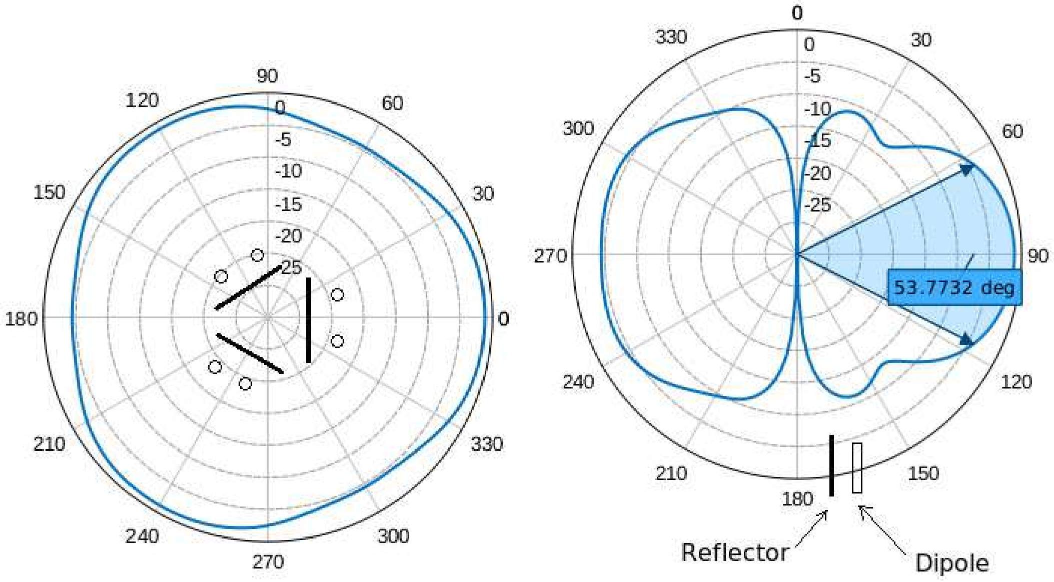

(a) (b)

Figure 5.8: Gain pattern (dBi) of the circular array of dipoles model at 128MHz: (a)horizontal plane; (b) vertical plane.

Figure 5.8 (a) shows that the radiation pattern is not completely omni-directional in the horizontal plane. There is a difference of 3.2dB between the maximal and minimal gains in the horizontal plane. The maximal gain occurs in the direction perpendicular to a panel, and the minimal gain occurs in the direction between 2 panels, which is also the direction opposite to the maximal gain. That is the reason why the radiation pattern is not symmetric in Figure 5.8 (b), which is in a plane perpendicular to a panel.

A comparison has been done between the model and the real circular array in the VHF aeronautical band. It is presented in Table 5.2. The bandwidth is defined as the band inside which the VSWR < 1.3 (as in the technical file).

The comparison presented in Table 5.2 shows that the bandwidth of the model is smaller than the real one. The maximal gain of the model is larger than the real one, at the cost of a smaller half power beamwidth in the vertical plane and a smaller bandwidth. In spite of these slight differences, the performance of the circular array model is similar to the real array.

Characteristics	Real antenna	Antenna model
Bandwidth	110-160MHz	110-134MHz
Maximal isotropic gain	3.3 dBi	3.88 dBi
Half-power beam-width in the vertical plane	64 degrees	53 degrees
Radiation pattern in the horizontal plane	Quasi omni-directional with ±1.5dB	Quasi omni-directional with ±1.6dB

Table 5.2: Characteristics of the circular array of dipoles: model and real antennas.

5.2.2 Pylon

VHF antennas are usually mounted on pylons. The effect of corona radiation interference may be influenced by the presence of the pylon. We therefore perform some simulations to include the pylon, and compare the results with the ones without the pylon.

For the Champcueil station case, the pylon is constructed with metallic tubes. The diameters of these tubes vary from 4cm to about 10cm. The lengths of these tubes are about 2 meters or more. Because the wavelength in the VHF aeronautical band is between 2m and 3m, the pylon is modeled as a wire structure.

For the ground-plane antenna, only one antenna is excited. The other antennas on the pylon are connected to matched loads

The impedance matching of the model with the pylon is compared with the one without the pylon. The results are presented in Figure 5.9 for a reference impedance of 60Ω. The comparison shows that the impedance matching of the ground-plane antenna is no affected by the presence of the pylon.

The radiation pattern of the model with the pylon is presented in Figure 5.10. The comparisons of radiation patterns in the horizontal and vertical planes are shown in Figure 5.11.

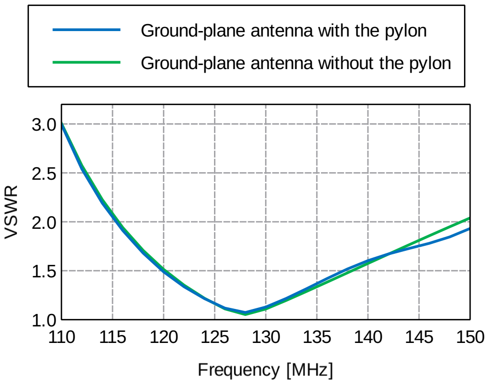

Figure 5.9: VSWR comparison between the ground-plane antenna with and without the pylon.

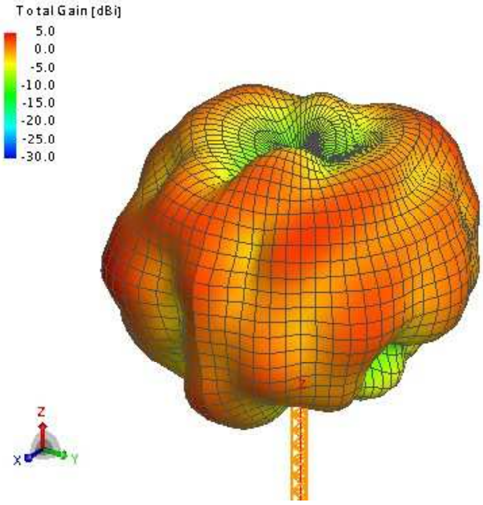

Figure 5.10: Radiation pattern of the ground-plane antenna installed on the pylon in 3D.

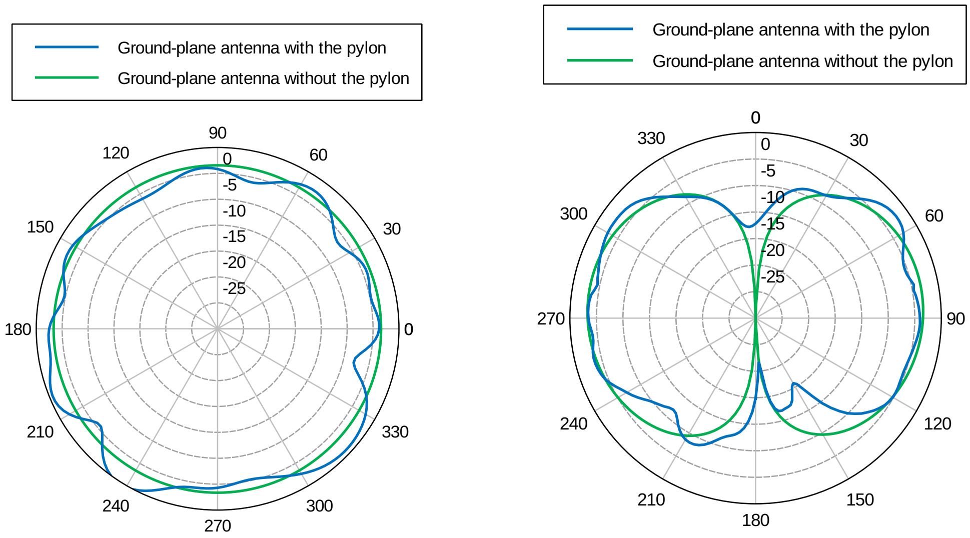

Figure 5.11: Radiation pattern comparison between the ground-plane antenna with and without the pylon: (a) horizontal plane; (b) vertical plane.

Compared with the radiation pattern without the pylon (Figure 5.3), the influence of the pylon is obvious. Because there are 3 ground-plane antennas, 3 UHF antennas and a lightning conductor on top of the pylon, the radiation in the horizontal plane is no longer omni-directional. There is a 6dB difference between the maximal and the minimal gain. The radiation in the vertical plane has also changed. In some directions below the horizon, the presence of the pylon reduces the radiation of 10dB (see Figure 5.11 (b)). However, for the directions above the horizon, which are the directions of the air-ground links, the reduction of radiation is less significant.

For the circular array of dipoles, the lower circular array is excited. The other antennas are not excited and are connected to matched loads.

The impedance matching of the model with the pylon is compared with the one without the pylon for a reference impedance of 140Ω. The results are shown in Figure 5.12. As for the ground-plane antenna, the impedance matching in the VHF band is not much influenced by the presence of the pylon.

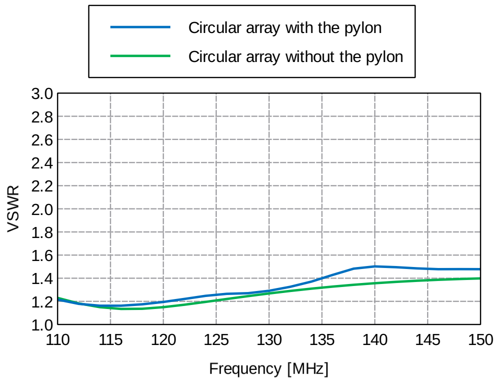

Figure 5.12: VSWR comparison between the circular array of dipoles with and without the pylon.

The radiation pattern of the circular array of dipoles with the pylon is presented in Figure 5.13. It is similar to the model without the pylon (see Figure 5.7). The comparisons of the radiation pattern in the horizontal and vertical planes are illustrated in Figure 5.14. The pylon has a small influence on the radiation pattern of the circular array of dipoles because of the presence of the reflectors.

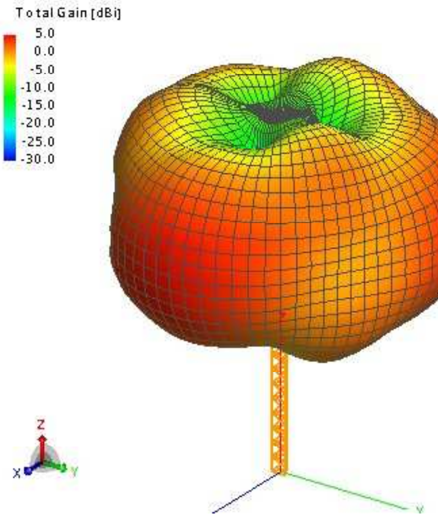

Figure 5.13: Radiation pattern of the circular array of dipoles installed on the pylon in 3D.

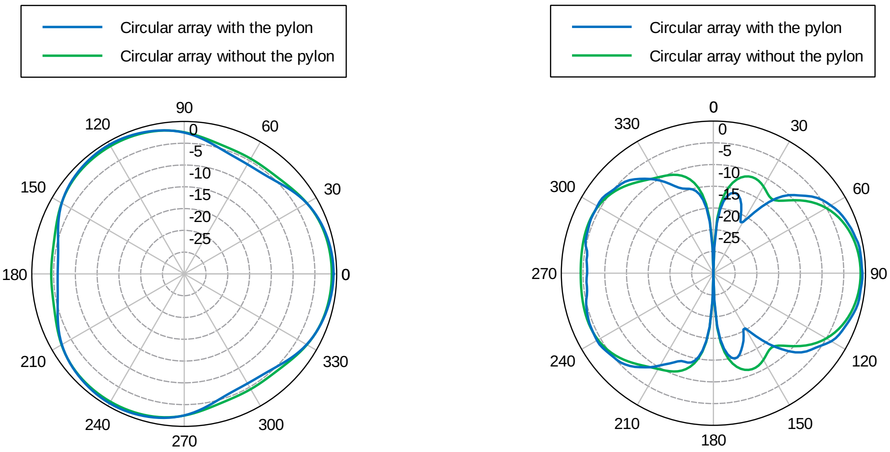

(a)

(b)

Figure 5.14: Radiation pattern comparison between the circular array of dipoles with and without the pylon: (a) horizontal plane; (b) vertical plane.

5.3 Reference noise values

In the previous section, we have presented the antenna models. We now use these models to perform the simulations in the frequency domain. In this section, we want to define a reference noise level below which the corona noise is negligible.

The total noise received at the antenna port is the sum of noises from different origins: noise of corona discharges that we study here, natural noises (cosmic radiations, sun, ground, etc.), and man-made noises (radiation of other electronic devices, radiation from high-power transmission lines, etc.). We here define a reference noise level from a noise temperature of order the ambient temperature $T_B = 290\text{K}$. On a known band, this yields a noise power P_{ref} expressed as

$$P_{\text{ref}} = k_{\text{B}} T_{\text{B}} B, \tag{5.1}$$

with $k_{\text{B}} = 1.38 \times 10^{-23} \text{J} \cdot \text{K}^{-1}$ the Boltzmann's constant, and B the bandwidth.

For a VHF voice channel B_{c}, this yields $P_{\text{ref}} = -134\text{dBm}$. As to conclude, in this Ph.D. thesis, we consider that corona noises which levels are below -134dBm on a band B_{c} are negligible because they induce a noise weaker than any noise of temperature the ambient temperature.

5.4 Simulations to estimate the interference level introduced by corona discharges at one place

5.4.1 Principle of the simulations

In this section, we perform simulations to estimate the interference levels introduced at the antenna ports by corona discharges for each location separately.

We want to evaluate the noise-per-voice-channel, *i.e.* the interference level which corresponds to the noise received on a voice channel B_{c}. For such a band, the bandwidth is very small compared to the central frequency (larger than 100MHz). Thus, the variations of the electric field and current within this band are small. Finally, on each voice channel B_c, the computation is performed at the central frequency.

To compute the interference noise on each voice channel for one discharge location, an elementary dipole of amplitude $I\delta l$ representing positive or negative corona discharges is placed at the discharge location. We have calculated in Section 4.2.3.b the average amplitude of the elementary dipole source. They are of about $0.679\mu\text{A} \cdot \text{mm}$ and $3.82\mu\text{A} \cdot \text{mm}$ for positive and negative corona discharges, respectively.

The simulations are realized *via* the commercial software Feko based on the integral equations method. In the simulation, the noise power is the power on a matched impedance connected to the antenna port. Note that the other antennas are also connected to matched loads.

In this chapter, we use the Champcueil station case as an example. The locations where corona discharges may occur have been identified in Section 3.6. They are listed here:

- top of the lightning conductor;
- tops of the monopoles and lower ends of the downward sticks of the ground-plane antennas;
- tops of the UHF antennas;
- upper and lower ends of the dipoles of the two circular array.

These discharges induce interference on 5 VHF antennas (3 ground-plane antennas, 2 circular arrays of dipoles with reflectors).

In the following sections, only the most important results are discussed. The complete simulation results are presented in Appendix E.

5.4.2 Simulation with discharges on top of the lightning conductor

The top of the lightning conductor is the place where corona discharges most certainly occur. In this section we perform simulations to evaluate whether corona discharges on top of the lightning conductor may induce a significant noise to the antennas.

The simulation results of the noise-per-voice-channel on the antennas are displayed in Figure 5.15. Because the arrangement of the ground-plane antennas are symmetrical about the axis of the pylon, the power introduced to the three ground-plane antennas are the same. As a result, we here just present the interference level on one ground-plane antenna.

For each antenna, the variation of the interference level with the frequency may be

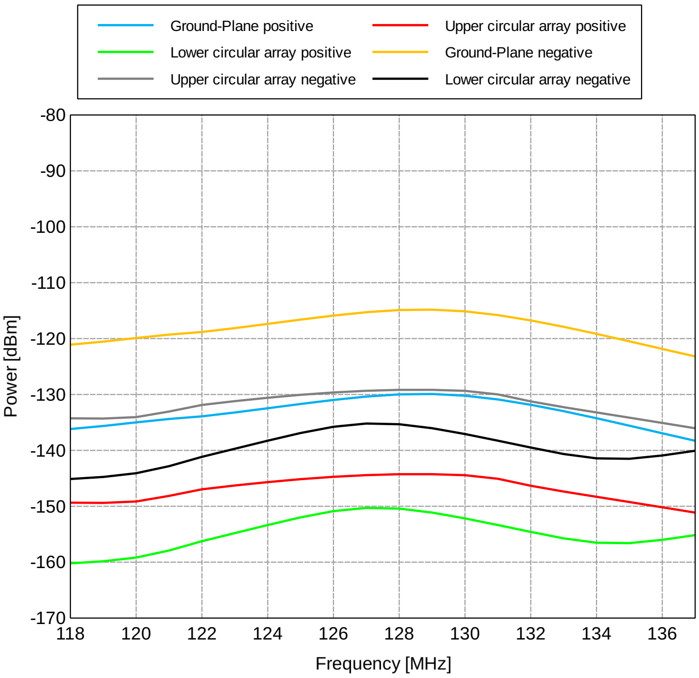

Figure 5.15: Noise-per-voice-channel introduced by positive and negative corona discharges on top of the lightning conductor.

explained by the complex near-field coupling between the corona source and the antenna.

The average values of the noise-per-voice-channel on the complete VHF aeronautical band are shown in Table 5.3.

Antennas	Average level of positive corona (dBm)	Average level of negative corona (dBm)
Ground-plane	-132.6	-117.54
Upper circular array	-146.5	-131.44
Lower circular array	-153.8	-138.74

Table 5.3: Average noise-per-voice-channel introduced at the antenna ports by corona discharges on top of the lightning conductor.

The simulation results in Figure 5.15 and Table 5.3 show that the interferences caused by positive corona discharges are always 15dB weaker than the interferences from negative corona discharges. This is due to the difference between the amplitude of the elementary dipole $I\delta l$ for positive and negative corona discharges. To simplify the presentation, from now on, we just present the results of negative corona discharges because they are stronger.

Compared with the reference noise level defined in Section 5.3, we can conclude from the simulation results that noises induced by corona discharges occurring on the lightning conductor are weak at all the antenna ports. Except for the noise at the ground-plane antennas caused by negative discharges, they are of order or weaker than the reference noise level defined in Section 5.3.

5.4.3 Simulation with discharges on different locations of a ground-plane antenna

Because of their proximity, we can expect that corona discharges occurring on a ground-plane antenna mainly cause a noise to the antenna itself. In this section, we perform simulations to verify this statement.

There are two locations on a ground-plane antenna where corona discharges may occur: the top of the monopole and the lower ends of the downward sticks. We perform simulations for the cases where corona discharges occur on top of one ground-plane antenna and on the lower end of one downward stick separately.

At first the interference caused by discharges on top of one ground-plane antenna is studied(see Figure 5.16).

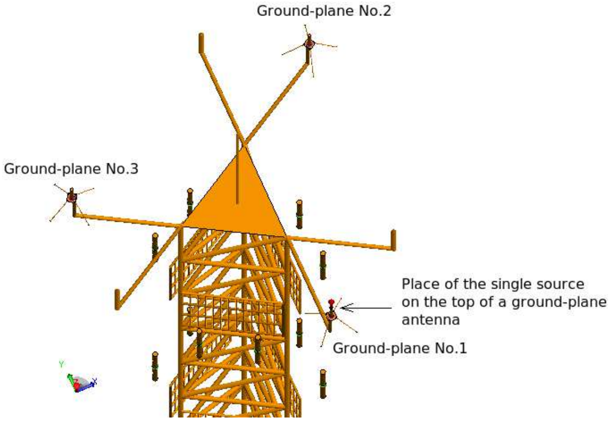

Figure 5.16: Position of the elementary dipole on top of one ground-plane antenna.

The simulation results are shown in the second column of the Table 5.4. The noises significantly above the reference noise level are marked in red. The noise levels received by the three ground-plane antennas are different because the three ground-plane antennas are not symmetrical about the corona discharge source. As expected, corona discharges on top of one ground-plane antenna (ground-plane no.1) mainly introduce a strong interference to the antenna itself. The interference levels at the two other ground-plane antennas are about 30dB weaker. The noises introduced to the circular arrays are negligible with respect to the reference noise level.

We now analyze the radiation of discharges on the lower ends of the downward sticks.

Each ground-plane antenna has four downward sticks, which are symmetrical about the axis of the monopole. We here just perform simulations for one of the downward sticks. The configuration is shown in Figure 5.17.

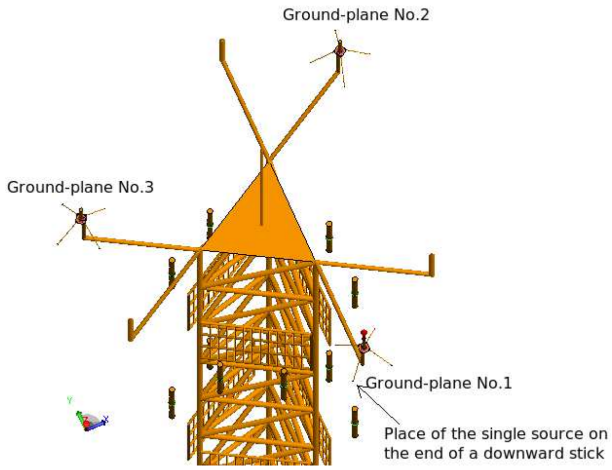

Figure 5.17: Positions of the elementary dipole at the lower end of one downward stick of one ground-plane antenna.

Antennas	Average level for top of antenna (dBm)	Average level for end of downward stick (dBm)
Ground-plane no.1 (antenna with discharges)	-94.54	-87.94
Ground-plane no.2	-123.3	-110.4
Ground-plane no.3	-124.1	-101.2
Upper circular array	-139.9	-110.4
Lower circular array	-155.3	-124.3

Table 5.4: Average noise-per-voice-channel introduced at the antenna ports by negative corona discharges on one ground-plane antenna.

From the simulation results presented in the last column of Table 5.4, we can conclude that corona discharges at the end of one downward stick of a ground-plane antenna mainly introduce a strong interference to the ground-plane antenna itself. All the other antennas receive noises but they are at least 15dB weaker.

5.4.4 Simulation with discharges on top of one UHF antenna

In Section 2.3.2.c, we have explained that the radiation of corona discharges in the UHF band is much weaker than in the VHF band. Hence corona discharges do not induce a significant noise on the UHF antennas. In this section, we perform simulations to determine whether corona discharges on top of one UHF antenna may induce a strong interference to the nearby VHF antennas. The position of the discharges is shown in Figure 5.18.

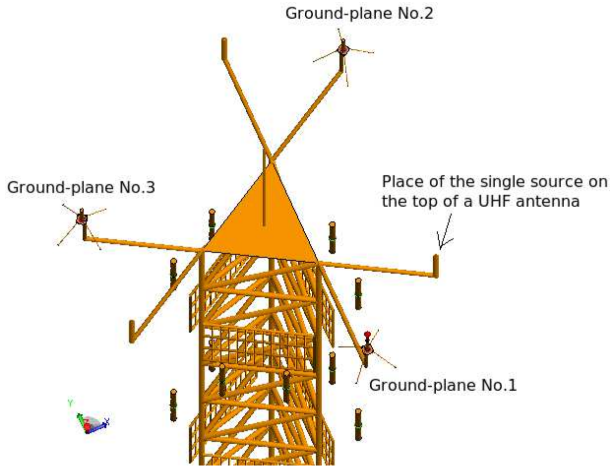

Figure 5.18: Positions of the UHF antenna where corona discharges occur.

Antennas	Average level of negative corona (dBm)
Ground-plane antennas	[-125,-115.3]
Circular arrays	[-143.5,-131.6]

Table 5.5: Average noise-per-voice-channel introduced at the antenna ports by negative corona discharges on a single UHF antenna.

With the results presented in Table 5.5, we can conclude that corona discharges on top of a UHF antenna do not introduce a strong interference to the VHF antennas. Except for the noise on the ground-plane antennas caused by negative discharges, the other noises are of order or weaker than the reference noise level.

5.4.5 Simulation with discharges on the circular arrays

As for ground-plane antennas, we can expect that corona discharges occurring on the dipole of a circular array mainly cause a noise to the circular array itself due to their proximity. In this section, we perform simulations to verify this statement.

On circular arrays of dipoles with reflectors, corona discharges may occur at both ends of the dipoles. This leads to 4 cases:

- the upper end of one dipole of the upper circular array (noted "UU");
- the lower end of one dipole of the upper circular array (noted "LU");
- the upper end of one dipole of the lower circular array (noted "UL");
- the lower end of one dipole of the upper circular array (noted "LL").

Antennas	Discharge at UU (dBm)	Discharge at LU (dBm)	Discharge at UL (dBm)	Discharge at LL (dBm)
Ground-plane antenna	[-148.2,-137.2]	[-143.9,-141.9]	[-153.8,-151.1]	[-156.2,-153.5]
Upper circular array	-113.8	-113.5	-149.9	-148.7
Lower circular array	-152.2	-150	-113.8	-113.5

Table 5.6: Average noise-per-voice-channel introduced at the antenna ports by negative corona discharges on the circular arrays.

Firstly, we find that corona discharges on one dipole of one circular array mainly cause a relatively strong interference to the circular array itself, as for the discharges on the ground-plane antennas. The interferences introduced to the other antennas are all weaker than the reference noise level.

Secondly, we can conclude from the simulation results that the interference levels introduced by corona discharges at both ends of the dipoles are the same.

5.5 Interference level introduced by several sources in different locations

In the previous section, interference levels introduced by corona discharges for each location have been presented. When the ambient electrostatic field increases, corona discharges will ignite at more places. In this section we calculate the interference level induced by corona discharges appearing simultaneously in different locations corresponding to the cases presented in Table 3.5. These cases can be listed as follows:

- case no.1: for discharges on top of the lightning conductor;
- case no.2: for case no.1 plus discharges on the ground-plane antennas and the UHF antennas;
- case no.3: for case no.2 plus discharges on the two circular arrays of dipoles with reflectors.

Corona discharges occurring simultaneously in different places are not correlated. Thus, for one antenna, the interference level received from N corona discharge sources P_{total} can be calculated as

$$P_{\text{total}} = \sum_{i=1}^{N} P_i, \tag{5.2}$$

where P_i is the power introduced by the ith source while no other source is radiating.

With (5.2), the total noise-per-voice-channel introduced by corona discharges at different locations can be evaluated. These results are presented in Table 5.7 and 5.8 for positive and negative corona discharges, respectively.

For case no.1, discharges induce noises of order or weaker than the reference noise level. We can conclude that positive corona discharges can not generate a notable noise to any antenna, and negative corona discharges may only generate a weak noise to the ground-plane antennas.

No. of the group	Noise received by ground-plane antenna (dBm)	Noise received by upper circular array (dBm)	Noise received by lower circular array (dBm)
1	-132.6	-146.5	-153.8
2	-97.3	-114.7	-128.6
3	-97.3	-113	-118.2

Table 5.7: Average noise-per-voice-channel introduced at the antenna ports by simultaneous positive corona discharges in different places.

No. of the group	Noise received by ground-plane antenna (dBm)	Noise received by upper circular array (dBm)	Noise received by lower circular array (dBm)
1	-117.5	-131.4	-138.7
2	-81.2	-99.6	-113.5
3	-81.2	-97.9	-103.1

Table 5.8: Average noise-per-voice-channel introduced at the antenna ports by simultaneous negative corona discharges in different places.

For case no.2, all the antennas can receive noises stronger than the reference noise level. Corona discharges on the ground-plane antennas induce strong noises to the antennas themselves. They also generate noises on the circular arrays, particularly on the upper one.

We have shown that for each antenna, the main sources of interference are corona discharges on the antennas themselves. Hence for case no.3, the noise levels of the circular arrays of dipoles are increased, particularly for the lower circular array. For the upper circular array, besides discharges on itself, it is also influenced by discharges on the ground-plane antenna which already exist in case no.2.

5.6 Comparison between the simulation results and the measurements

In this section we compare the simulation results with the measurements.

5.6.1 Calibration of the measurements

In the simulations, the noise-per-voice-channel has been computed at the antenna ports. In the measurements, the noises are observed at the output of a receiver. To compare both results, the receiver noise must be taken into account. Indeed, the measurements correspond to the combination of the corona and receiver noises. To get free of the receiver noise, we perform a calibration with a known noise source as indicated in Figure 5.19.

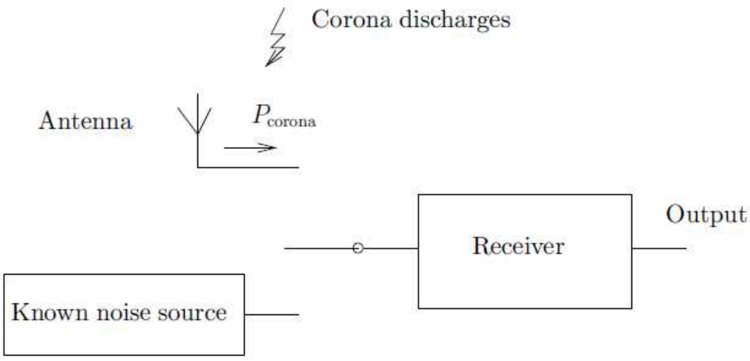

Figure 5.19: Schema of calibrations for the influence of the receiver.

Taking into account the calibration, for a voice channel B_{c}, the corona noise measured at the antenna ports P_{corona} can be expressed as [70]

$$P_{\text{corona}} = k_B T_{\text{corona}} B_c, \tag{5.3}$$

with

$$T_{\text{corona}} = \frac{(\text{ENR}+1)T_0 + T_{\text{E}}(1-Y)}{Y}, \tag{5.4}$$

and

- ENR the excess noise ratio of the known noise source;
- T_0 the ambient temperature;
- T_E the equivalent noise temperature of the receiver, $T_E = (F-1)T_0$;
- F the noise factor of the receiver;
- $Y = P_\mathrm{source}^\mathrm{measure} / P_\mathrm{corona}^\mathrm{measure}$;
- $P_\mathrm{source}^\mathrm{measure}$ the power of the noise source measured by the receiver;
- $P_\mathrm{corona}^\mathrm{measure}$ the corona noise measured by the receiver.

At the Champcueil station, the measurements have been realized with a Rohde & Schwartz receiver of type EB200. Its noise factor is about 9dB. The ambient temperature T_0 is about 290K. Besides, a noise source of ENR = 15.34dB has been used for the calibration.

We find that during the measurements at the Champcueil station, the maximal noise level for positive and negative corona discharges occurred at 5:38 on August 2, 2007, and at 4:20 on August 2, 2007, respectively. They have been presented in Figure 1.9. Using (5.3) and (5.4), we can estimate the noise levels at the antenna ports from the measured noises. They are given in Table 5.9.

Antennas	Maximal noise of positive discharges (dBm)	Maximal noise of negative discharges (dBm)
Ground-plane antenna	-96	-103
Upper circular array of dipoles	-111	-112
Lower circular array of dipoles	-120	-113

Table 5.9: Maximal noise levels at the antenna ports of Champcueil ground station on August 2, 2007.

Note that in the measurements at the Champcueil station, the receiver has a small influence, *i.e.* the differences between the corona noise at the antenna port and at the receiver output is smaller than 2dB.

5.6.2 Comparison with the measurements

For positive corona discharges, from Table 5.7 and 5.9, we conclude that the measurements are in good agreement with the simulations: considering the electrostatic simulations, the noise levels should correspond to the simulations of case no.2. The noise level difference between the ground-plane antenna and the upper circular array is about 15dB. This is almost the same as in the simulation. Other measurement results are presented in Appendix A. They show that this 15dB difference always exists with positive corona noises.

For negative corona discharges, the measured noise levels are weaker than the simulated noises. This may be explained by the uncertainties on the pulse amplitudes and repetition rates (see Table 2.3). They may largely differ from the values we have chosen for the simulations.

5.7 Conclusion

The models of the VHF antennas have been developed. The simulations in the frequency domain have been performed to evaluate the noise levels induced by corona discharges for each possible location. The noise levels induced by simultaneous corona discharges in different places have been estimated. The simulation results have been compared with the measurements. For negative corona discharges, the measured noise levels are weaker than the simulated noise. For positive corona discharges, they are in good agreement.

Conclusion

Summary of the study

The main objective of this Ph.D. thesis was to develop a model to predict quantitatively the interference level induced by corona discharges at VHF antennas for a known pylon geometry and ambient electrostatic field.

In order to achieve this objective, we have defined several subgoals. The first one was to prove that corona discharges are the origin of the interferences observed at the ground stations. The second one was to localize where corona discharges most likely occur on the pylon. The third one was to study the characteristics of corona discharges and to find a model that can represent their radiation in the VHF band. The last one was to evaluate the interference level introduced by corona discharges at the antennas, and compare the results with the measurements that have been performed at the Champcueil ground station.

In **Chapter 1**, we have studied the origin of the interference phenomena. We have considered the Champcueil station as an example. At first, we have presented the aeronautical telecommunication system impaired by the interference. We have then described the observed interference, listed, and analyzed its possible origins. We have found that the most probable reason for this noise is electrostatic discharges caused by the natural ambient electrostatic field. To confirm the analysis, simultaneous on-site measurements of the ambient electrostatic field and the VHF interference level have been presented. We have found that there exists a strong correlation between the ambient electrostatic field and the VHF interference level. Hence, we have concluded that electrostatic discharges caused by the natural ambient electrostatic field are most likely the origin of the interference observed at the ground stations.

In **Chapter 2**, we have studied the mechanism and the characteristics of corona discharges. Two different types of corona discharges have been presented, namely the positive and negative discharges. They generate a series of pulses occurring at the locations where there are strong non-uniform electrostatic fields. We have seen that the physics of positive and negative discharges are not the same. For both types of corona discharges, we have listed the essential characteristics, such as the pulse form, the pulse amplitude, and the repetition rate.

In **Chapter 3**, we have localized where corona discharges most likely occur on the pylon. At first, we have presented the equations and the numerical method (Finite Element Method) for the electrostatic simulations. Secondly, we have made simplifications to render the problem amenable by the numerical method. Then, the model has been validated on Champcueil station. Thirdly, in order to avoid the singularity caused by edges in the model, we have developed a criterion for the ignition of corona discharges which consists in comparing the computed electrostatic field with a critical field at a fixed given distance from the edges. At last, we have performed the electrostatic simulations to estimate the electrostatic field around the pylon to localize corona discharges. We have found the locations where corona discharges most likely occur. We have defined groups of locations for which the discharges occur from the same value of ambient field. These groups are directly related to the heights of the possible discharge locations.

In **Chapter 4**, we have developed a model to represent the radiation of corona discharges for the simulations in the frequency domain. Firstly, we have proposed an elementary dipole model. We have verified that it can represent the radiation of corona discharges in the VHF band. Then, we have determined the amplitude of the elementary dipole according to the characteristics of corona discharges in the VHF band by means of a deterministic and a statistical approaches.

In **Chapter 5**, we have performed the simulations in the frequency domain to evaluate the interference level introduced by corona discharges at the antennas. Firstly, we have developed models of the antennas with realistic performances. Secondly, we have estimated the noise introduced by corona discharges in each location by means of simulations in the frequency domain with elementary dipoles placed at each location. We have found that, for each VHF antenna, the noise received is mainly caused by corona discharges occurring on the antenna itself. At last, we have computed the noise levels introduced by corona discharges occurring simultaneously in different locations, and we have compared the simulation results with the measurement results collected at the Champcueil station. For negative corona discharges, the measured noise levels are weaker than the simulated noises. However, they are in good agreement for positive discharges.

Recommendations for the reduction of corona noise

During the process employed to achieve the main objective of this Ph.D. thesis, we have derived some conclusions that may be helpful to reduce the noise level caused by corona discharges.

We have found that for each antenna, the noise received is mainly caused by corona discharges occurring on the antenna itself. Hence, a practical way to reduce the noise level is to avoid corona discharges occurring on the antenna by means of reducing the electrostatic field level at the antennas. To achieve this, several possible methods can be imagined.

The first one is to increase the length of the lightning conductor. Indeed, a longer lightning conductor can provide better shielding for the antennas, so that the electrostatic fields on the antennas would be weakened and the possibility of discharge would be reduced.

The second one is to avoid installing the antennas on top of the pylon. The simulations have shown that in spite of the presence of a lightning conductor, the electrostatic field on top of the pylon can still be relatively strong. If the antennas are installed several meters below the top, the electrostatic field would be much weaker, so that the possibility of discharge would be reduced.

The third one is to add extra shielding rods to the antennas. These shielding rods may function as small "lightning conductors" and provide shielding to the nearby antennas so that the electrostatic field is reduced. Souny [71] has proposed such a method to reduce the noise level at the circular array of dipoles at the Champcueil station. It should be noticed that the extra shielding rods may influence the radiation pattern of the antennas. Thus they must be designed taking into account VHF aspects.

The fourth one is to design suitable antennas. Indeed, corona discharges usually occur at the sharp edges of the cylindrical dipole ends. Hence if the VHF antenna has less edges or sharp ends, the possibility of discharge would be reduced.

Future works

In the short term, firstly, we could study more cases of interferences observed at ground stations. In this thesis, we have considered the Champcueil station as an example for the analysis. The interference phenomena have also been observed at other ground stations. We may study these cases to verify and refine the model.

Secondly, we could perform some measurements to determine more precise values for the amplitude of the elementary dipole representing corona discharges in the VHF band. These values should depend on the configuration and the ambient electrostatic field. In this thesis, we have estimated these values by means of approaches based on the characteristics found in the literature. For negative discharges, the uncertainty on the discharges amplitude is large enough to obtain significant differences between the simulation and the measurements. Direct measurements of the VHF radiation of corona discharges may provide more accurate results. Some measurements have been performed in the literature [25, 54], but they present limitations. Firstly, the measurements are influenced by the environment. A possible solution would be to perform the measurements in an anechoic chamber. Secondly, a standard corona discharger may not radiate efficiently signals in the VHF band. Hence, the discharger should be coupled with a resonant element in the VHF band. A possible method would be to directly generate corona discharges on a real VHF antenna. During this Ph.D. thesis, first attempts have been made but the design of a corona discharger with good VHF radiation capabilities was out of the scope of this work.

Thirdly, we may try to study the noise introduced by corona discharges in other frequency bands. The principles would be the same as the ones presented in this thesis.

In the long term, we may consider to apply this method to other domains where corona discharges generate interferences. For example, for the domain of in-flight aircrafts, we may use our method to predict the corona interference level, or to optimize the wick dischargers.

Appendix A

Measurement results at the Champceuil station

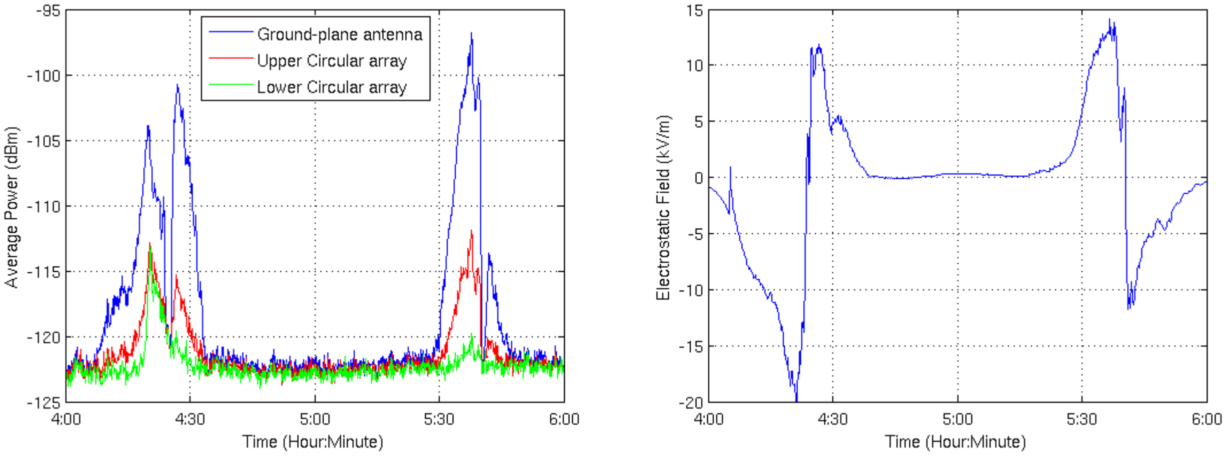

(a) (b)

Figure A.1: Measurement results on August 2 2007 : (a)average noise-per-voice-channel; (b)electrostatic field measured.

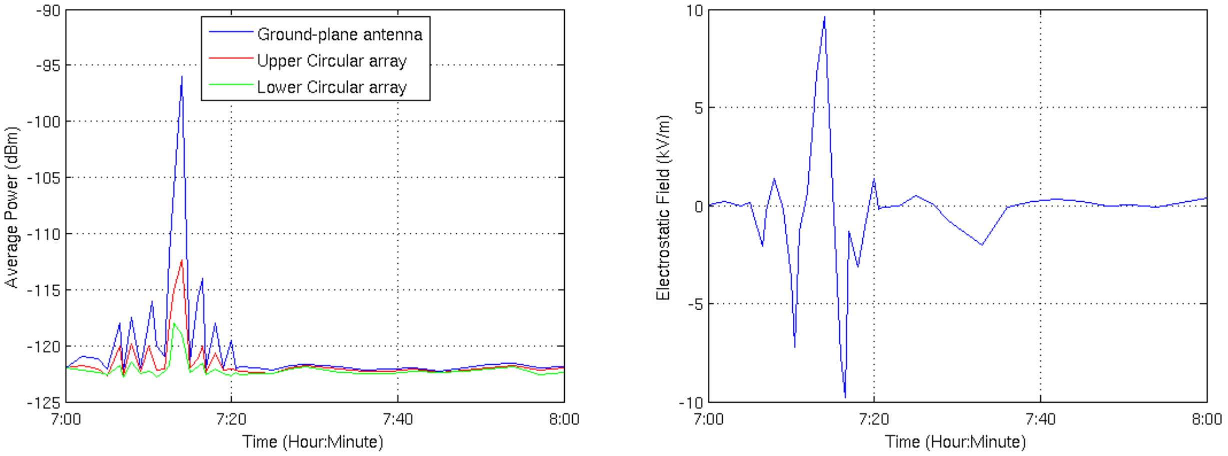

(a) (b)

Figure A.2: Measurement results on August 6 2007 : (a)average noise-per-voice-channel; (b)electrostatic field measured.

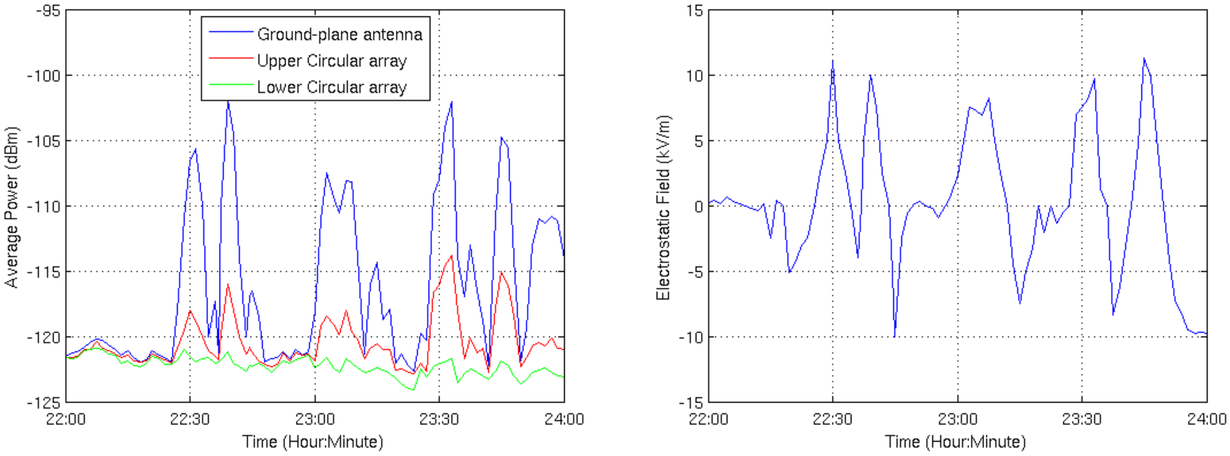

(a) (b)

Figure A.3: Measurement results on August 7 2007 : (a)average noise-per-voice-channel; (b)electrostatic field measured.

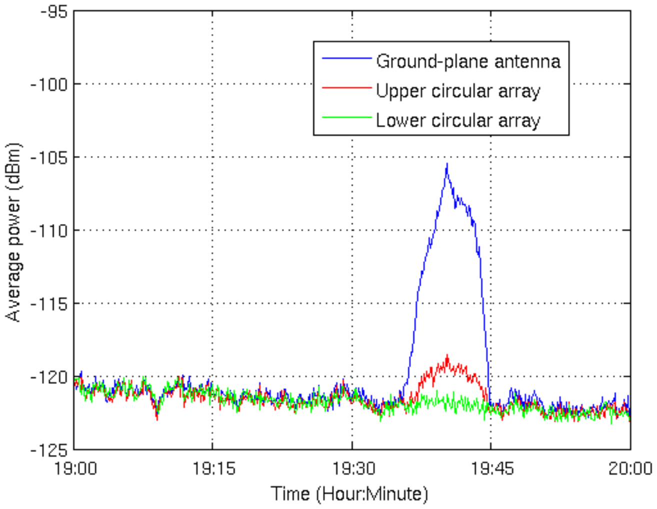

Figure A.4: Average noise-per-voice-channel on July 21 2007.

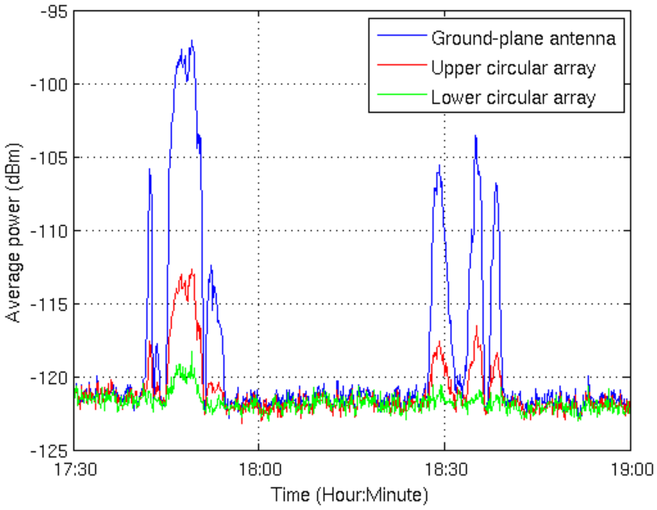

Figure A.5: Average noise-per-voice-channel on July 23 2007.

Appendix B

Technical files of the ground-plane antennas

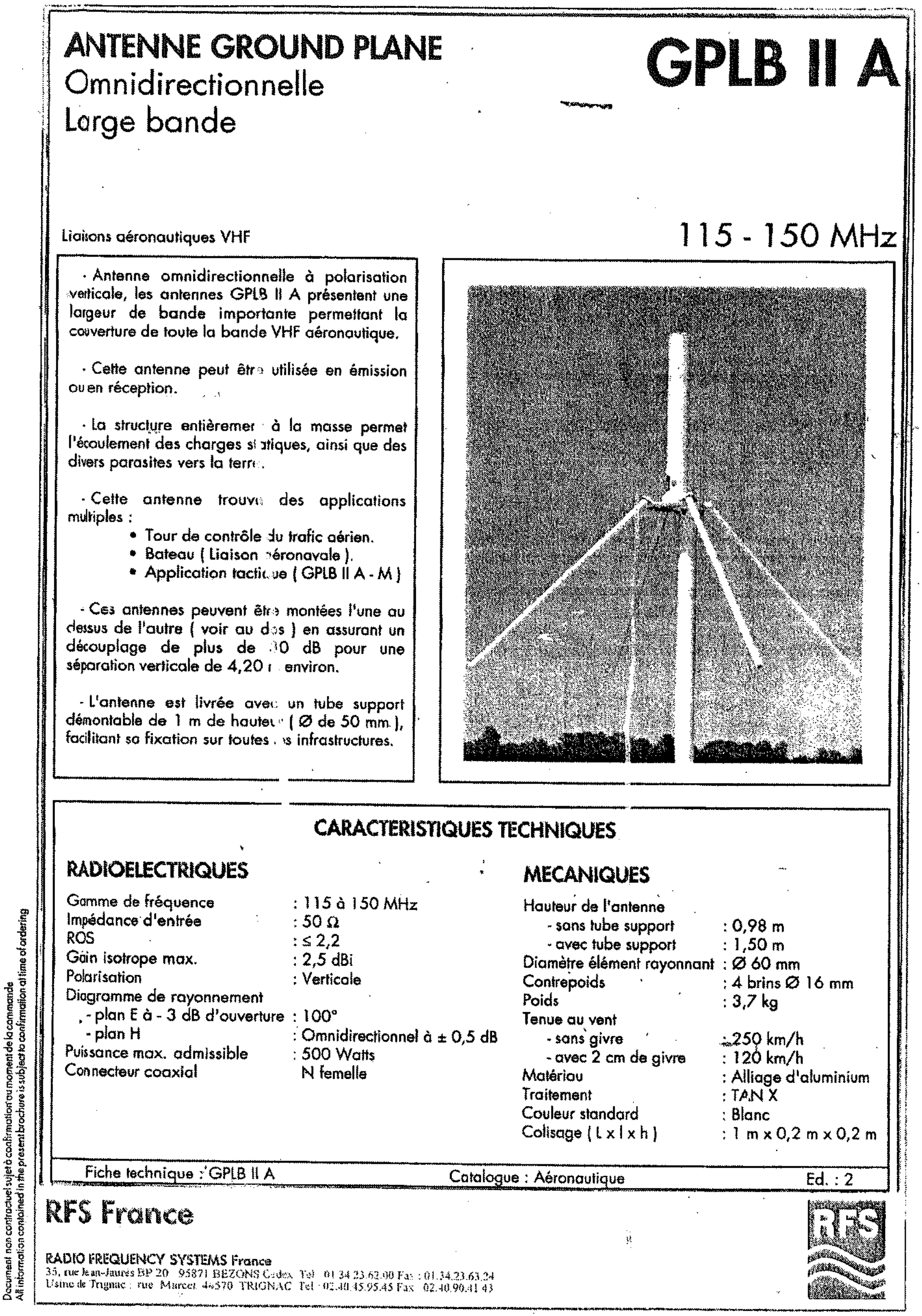

ANTENNE GROUND PLANE
Omnidirectionnelle
Large bande

GPLB II A

Liaisons aéronautiques VHF

115 - 150 MHz

- Antenne omnidirectionnelle à polarisation verticale, les antennes GPLB II A présentent une largeur de bande importante permettant la couverture de toute la bande VHF aéronautique.

- Cette antenne peut être utilisée en émission ou en réception.

- La structure entièrement à la masse permet l'écoulement des charges statiques, ainsi que des divers parasites vers la terre.

- Cette antenne trouve des applications multiples :
  - Tour de contrôle du trafic aérien.
  - Bateau (Liaison aéronavale).
  - Application tactique (GPLB II A - M)

- Ces antennes peuvent être montées l'une au dessus de l'autre (voir au dos) en assurant un découplage de plus de [illegible]0 dB pour une séparation verticale de 4,20 m environ.

- L'antenne est livrée avec un tube support démontable de 1 m de hauteur (Ø de 50 mm), facilitant sa fixation sur toutes les infrastructures.

CARACTERISTIQUES TECHNIQUES

RADIOELECTRIQUES

Gamme de fréquence : 115 à 150 MHz
Impédance d'entrée : 50 Ω
ROS : ≤ 2,2
Gain isotrope max. : 2,5 dBi
Polarisation : Verticale
Diagramme de rayonnement
- plan E à - 3 dB d'ouverture : 100°
- plan H : Omnidirectionnel à ± 0,5 dB
Puissance max. admissible : 500 Watts
Connecteur coaxial N femelle

MECANIQUES

Hauteur de l'antenne
- sans tube support : 0,98 m
- avec tube support : 1,50 m
Diamètre élément rayonnant : Ø 60 mm
Contrepoids : 4 brins Ø 16 mm
Poids : 3,7 kg
Tenue au vent
- sans givre : 250 km/h
- avec 2 cm de givre : 120 km/h
Matériau : Alliage d'aluminium
Traitement : TAN X
Couleur standard : Blanc
Colisage (L x l x h) : 1 m x 0,2 m x 0,2 m

Fiche technique : GPLB II A
Catalogue : Aéronautique
Ed. : 2

RFS France

RADIO FREQUENCY SYSTEMS France
35, rue Jean-Jaurès BP 20 95871 BEZONS Cedex Tel 01.34.23.62.00 Fax : 01.34.23.63.24
Usine de Trignac : rue Marcel 44570 TRIGNAC Tel 02.40.45.95.45 Fax 02.40.90.41.43

Appendix C

Technical files of the circular dipole arrays with reflectors

Directional Antenna
100 – 160 MHz
K 52 30 31

KATHREIN
Antennen · Electronic

K 52 30 37 connectique 7/16

A heavy duty 8 dB gain panel of hot dip galvanized steel for use under heavy icing

Type No.	K 52 30 31
Input	N female connector in a weather protective housing directly at the antenna
Frequency range	100 – 160 MHz
VSWR	< 1.3
Gain (ref. λ/2 dipole)	8 dB
Impedance	50 Ω
Polarization	Horizontal or vertical
Max. Power	1590 Watt (at 50 °C ambient temperature)
Weight	35 kg
Windload	1200 N (at 160 km/h)
Max. wind velocity	200 km/h (incl. $^1/_2$″ radial ice)
Packing size	2000 x 2000 x 850 mm
Height/width/depth	1900 x 1900 x 640 mm

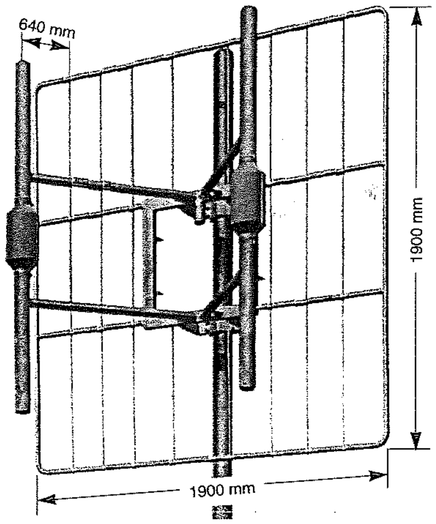

Material:	Hot dip galvanized steel. All screws and nuts: Stainless steel.
Montage:	By means of a pair of hot dip gavanized steel clamps K 61 12 0 to pipes of 60 – 115 mm OD or the pair of clamps K 61 13 0 to pipes of 115 – 200 mm.
Grounding:	All metal parts of the antenna including the mounting kit are DC grounded.
Scope of supply:	Panel without mounting hardware.
Special features:	The fiberglass cover of the radiators keeps the electrical characteristics, even under heavy icing conditions, nearly constant.

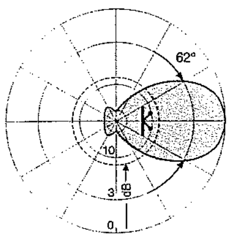

Horizontal Pattern

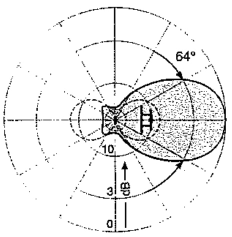

Vertical Pattern

3.3 Conclusions

3.3.1 Solution retenue

La solution retenue consiste à associer 3 panneaux K523037 à 120° les uns des autres et à une distance de 650 mm de leur centre de phase (centre du pylône). La distance de 650 mm permet d'utiliser un pylône triangulaire de 2200 m de côté.
Le diagramme de rayonnement de la couronne ainsi formée sera le suivant :

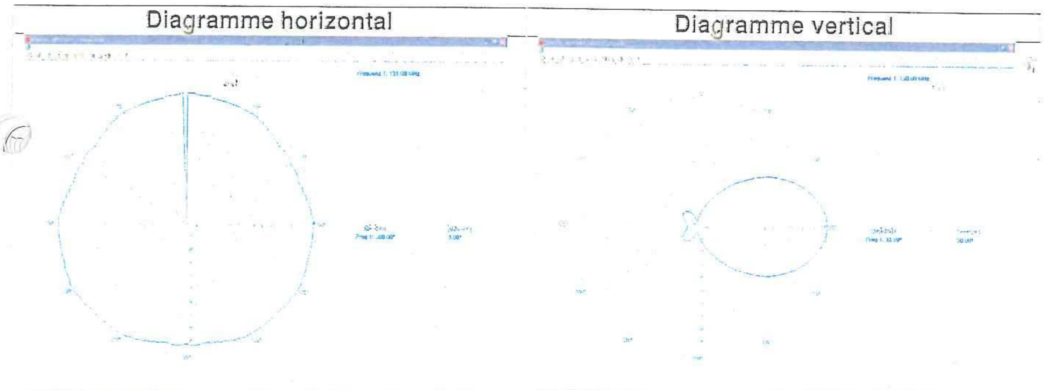

Gain maximum calculé = 3,3 dBi
Omnidirectivité < 1 dB (+/-0,5 dB)

A cette valeur de gain, il faut toutefois retrancher la perte d'insertion des bretelles coaxiales reliant les panneaux au splitter et le splitter au feeder, ainsi que les pertes d'insertion du splitter. L'ensemble de ces pertes est cependant inférieur à 1 dB.

3.3.2 Principe d'alimentation des couronnes

Les trois panneaux VHF sont alimentés chacun par 3 bretelles de longueur identique, pour s'affranchir de tout déphasage. Ces 3 bretelles sont reliées à un diviseur de puissance K62563 lui-même relié par une bretelle coaxiale au feeder.
La fiche technique du diviseur de puissance K62563 est présentée en annexe. L'intérêt de ce type d'équipement est de présenter des pertes d'insertion très faibles (< 0,05 dB).

Les bretelles sont constituées ainsi :

- Câble ½" super flexible
- Longueur 3 m pour relier le splitter aux panneaux, 1 m pour relier le splitter au feeder
- Connectique 7-16 mâle
- Etanchéité longitudinale : IP68
- Pertes d'insertion : 11,2 dB / 100 m à 900 MHz
- ROS : 1,08 à 900 MHz

L'utilisation du câble ½" SUPERFLEX permet de minimiser les pertes tout en conservant une bonne souplesse. Ce type de câble est préférable au choix du RG214.

Appendix D

Relation between the ambient field and the measured field

At the Champcueil station, the electrostatic field is measured with a field mill (assumed ideal). Because the distance between the field mill and the pylon is less than 20m (see Figure 1.11), the field measured with the field mill E_{measured} may be different from the ambient electrostatic field. In this appendix, we determine the ambient electrostatic field from the measured field.

The simulation model is the Champcueil station with the ground-station building, as presented in Section 3.4.3.c. The parameters of the building are presented in Figure D.1. The field mill is placed at an altitude of 2m above the chimney of the building (see Figure 1.11 (b) and (c)).

The simulation results for the electrostatic field E are presented in Figure D.2 (b) along a vertical segment above the chimney (shown in Figure D.2 (a)). Note that we here present the electrostatic field normalized with respect to the ambient field.

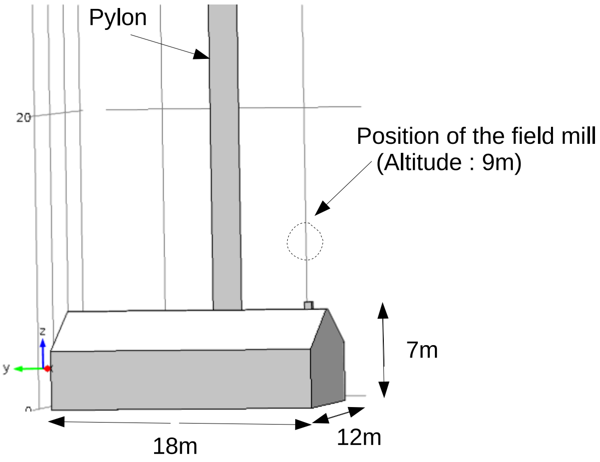

Figure D.1: Size of the ground station building and position of the field mill.

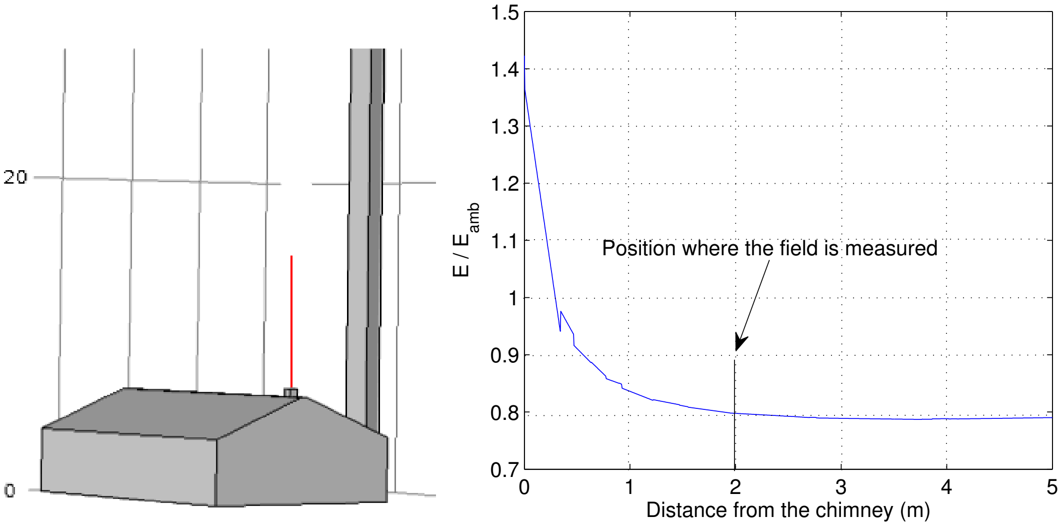

(a) (b)

Figure D.2: Comparison the ambient field with the computed field: (a) place where the electric field is computed (red line); (b) normalized electric field along the red line.

The simulation results in Figure D.2 show that in the area where the field mill is placed, the electrostatic field is about 0.8 times of the ambient field. That means that the electric field measured by the field mill is reduced by the presence of the pylon. Hence, in the case of the Champcueil ground station, the value of the ambient field E_{amb} can be approximately calculated by

$$E_{\mathrm{amb}} = \frac{E_{\mathrm{measured}}}{0.8}. \tag{D.1}$$

Appendix E

Simulation results of the interference level induced by corona discharges for each location

Antennas	Average level of positive corona (dBm)	Average level of negative corona (dBm)
Ground-plane No.1	-132.6	-117.54
Ground-plane No.2	-132.6	-117.54
Ground-plane No.3	-132.6	-117.54
Upper circular array	-146.5	-131.44
Lower circular array	-153.8	-138.74

Table E.1: Average noise-per-voice-channel in the VHF band introduced by average-level corona discharges on the top of the lightning conductor.

Antennas	Average level of positive corona (dBm)	Average level of negative corona (dBm)
Ground-plane No.1 (antenna with discharges)	-109.63	-94.54
Ground-plane No.2	-138.4	-123.3
Ground-plane No.3	-139.2	-124.1
Upper circular array	-155	-139.9
Lower circular array	-170.4	-155.3

Table E.2: Average noise-per-voice-channel in the VHF band introduced by average-level corona discharges on the top of a ground-plane antenna.

Antennas	Average level of positive corona (dBm)	Average level of negative corona (dBm)
Ground-plane No.1 (antenna with discharges)	-103.03	-87.94
Ground-plane No.2	-125.5	-110.4
Ground-plane No.3	-116.3	-101.2
Upper circular array	-125.5	-110.4
Lower circular array	-139.4	-124.3

Table E.3: Average noise-per-voice-channel in the VHF band introduced by average-level corona discharges at the lower end of a downward stick of a ground-plane antenna.

Antennas	Average level of positive corona (dBm)	Average level of negative corona (dBm)
Ground-plane No.1	-130.4	-115.3
Ground-plane No.2	-131.9	-116.8
Ground-plane No.3	-140.1	-125
Upper circular array	-146.7	-131.6
Lower circular array	-158.6	-143.5

Table E.4: Average noise-per-voice-channel in the VHF band introduced by average-level corona discharges on a single UHF antenna.

Antennas	Discharge at UU (dBm)	Discharge at LU (dBm)	Discharge at UL (dBm)	Discharge at LL (dBm)
Ground-plane No.1	-152.3	-157	-166.2	-171.3
Ground-plane No.2	-156.5	-161.3	-166.9	-169.9
Ground-plane No.3	-163.3	-159	-168.9	-168.9
Upper circular array	-128.9	-138.6	-165	-163.8
Lower circular array	-167.3	-165.1	-128.9	-128.6

Table E.5: Average noise-per-voice-channel in the VHF band introduced by average-level positive corona discharges on the circular arrays.

Antennas	Discharge at UU (dBm)	Discharge at LU (dBm)	Discharge at UL (dBm)	Discharge at LL (dBm)
Ground-plane No.1	-137.2	-141.9	-151.1	-156.2
Ground-plane No.2	-141.4	-146.2	-151.8	-154.8
Ground-plane No.3	-148.2	-143.9	-153.8	-153.8
Upper circular array	-113.8	-113.5	-149.9	-148.7
Lower circular array	-152.2	-150	-113.8	-113.5

Table E.6: Average noise-per-voice-channel in the VHF band introduced by average-level negative corona discharges on the circular arrays.

Résumé

Introduction

1. Contexte

En aviation civile, les communications entre les pilotes d'avions et les contrôleurs aériens sont d'une importance primordiale pour garantir la sécurité des vols. Des voix et données numériques sont transmises par des systèmes de communication radio, principalement dans la bande VHF [1]. Des stations sol équipées d'antennes VHF sont utilisées pour recevoir les signaux radio des pilotes et les transmettre aux contrôleurs aériennes, et *vice versa.*

En radiocommunications, les signaux transmis sont modulés et ensuite émis par l'antenne d'émission. Ils se propagent dans l'espace, sont ensuite captés par l'antenne de réception, puis finalement démodulés. Le bilan de liaison et l'horizon radio limitent la portée des communications aéronautiques VHF à quelque centaines de kilomètres [2]. De plus, il existe de nombreux phénomènes physiques qui peuvent modifier les signaux radios lors de leur propagation dans l'espace. Les signaux VHF des télécommunications aéronautiques peuvent notamment être perturbés par le rayonnement d'appareils électroniques ou par des sources naturelles de bruit.

Plus particulièrement, un phénomène de brouillage a été observé sur les stations de réception utilisées pour les liaisons air-sol par la Direction Générale de l'Aviation Civile (DGAC). Ces bruits parasites, qui perturbent les dialogues entre les pilotes et les contrôleurs aériens, ont été rencontrés de nombreuse fois, notamment sur la station située à Champceuil proche de Paris. Par conséquent, identifier l'origine de ces interférences et étudier leurs propriétés sont essentiels.

Des mesures ont été réalisées pour déterminer l'origine des interférences. Elles ont montré que l'origine est probablement des décharges électrostatiques, plus particulièrement des décharges corona provoquées par un champ électrostatique local fort. Ce champ électrostatique peut être expliqué par les conditions météo [3, 4].

Les décharges corona sont un type de décharges électrostatiques qui se produisent aux endroits où le champ électrostatique est fort et nonuniforme [5, 6]. Les endroits où ces décharges se produisent comprennent les arêtes, les extrémités pointues et les fils de petit diamètre [5, 7]. Un exemple de décharges corona est le feu de Saint-Elme apparaissant au dessus des mâts des bateaux pendant l'orage.

Les brouillages provoquées par les décharges corona ont été observés dans plusieurs domaines, tel que les lignes de transmission à haute tension [8], les avions en vols [9], les pylônes au sol pour la diffusion de la télévision [10]. Moins de littératures existe sur les brouillages corona par rapport aux autres types de décharges, notamment les décharges électrostatiques (ESD) et la foudre. Dans les paragraphes suivantes, les phénomènes existants sont listés et la façon dont ils interfèrent avec les communications VHF est expliquée.

Les décharges corona se produisent souvent sur les lignes de transmission à haute tension en raison du faible rayon des lignes et de leur fort potentiel. Ce phénomène a été étudié par de nombreux auteurs parce qu'il cause des pertes de puissance [8, 11, 12, 13, 14, 15]. Les corona décharges génèrent également un brouillage sur une large bande (de continu à la VHF) [8, 13, 16, 17].

Les décharges corona ont également été étudiés largement pour les systèmes de radio à bord des avions à grande vitesse [7, 9]. Dans les années 1940, des brouillages sur les signaux des systèmes de radiocommunication et de navigation ont été observés. Des mesures ont été effectuées. Elles ont montré que, pendant le vol, les avions sont chargés par l'effet triboélectrique quand ils sont frappés par des particules de précipitation [18, 19, 20, 21, 22, 23]. Le potentiel de l'avion est augmenté à un niveau élevé et le champ électrostatique peut être très fort. Par conséquent, des décharges corona se produisent sur les antennes bord et sur les autres extrémités de l'avion. Ces études ont conduit à l'invention des déchargeurs statiques qui sont monté à bord des aéronefs pour réduire le niveau du bruit [21]. Des travaux de recherche plus récent ont porté sur l'impact des décharges corona sur les avions composites [24].

Les interférences corona ont également été étudiées au sol, particulièrement sur les pylônes. Ces décharges introduisent un brouillage à large bande qui dégrade les signaux de télévision et des radioamateur [10, 25, 26]. Des disposition spécifiques de pylônes et d'antennes ont été proposées pour réduire le niveau d'interférence [10, 25].

Pour les station sol de radiocommunications de l'aviation civile, les antennes affectées par les décharges électrostatiques sont montés sur la partie supérieure des pylônes (plusieurs dizaines de mètres de haut). Les décharges sont probablement provoquées par un champ électrostatique fort d'origine naturelle. Il serait utile de développer un modèle pour prédire quantitativement le niveau de brouillage observé sur les antennes VHF. C'est le sujet de cette thèse.

2. Objectif de la thèse

L'objectif principal de cette thèse est de développer un modèle pour prédire quantitativement le niveau d'interférence introduit par des décharges corona sur les antennes VHF avec une géométrie de pylône et un champ électrostatique ambiant connus. Nous devons réaliser les tâches suivantes pour atteindre cet objectif

- montrer que les décharges corona sont à l'origine des brouillages observés sur les stations sol;
- localiser où les décharges corona se produisent sur les pylônes;
- étudier les caractéristiques des décharges corona et trouver un modèle qui peut représenter leur rayonnement dans la bande VHF;
- évaluer le niveau de brouillage introduit par les décharges corona aux ports des antennes, et comparer les résultats avec les mesures effectuées à la station de Champceuil.

3. Contribution

Pour atteindre ces objectifs, les travaux ont été divisé en différentes parties. Pour chaque partie, nous développons des modèles basés sur la physique avec des hypothèses cohérentes qui sont testées numériquement. Les contributions suivantes sont proposées:

- Nous comparons les mesures du champ électrostatique ambiant et des interférences VHF pour confirmer l'origine du brouillage.
- Nous localisons les endroits sur le pylône où les décharges corona se produisent probablement *via* une simulation électrostatique basée sur la méthode des éléments finis. La simulation électrostatique estime le champ électrostatique autour du pylône et des antennes pour un champ électrostatique ambiant connu. A partir des résultats de simulation, un critère est déterminé pour évaluer où les décharges corona se produisent le plus probablement.
- Nous proposo.ns et validons un modèle de dipôle élémentaire pour représenter le rayonnement des décharges corona dans le domaine fréquentiel. L'amplitude du

dipôle élémentaire est estimé au moyen d'approches déterministe et statistique basées sur les caractéristiques des décharges corona.

- Nous évaluons les niveaux d'interférence introduits par les décharges corona aux ports des antennes au moyen de simulations dans le domaine fréquentiel basées sur la méthode des moments. Les résultats de simulation sont comparés avec les mesures réalisés à la station de Champceuil.

4. Plan de thèse

Cette thèse est organisée comme suit:

Le **Chapitre 1** décrit le phénomène d'interférence et son origine. Dans un premier temps, nous présentons le système de télécommunication de l'aviation civile. Ensuite, le phénomène d'interférence est décrit. Ses origines possibles sont listées et analysées une par une pour le cas de Champceuil. Pour confirmer cette analyse, nous présentons des mesures simultanées des champs électrostatiques ambiants et des interférences VHF. Finalement, l'origine des interférences est identifié.

Le **Chapitre 2** présente le mécanisme et les caractéristiques des décharges corona. Les différences entre les décharges positives et négatives sont expliquées. Les caractéristiques essentielles des décharges corona, telles que la forme de l'impulsion, l'amplitude de l'impulsion, et le taux de répétition sont listées pour les deux types de décharge.

Le **Chapitre 3** présente les simulations électrostatiques pour localiser les endroits où les décharges corona peuvent se produire. Dans un premier temps, les équations de base gouvernant l'allumage des décharges corona et la méthode numérique pour les simulations électrostatiques sont présentées. Ensuite, nous faisons des simplifications pour rendre le problème calculable par la méthode des éléments finis. Enfin, pour le cas de Champceuil, le champ électrostatique autour du pylône est évalué à partir des simulations électrostatiques, et un critère pour déterminer où les décharges corona se produisent le plus probablement est proposé.

Le **Chapitre 4** présente le modèle utilisé pour représenter les décharges corona pour les simulations dans le domaine fréquentiel. Un modèle de dipôle élémentaire est proposé. Sa capacité à représenter le rayonnement des décharges corona dans la bande aéronautique VHF est vérifiée. Ensuite, au moyen d'approches déterministe et statistique, nous déterminons l'amplitude du dipôle élémentaire selon les caractéristiques des décharges corona dans la bande VHF.

Le **Chapitre 5** décrit des simulations dans le domaine fréquentiel afin d'évaluer le niveau d'interférence introduit par les décharges corona aux ports des antennes. Dans un premier temps, les modèles d'antennes sont présentés et testés pour avoir des performances réalistes. Ensuite, nous estimons les interférences introduites par les décharges corona pour chaque lieu possible de décharge. Puis, nous calculons les interférence introduites par les décharges corona se produisant simultanément dans des lieux différents. Enfin, le modèle est validé par comparaisons des simulations avec les résultats de mesures à la station Champceuil.

Chapitre 1 Phénomène d'interférence et son origine

Le but de ce chapitre est premièrement de décrire le phénomène d'interférence observé aux stations sol, et deuxièmement de trouver son origine. Dans ce chapitre, nous présentons le système radiocommunication utilisé de l'aviation civile. Ensuite nous décrivons et analysons le phénomène d'interférence observé sur les stations sol. Finalement nous trouvons son origine.

Dans la **section 1.1**, nous présentons le système de radiocommunications VHF de l'aviation civile. Les concepts importants, tels que la bande passante, les canaux vocaux, les émetteurs, les récepteurs, les antennes et le canal de propagation sont exposées. Le canal de propagation est expliqué plus précisément car c'est le lieu dans lequel les signaux VHF sont altérés par des phénomènes physiques différents. Nous expliquons certains détails du canal de propagation, incluant la distance limite de propagation, le bilan de liaison, l'effet multitrajet, et les interférences.

Dans la **section 1.2**, nous présentons le phénomène d'interférence. Premièrement, la station de Champceuil, qui est d'explorer tout en cette thèse, est présentée. Les antennes VHF installées sur le pylône de cette station incluent des antennes ground-planes et des couronnes d'antennes (voir Figure E.1). Puis, le phénomène d'interférence observé est décrit. Un bruit significatif est observé à certains de moments dont le niveau peut être 25dB plus fort que le niveau du bruit ambiant (voir Figure E.2 (a)).

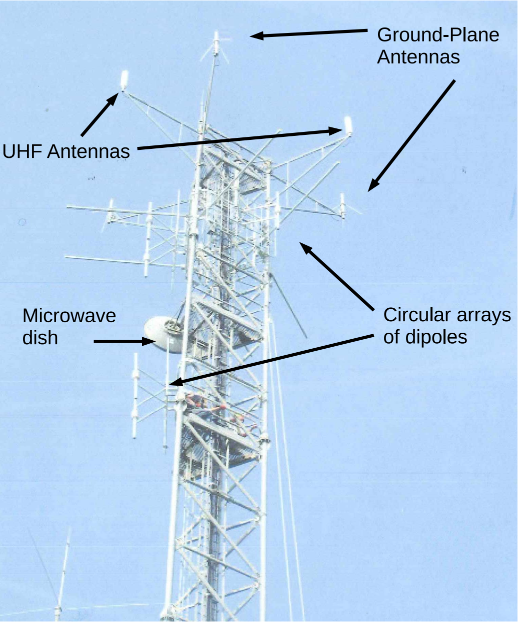

Figure E.1: Pylône et antennes de la station sol à Champcueil.

Dans la **section 1.3**, pour identifier l'origine de l'interférence observée, nous listons les origines possibles et les analysons une par une. Les origines possibles peuvent être divisés dans deux catégories: artificielles et naturelles.

Nous listons les origines possibles et les analysons. Les origine artificielles incluent

- la réception de signaux provoquant d'autres stations sols lors de l'existence de phénomène conduit atmosphérique: les signaux des autres stations sols sont aussi les voix et ils peuvent être identifié simplement. Les enregistrements bu brouillage montrent que elle n'est pas l'origine du brouillage car le bruit n'est pas la voix.
- les appareils rayonnant des forts signaux VHF: ce genre d'appareils peuvent être identifié simplement au moyen de mesure *via* une antenne directive. Les mesures ont été effectuées, et on n'a trouvé pas ce type d'appareils.
- les pannes des appareils: les appareils en panne peuvent être identifiés en vérifiant séparément les performances des appareils. Les mesures ont été faites, et on n'a trouvé pas de appareil en panne.

Les origines naturelles possibles incluent

- la foudre: les enregistrements du brouillage montrent que le bruit n'apparaît pas toujours simultanément avec le foudre, donc elle no provoque pas le bruit observé.
- les décharges électrostatiques de faible puissance: les décharges électrostatiques incluent aussi plusieurs types de décharges:
  - les décharges provoquées par précipitation électrostatique: les décharges de précipitation électrostatique apparaissent principalement sur les avions en vols. Le bruit observé aux stations sols n'est pas provoqué par elles.
  - les décharges sur les lignes de transmission haute tension: les décharges sur les lignes de transmission haute tension peuvent être détectées facilement via une antenne directive. Les mesures ont été effectuées. Elles montrent que le bruit n'est pas provoqué par ce type de décharge.
  - les décharges provoquées par un champ électrostatique fort naturel: aux stations sol, ce type de décharge peut être provoqué par un nuage chargé. Elles peuvent introduire un bruit dans la bande VHF, donc elles sont une origine possible du brouillage.

Finalement les décharges électrostatiques provoquées par un fort champ naturel peuvent être l'origine du brouillage. Il faut confirmer cette hypothèse.

Dans la **section 1.4**, nous présentons les mesures pour confirmer la hypothèse. S'il y a un champ électrostatique qui est plus fort qu'un champ critique, des décharges électrostatiques, et plus particulièrement des décharges corona se produisent. Le champs électrostatique autour le pylône de la station Champceuil a été mesuré *via* un moulin à champ. Les résultats de mesure ont montré qu'il existe une forte corrélation entre le niveau du champ électrostatique et le brouillage (voir Figure E.2 (b)). En conséquence, l'hypothèse que des décharges corona sont à l'origine du brouillage observé à la station sol a été vérifiée.

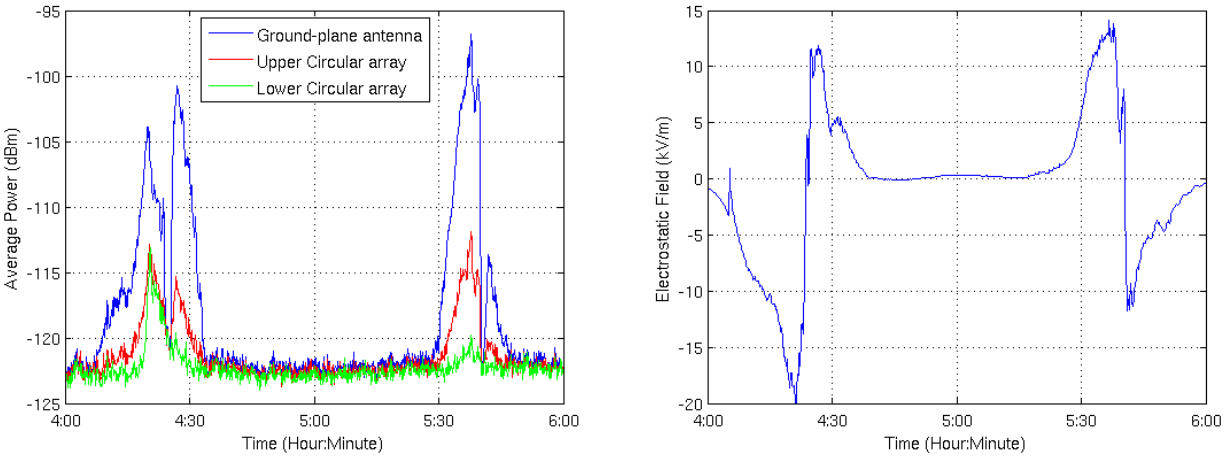

(a) (b)

Figure E.2: Résultat de mesure le 2 août 2007: (a) niveau du bruit par canal voix; (b) champ électrostatique.

Chapitre 2 Mécanisme et caractéristiques des décharges corona

Le but de ce chapitre est d'étudier le mécanisme des décharges corona et ses caractéristiques pour évaluer le niveau du bruit. Dans ce chapitre, nous décrivons premièrement les mécanismes des décharges corona pour mieux comprendre ce phénomène. Ensuite, nous présentons ses caractéristiques essentielles qui seront utilisées dans la suite de la thèse.

Dans la **section 2.1**, nous expliquons les mécanismes de génération de porteurs de charge. Les décharges électrostatiques se produisent entre les électrodes avec potentiels différents. Des milieux entre les électrodes sont normalement isolant. Pour notre cas, le milieu est l'air. En conséquence, des décharges électrostatiques commencent par la génération des porteurs de charge. Différent mécanismes de génération des porteurs de charge sont présentés. Ils incluent la photonionization, l'avalanche et l'émission d'électrons aux surfaces des électrodes.

Dans la **section 2.2**, nous présentons le streamer. Si le nombre des porteurs de charge est suffisant, le milieu isolant devient conducteur et la décharge électrostatique commencent. Le streamer est un canal faiblement ionisé formé à partir de l'avalanche. Il y a deux types du streamer: steamer positif et négatif qui dépendent de la polarisation d'électrode depuis laquelle le streamer se développe. Ils ont les caractéristiques à cause de les vitesses différentes des porteurs de charge: des ions pour le positif et des électrons pour le négative.

Dans Section 2.3, nous présentons les décharges corona. Tout d'abord, les mécanismes des décharges sont décrits. Ce sont des décharges électrostatiques se produisant là où le champ électrostatique est non-uniforme et plus fort qu'un champ critique. Ce type du champ se produit souvent au voisinage d'électrode avec petit rayon de couverture (elle s'appelle l'électrode active). Il y a deux types de la décharge corona: décharge positive et négative qui dépendent de la polarisation de l'électrode active. Elles se composent des streamers avec la même polarisation. Le courant du corona est une séries de pulses.
Ensuite, nous présentons les caractéristiques essentielles des décharges corona, incluant le champ critique, la taille de la région du corona, la forme du courant de décharge, son

spectre, son amplitude et le taux de répétition du pulse. Les caractéristiques essentielles sont résumées dans le tableau E.7.

Caractéristiques	Corona positive	Corona négative
Temps de monté (ns)	30	10
Temps de descente (ns)	200	70
Amplitude du pulse (mA)	[2, 120]	[1, 50]
Taux de répétition (kHz)	[0.1, 4]	[1, 100]
Taille de la région de décharge	quelque cm	quelque cm

Table E.7: Résumé des caractéristiques des décharges corona.

Chapitre 3 Simulations électrostatiques

Le but de ce chapitre est de localiser les endroits où les décharges corona se produisent. Dans le chapitre précédent, nous avons vu que les décharges corona se produisent aux lieux où le champ électrostatique est plus fort qu'un champ critique. Dans ce chapitre, nous proposons une méthode au moyen de faire des simulation électrostatique pour estimer le champ électrostatique autour du pylône, et puis localiser des décharges corona. Nous évaluons le champ électrostatique par résolution des équations *via* une méthode numérique (la méthode des éléments finis).

Dans la **section 3.1**, nous présentons les équations de base gouvernant des décharges. L'équation à résoudre pour les simulations électrostatiques est de $\nabla \cdot (\varepsilon \nabla V) = -\rho(t)$, avec ε la permittivité du milieu, V le potentiel électrique et $\rho(t)$ la densité de charge dans le milieu.

Dans la **section 3.2**, nous décrivons la méthode des éléments finis.

Dans la **section 3.3**, nous proposons des simplifications pour rendre le problème calculable par la méthode des éléments finis.

Premièrement, nous simplifions l'équation à résoudre. Nous supposons que les simulations électrostatiques sont effectuées juste avant des décharges, la densité de charge dans l'air est donc négligeable. En conséquence, l'équation à résoudre devient $\nabla \cdot (\varepsilon \nabla V) = 0$. Pour résoudre les équations, les conditions limites sont nécessaire. Nous supposons que la différence de potentiels entre le nuage chargé et le sol est constante. Le sol est donc représenté par une électrode de sol avec un potentiel de zéro. L'électrode de sol incluent le sol et le pylône. Nous supposons que le sol est plat et le pylône est représenté par une structure métallique solide. Ensuite, nous supposons que les nuages chargés sont représentés par un électrode de ciel plate au-dessus du pylône. Le potentiel de l'électrode de ciel est déterminée à partir du champ ambiant (champ électrostatique sans l'influence du pylône) et de la hauteur de l'électrode de ciel.

La méthode des éléments finis nécessite un domaine de calcul limité. Nous choisissons donc le domaine de calcul comme une boîte. Les frontières latérales sont verticales et nous supposons qu'elles se situent assez loin du pylône. La condition aux limites aux frontières latérales est $\frac{\partial V}{\partial \mathbf{n}} = 0$.

Les bâtiments des stations sols sont normalement petits par rapport au pylône. Nous supposons donc que ce bâtiment est négligeable, et l'équation à résoudre devient $\nabla^2 V = 0$.

Dans la **section 3.4**, nous vérifions que le modèle proposée dans la section 3.3 peut représenter le cas réel en l'appliquant à la station de Champceuil, puis en testant les hypothèse une par une.

Tout d'abord, nous considérons la station de Champceuil comme cas de test (voir Figure E.3), et nous vérifions que les simulations électrostatiques donnent des résultats physiquement corrects (voir Figure E.4).

En suite, nous proposons une méthode pour évaluer quantitativement les influences des différentes hypothèses par comparaison avec des résultats de références. Plus précisément, nous choisissons de comparer les potentiels le long des axes des antennes (voir Figure 3.7). Nous définissons une différence quadratique moyenne normalisée ϵ comme

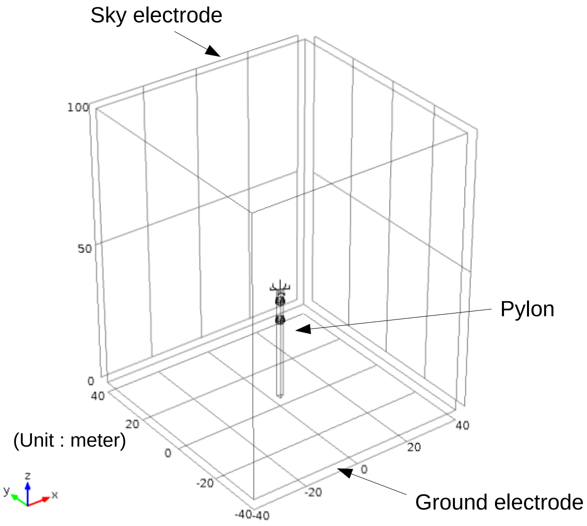

Figure E.3: Cas test basé sur la station de Champceuil.

(3.12). Si $\epsilon < 0.05$, nous considérons que les résultats de simulation sont en accord avec les références. Nous effectuons des simulations électrostatiques et appliquons cette méthode aux hypothèses proposées précédemment. Les résultats des simulations montrent que le modèle proposé représente avec précision le cas réel. Le cas test de la station Champceuil peut être utilisé pour les simulations électrostatiques.

Dans la **section 3.5**, nous proposons un critère pour localiser les décharges corona. Elles se produisent aux bords pointus où le champ électrostatique est très fort. Ces bords ont de petits rayons de courbures. Le champ critique peut être évalué par la formule de Peek (2.1). Toutefois, dans notre modèle, les parties pointues sont modélisées par des arêtes parfaites dont le rayon de courbure est nul. A cause de la singularité, le champ électrostatique ne peut pas être calculé sur l'arête. Nous proposons une méthode par définir un champ critique $E_{\mathbf{cd}}$ à une distance d du bord. Par comparaison entre le champ critique $E_{\mathbf{cd}}$ et le champ calculé à une distance d, nous pouvons connaître les lieux où les décharges corona se produisent.

Dans la **section 3.6**, nous localisons les décharges corona. Nous listons les lieux possibles de décharge à la station de Champceuil. En plus, nous définissons des groupes de lieux

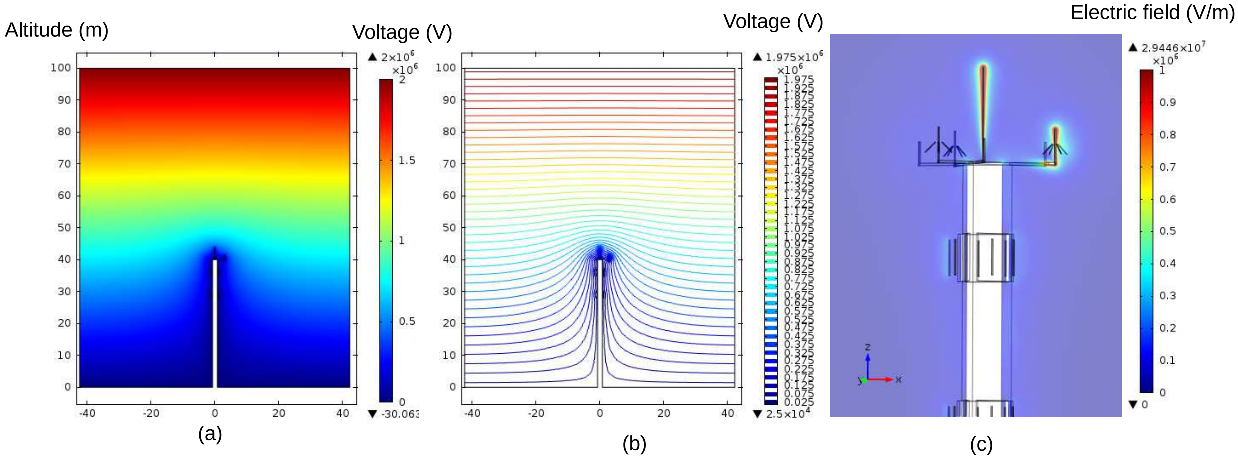

Figure E.4: Résultat de simulation dans un plan vertical incluant le paratonnerre et une antenne ground-plane: (a) potentiel; (b) lignes equi-potentiels et (c) champ électrostatique autour au sommet du pylône.

pour lesquels les décharges corona se produisent à partir de la même valeur de champ ambiant. Ces groupes sont directement liés à leur hauteur sur le pylône (voir Tableau E.8).

No.	Lieux où les décharges corona se produisent simultanément
1	Sommet du paratonnerre
2	Sommet du paratonnerre, extrémités des antennes ground-plane et des antennes UHF
3	Sommet du paratonnerre, extrémités des antennes ground-plane, des antennes UHF et des antennes couronnes

Table E.8: Groupes de lieux où les décharges corona se produisent simultanément.

Chapitre 4 Sources représentant les rayonnement VHF des décharges corona

Dans ce chapitre, nous proposons une source qui peut représenter le rayonnement des décharges corona dans la bande VHF afin de pouvoir évaluer le niveau d'interférence introduit par les décharges. Premièrement nous proposons un modèle basé sur un dipôle électrique élémentaire. Nous vérifions sa capacité de représenter les décharges corona dans la bande VHF. Ensuite, nous déterminons l'amplitude du dipôle élémentaire selon les caractéristiques des décharges corona dans la bande VHF dans les littératures.

Dans la **section 4.1**, nous proposons le modèle du dipôle élémentaire. Nous présentons son rayonnement en l'espace libre, et vérifions qu'il peut représenter le rayonnement des décharges corona dans la bande VHF.

Dans la **Section 4.2**, nous déterminons l'amplitude du dipôle élémentaire. Dans la littérature, nous trouvons les caractéristiques des décharges corona (voir Tableau E.7). Nous déterminons l'amplitude du dipôle élémentaire par des approches déterministe et statistique. Dans l'approche déterministe, nous supposons que les pulses des décharges corona sont purement périodique, c'est-a-dire l'amplitude et l'espacement temporel entre les pulses sont constants. Dans l'approche statistique, nous supposons l'amplitude et l'espacement temporel entre les pulses sont variables. Ces deux approches donnent presque les mêmes résultats pour l'amplitude du dipôle élémentaire, car les niveaux moyens des amplitudes et séparations de l'approche statistique correspondent aux valeurs constantes de l'approche déterministe. Nous trouvons que dans un canal vocal de 8.33kHz, l'amplitude du dipôle élémentaire est $0.679\mu\mathrm{A}\cdot\mathrm{mm}$ pour des décharges corona positives, et $3.82\ mu\mathrm{A}\cdot\mathrm{mm}$ pour les décharges négatives.

Chapitre 5 Simulations dans le domaine fréquentiel

Dans ce chapitre, nous effectuons les simulations dans le domaine fréquentiel pour évaluer le niveau de bruit introduit par les décharges corona. Nous prenons la station de Champceuil comme exemple. Premièrement nous présentons la méthode numérique utilisée, ensuite les modèles des antennes. Nous définissons un niveau de référence du bruit correspondant au bruit typique introduit par des sources de bruit classique. Puis nous effectuons les simulations pour évaluer le niveau d'interférence introduit par chaque lieu de décharge corona. Enfin, nous présentons les niveaux d'interférence lorsque les décharges corona se produisent simultanément à différents endroits.

Dans la **Section 5.1**, nous présentons la méthode numérique avec laquelle les simulations dans le domaine fréquentiel sont effectuées. La méthode utilisée est la méthode des moments. Pour réduire le temps de calcul, nous modélisons le pylône comme une structure filaire.

Dans la **Section 5.2**, nous développons des modèles pour les antennes VHF. Les modèles des antennes sont ajustés afin d'avoir des performances réalistes (diagramme de rayonnement et adaptation). L'influence de la présence du pylône est aussi étudiée.

Dans la **Section 5.3**, nous proposons un niveau de référence de bruit en-dessous duquel le bruit provoqué par des décharges corona devient négligeable. Nous définissons un bruit dont le température de bruit est de l'ordre de la température ambiante. Pour un canal vocal dans la bande VHF, la puissance de référence du bruit est alors de $P_{\text{ref}} = -134\text{dBm}$.

Dans la **Section 5.4**, nous effectuons les simulations pour évaluer le niveau d'interférence introduit par les décharges corona à un seul endroit. Nous calculons le niveau de bruit qui correspond au bruit reçu sur un canal vocal B_{c}. Pour chaque canal vocal, nous effectuons la simulation sur sa fréquence centrale. Pour évaluer le niveau de bruit provoqué par des décharges corona à un seul endroit, nous plaçons une source de dipôle élémentaire au lieu spécifié. Le niveau de bruit est la puissance sur une impédance adaptée reliée au port d'accès de l'antenne.
Les lieux possibles de décharge identifiés dans le Chapitre 3 incluent

- sommet du paratonnerre;
- extrémités hautes et basses des antennes ground-planes;
- sommets des antennes UHF;
- extrémités des dipôles des antennes couronnes.

Pour chaque lieu, nous évaluons le bruit introduit au niveau des antennes. Les résultats montrent que les décharges corona aux sommet du paratonnerre n'introduisent pas de brouillage significatif aux antennes par rapport au niveau de référence du bruit. Ainsi, pour chaque antenne VHF, le bruit reçu est principalement provoqué par des décharges corona se produisant sur l'antenne elle-même.

Dans la **section 5.5**, nous calculons le niveau de bruit introduit par des décharges corona se produisant simultanément dans différents lieux. Des décharges corona peuvent se produire simultanément à différentes endroits. Ces décharges ne sont pas corrélées, donc pour une seule antenne, le bruit introduit par l'ensemble des lieux de décharges est le somme des bruits introduits en chaque lieu.

Dans le chapitre 3, nous avons défini des groupes d'endroits pour lesquels les décharges corona se produisent à partir de la même valeur du champ ambiant (voir Tableau E.8). Nous calculons ici le niveau de bruit correspondant à ces groupes, et présentons les résultats dans les tableaux E.9 et E.10 pour des décharges positives et négatives.

No.de groupe	Bruit reçu par l'antenne ground-plane (dBm)	Bruit reçu par l'antenne couronne supérieure (dBm)	Bruit reçu par l'antenne couronne inférieure (dBm)
1	-132.6	-146.5	-153.8
2	-97.3	-114.7	-128.6
3	-97.3	-113	-118.2

Table E.9: Bruit-par-canal-vocal moyen introduit aux ports des antennes par des décharges corona positives simultanées en différents lieux.

No.de groupe	Bruit reçu par l'antenne ground-plane (dBm)	Bruit reçu par l'antenne couronne supérieure(dBm)	Bruit reçu par l'antenne couronne inférieure(dBm)
1	-117.5	-131.4	-138.7
2	-81.2	-99.6	-113.5
3	-81.2	-97.9	-103.1

Table E.10: Bruit-par-canal-vocal moyen introduit aux ports des antennes par des décharges corona négatives simultanées en différents lieux.

Ces résultats montrent que pour le cas no.1, le bruit provoqué par des décharges corona est faible. Pour le cas no.2, toutes les antennes reçoivent un bruit plus fort que le niveau de référence du bruit. Pour le cas no.3, le niveau de bruit sur les antennes couronnes augment, particulièrement pour la couronne inférieure.

Dans la **section 5.6**, nous comparons les résultats des simulations présentées dans la section 5.5 avec des résultats de mesures. Tout d'abord, parce que les résultats des mesures sont observés *via* des récepteurs, nous faisons une calibration pour éliminer le bruit du récepteur. Nous montrons le niveau maximal de bruit pendant les mesures à la station de Champceuil sur Tableau E.11.

Antennes	Niveau maximal du bruit décharges positives (dBm)	Niveau maximal du bruit décharges négatives (dBm)
Antenne ground-plane	-96	-103
Antenne couronne supérieure	-111	-112
Antenne couronne inférieure	-120	-113

Table E.11: Niveaux maximaux des décharges corona pendant les mesures à la station de Champceuil.

La comparaison entre les résultats des simulations et les mesures montrent que pour les décharges corona négatives, le bruit mesuré est plus faible que celui calculé par simulations. Cela peut s'expliquer par les incertitudes sur les amplitudes des pulses et sur le taux de répétition. Pour les décharges corona positives, les mesures sont en accord avec les simulations du cas no.2.

Conclusion

1. Résumé des travaux

L'objectif principal de cette thèse était de développer un modèle pour prédire quantitativement le niveau d'interférence induit par des décharges corona sur une antenne VHF pour une géométrie de pylône et un champ électrostatique ambiant connu.

Pour atteindre cet objectif, nous avons défini plusieurs sous-objectifs. Le premier était de prouver que les décharges corona sont à l'origine des interférences observées aux stations sols. Le second était de localiser où les décharges corona se produisent le plus probablement sur le pylône. Le troisième était d'étudier les caractéristiques des décharges corona et de trouver un modèle qui peut représenter leur rayonnement dans la bande VHF. Le dernier était d'évaluer le niveau de brouillage introduit par des décharges corona aux antennes, et comparer les résultats avec les mesures qui ont été effectuées à la station de Champceuil.

Dans le **chapitre 1**, nous avons étudié l'origine des phénomènes d'interférence. Nous avons pris la station de Champceuil comme exemple. Dans un premier temps, nous avons présenté le système de télécommunication altéré par les interférences. Nous avons ensuite décrit l'interférence observée, listé et analysé ses possibles origines. Nous avons trouvé que la raison la plus probable pour ce bruit est des décharges électrostatiques provoquées par le champ électrostatique ambiant naturel. Pour confirmer l'analyse, des mesures simultanées du champ électrostatique ambiant et du niveau de bruit VHF sur place ont été présentées. Nous avons trouvé qu'il existe une forte corrélation entre le champ électrostatique ambiant et le niveau du brouillage VHF. Par conséquence, nous avons conclu que les décharges électrostatiques provoquées par le champ électrostatique ambiant naturel sont la cause la plus probable des interférences observées aux stations sols.

Dans le **chapitre 2**, nous avons étudié le mécanisme et les caractéristiques des décharges corona. Deux types de décharges corona ont été présentés, appelés les décharges positives et négatives. ils génèrent une série d'impulsions qui se produisent aux lieux où il y a des forts champs électrostatiques non uniformes. Nous avons vu que la physique des décharges positive et négative sont différentes. Pour les deux types de décharges corona, nous avons listé les caractéristiques essentielles, telles que la forme d'impulsion, l'amplitude et le taux de répétition.

Dans le **chapitre 3**, nous avons localisé où des décharges corona se produisent le plus probablement sur le pylône. Dans un premier temps, nous avons présenté les équations et la méthode numérique (méthode des éléments finis) pour les simulations électrostatiques. Deuxièmement, nous avons fait des simplifications pour rendre le problème calculable par la méthode des éléments finis. Ensuite, le modèle a été validé sur la station de Champceuil. En troisième lieu, afin d'éviter la singularité provoquée par les arêtes dans le modèle, nous avons développé un critère pour le déclenchement des décharges corona. Ce critère consiste à comparer le champ électrostatique calculé avec un champ critique à une distance donnée des bords. Enfin, nous avons effectué des simulations électrostatiques pour estimer le champ électrostatique autour du pylône, ceci afin de localiser les décharges corona. Nous avons trouvé les lieux où les décharges corona se produisent le plus probablement. Nous avons défini des groupes d' endroits pour lesquels les décharges corona se produisent à partir de la même valeur du champ ambiant. Ces groupes sont directement liés à la hauteur des lieux possibles de décharge.

Dans le **chapitre 4**, nous avons développé un modèle pour représenter le rayonnement des décharges corona pour les simulations dans le domaine fréquentiel. Tout d'abord, nous avons proposé un modèle de dipôle élémentaire. Nous avons vérifié qu'il peut représenter le rayonnement des décharges corona dans la bande VHF. Ensuite, nous avons déterminé l'amplitude du dipôle élémentaire selon les caractéristiques des décharges corona dans la bande VHF au moyen d'approches déterministe et statistique.

Dans le **chapitre 5**, nous avons effectué des simulations dans le domaine fréquentiel pour évaluer le niveau de brouillage introduit par les décharges corona aux antennes. Tout d'abord, nous avons développé des modèles d'antennes avec des performances réalistes. Ensuite, nous avons estimé le bruit introduit par les décharges corona dans chaque lieu au moyen de simulations dans le domaine fréquentiel avec des dipôles élémentaires placés à chaque endroit. Nous avons constaté que, pour chaque antenne VHF, le bruit reçu est principalement provoqué par des décharges corona se produisant sur l'antenne elle-même. Enfin, nous avons calculé les niveaux de bruit introduits par les décharges corona se produisant simultanément dans des différents endroits. Nous avons comparé les résultats des simulations avec les résultats de mesures recueillis à la station de Champceuil. Pour des décharges corona négative, les niveaux de bruit mesurés sont plus faibles que les bruits simulés. Par contre, pour les décharges positives, ils sont en accord.

2. Recommandation pour la réduction du bruit de corona

Pendant le processus utilisé pour atteindre l'objectif principal de cette thèse, nous avons tiré des conclusions qui peuvent être utiles pour réduire le niveau de bruit causé par des décharges corona.

Nous avons trouvé que, pour chaque antenne, le bruit reçu est principalement causé par des décharges corona se produisant sur l'antenne elle-même. Par conséquent, un moyen pratique pour réduire le niveau de bruit est d'éviter les décharges corona se produisant sur l'antenne en réduisant le niveau du champ électrostatique autour de l'antenne. Pour cela, plusieurs méthodes possibles peuvent être imaginées.

La première est d'augmenter la longueur du paratonnerre. Un paratonnerre plus long peut fournir une meilleure protection pour les antennes, donc le champ électrostatique autour des antennes sera affaibli, et la possibilité de décharge sera réduit.

La seconde est d'éviter d'installer les antennes au sommet du pylône. Les simulations ont montré que, malgré la présence d'un paratonnerre, le champ électrostatique au sommet du pylône peut être encore relativement fort. Si les antennes sont installées quelque mètres au-dessous du sommet, le champ électrostatique sera beaucoup plus faible et la possibilité de décharge sera réduit.

La troisième est d'ajouter des tiges de blindage supplémentaire pour les antennes. Ces tiges de blindage peuvent fonctionner comme des petits "paratonnerre" et fournir une protection pour les antennes à proximité sur lesquelles le champ électrostatique sera réduit. Souny [71] a proposé une telle méthode pour réduire le niveau de bruit aux antennes couronnes à la station Champceuil. Il convient de noter que les tiges de blindage supplémentaires peuvent influencer le diagramme de rayonnement des antennes. En conséquence, les aspects VHF doivent être pris en compte pour la conception des tiges.

La quatrième est de choisir des antennes convenables. Les décharges corona se produisent généralement aux bords pointus des extrémités cylindriques des dipôles. Par conséquent, si l'antenne VHF a moins de bords ou extrémités pointus, la possibilité de décharge sera réduit.

3. Perspectives

A courte terme, nous pourrions premièrement étudier plus de cas d'interférence observées aux stations au sol. Dans cette thèse, nous avons considéré la station Champceuil comme un exemple pour l'analyse. Les phénomènes d'interférence ont également été observés dans d'autres stations sol. Nous pouvons étudier ces cas pour vérifier et affiner le modèle.

Deuxièmement, nous pourrions effectuer des mesures pour déterminer des valeurs plus précises pour l'amplitude du dipôle élémentaire représentant les décharges corona dans la bande VHF. Ces valeurs doivent dépendre de la configuration et du champ électrostatique ambiant. Dans cette thèse, nous avons estimé ces valeurs au moyen d'approches basées sur les caractéristiques trouvées dans la littérature. Pour les décharges négatives, l'incertitude sur l'amplitude des décharges est suffisamment grande pour obtenir des différences significatives entre les simulations et les mesures. Des mesures directes du rayonnement VHF des décharges corona peuvent fournir des résultats plus précis. Certaines mesures ont été effectuées dans la littérature, mais elles présentent des limitations. Tout d'abord, les mesures sont influencées par l'environnement. Une solution possible serait d'effectuer des mesures dans une chambre anéchoïque. Deuxièmement, un déchargeur corona normal ne rayonne pas de manière efficace dans la bande VHF. Par conséquent, le système de décharge doit être couplé à un élément résonnant dans la bande VHF. Une méthode possible serait de générer directement des décharges corona sur une antenne VHF réel. Au cours de cette thèse, les premiers essais ont été faits, mais la conception d'un déchargeur corona avec de bonnes capacités de rayonnement VHF était hors du cadre de cette thèse.

Troisièmement, nous pouvons essayer d'étudier le bruit introduit par des décharges corona dans d'autres bandes de fréquences. Les principes seraient les mêmes que ceux présentés dans cette thèse.

A long terme, on peut envisager d'appliquer cette méthode à d'autres domaines où les décharges corona produisent des interférences. Par exemple, pour le domaine des avions en vol, nous pourrions utiliser notre méthode pour prédire le niveau d'interférence du corona, ou pour optimiser des déchargeurs statiques montés sur avion.

Bibliography

[1] *IACO Annex 10 Volume 3*, International Civil Aviation Orgnization Std., July 2007.

[2] F. Gordon and W. Morgan, *Principles of communications satellites.* John Wiley, New York, 1993.

[3] A. Azoulay, "Etude des brouillage sur le site DGAC de Champcueil, rapport no.4 simulation de brouillage par décharge électrostatiques„" consultant radiocommunications et electromagnétisme, Rapport d'étude pour la DGAC-DSNA-DTI, Septembre 2006.

[4] B. Souny, "Test d'un moulin à champ type Previstorm bruit émis dans la gamme VHF," Rapport d'étude pour DGAC-DSNA-DTI, ENAC/LETA, 2007.

[5] R. Myron, "Movement of air in the electric wind of the corona discharge," *American Institute of Electrical Engineers, Part I: Communication and Electronics, Transactions of the*, vol. 80, pp. 143–150, 1961.

[6] Y. P. Raizer, *Gas Discharge Physics.* Belin: Ellipses, Berlin, 1991.

[7] H. Hucke, "Precipitation-static interference on aircraft and at ground stations," *Proceedings of the IRE*, vol. 27, pp. 301–316, 1939.

[8] R. Olsen, "Power-transmission electromagnetics," *Antennas and Propagation Magazine, IEEE*, vol. 36, no. 6, pp. 7–16, December 1994.

[9] R. L. Tanner, "An analysis of corona-generated interference in aircraft," *Proceedings of the IEEE*, vol. 52, no. 1, pp. 44–52, January 1964.

[10] H. Page and D. J. Whythe, "Corona and precipitation interference in VHF television reception," *Proceedings of the Institution of Electrical Engineers*, vol. 114, no. 5, pp. 566–576, May 1967.

[11] C. Helstrom, "The spectrum of corona noise near a power transmission line," *Power Apparatus and Systems, Transactions of the American Institute of Electrical Engineers*, vol. 80, no. 3, pp. 831–835, April 1961.

[12] D. A. Rickard, N. Harid, and R. Waters, "Modelling of corona at a high-voltage conductor under double exponential and oscillatory impulses," *Science, Measurement and Technology, IEE Proceedings*, vol. 143, pp. 277–284, 1996.

[13] A. J. Otto and H. Reader, "Wideband and narrowband HVDC conductor corona test methods for radio noise prediction," *Power Delivery, IEEE Transactions on*, vol. 25, pp. 2950–2957, October 2010.

[14] Z. Zhang, R. Rong, and Z. Yu, "Measurement of corona characteristics and electromagnetic environment of ±800kV HVDC transmission lines under high altitude condition," in *Progress In Electromagnetics Research Synposium Proceedings, Moscow, August 18-21*, 2000.

[15] S. Masuda, H. Nakatani, and S. Hosokawa, "Modification in waveform of traveling pulse voltages due to corona production along transmission line," *Industry Applications, IEEE Transactions on*, vol. IA-21, pp. 724–732, 1985.

[16] S. El-Debeiky and M. Khalifa, "Calculating the corona pulse characteristics and its radio interference," *Power Apparatus and Systems, IEEE Transactions on*, vol. PAS-90, pp. 165–179, 1971.

[17] R. Olsen and B. Stimson, "Predicting VHF/UHF electromagnetic noise from corona on power-line conductors," *Electromagnetic Compatibility, IEEE Transactions on*, vol. 30, no. 1, pp. 13–22, February 1988.

[18] R. Gunn, W. Hall, and G. Kinzer, “Army-navy precipitation-static project: Part I-the precipitation-static interference problem and methods for its investigation,” *Proceedings of the IRE*, vol. 34, pp. 156–161, 1946.

[19] R. C. Waddel, R. Drutowski, and W. Blatt, “Army-navy precipitation-static project: Part II-aircraft instrumentation for precipitation-static research,” *Proceedings of the IRE*, vol. 34, pp. 161–166, 1946.

[20] R. G. Stimmel, E. H. Rogers, F. E. Waterfall, and G. R., “Army-navy precipitation-static project part III–electrification of aircraft flying in precipitation areas,” *Proceedings of the IRE*, vol. 34, pp. 167–177, 1946.

[21] G. Kinzer and J. McGee, “Army-navy precipitation-static project: Part IV-investigations of methods for reducing precipitation-static radio interference,” *Proceedings of the IRE*, vol. 34, pp. 234–240, 1946.

[22] R. Gunn and J. Parker, “Army-navy precipitation-static project: Part V-the high-voltage characteristics of aircraft in flight,” *Proceedings of the IRE*, vol. 34, pp. 241–247, 1946.

[23] M. Newman and A. O. Kemppainen, “Army-navy precipitation-static project: Part VI high-voltage installation of the precipitation-static project,” *Proceedings of the IRE*, vol. 34, pp. 247–254, 1946.

[24] H. Fu, Y. Xie, and Z. J., “Analysis of corona discharge interference on antennas on composite airplanes,” *Electromagnetic Compatibility, IEEE Transactions on*, vol. 50, pp. 822–827, 2008.

[25] K. Arai, W. Janischewskyj, and N. Miguchi, “Micro-gap discharge phenomena and television interference,” *Power Apparatus and Systems, IEEE Transactions on*, vol. PAS-104, pp. 220–232, 1985.

[26] C. F. Clark and M. Loftness, “Some observations of foul weather EHV television interference,” *Power Apparatus and Systems, IEEE Transactions on*, vol. 1157-1168, p. 1970, PAS-89.

[27] W. Hioki, *Telecommunications (4th Edition).* Prentice Hall, 2000.

[28] C. A. Balanis, *Antenna Theory: Analysis and Design*, 2nd ed. John Wiley, New Jersy, 1997.

[29] N. Blaunstein and C. Christodoulou, *Radio propagation and adaptive antennas for wireless communication links - terrestrail, atmospheric and ionospheric.* John Wiley & Sons, INC., USA, 2007.

[30] *International standard CISPR 11 Industrial, scientific and medical equipment – Radio-frequency disturbance characteristics – Limits and methods of measurement*, International Electrotechnical Commission (IEC) Std. 11, 2009.

[31] A. Orlandi and R. Scheich, "EMC in power electronic devices: radiated emissions from a silicon controlled rectifier," in *Electromagnetic Compatibility, 1994. Symposium Record. Compatibility in the Loop., IEEE International Symposium on.*

[32] C. Baum, L. Baker, and R. Gardner, *Lightning Electromagnetic*, R. Gardner, Ed. Hemisphere Publishing Corporation, New York, 1990.

[33] M. Mardiguian, *Electrostatic Discharge understand, simulate and fix ESD problems.* John Wiley & Sons, INC., USA, 2009.

[34] J. E. Nanevicz, "Static charging and its effects on avionic systems," *IEEE Transactions on electromagnetic compatability*, vol. EMC-24, pp. 203–209, 1982.

[35] K. Kawamata and S. Minegishi, "Measurements of characteristics of electromagnetic radiation caused by electrostatic discharges in metal sphere gap at voltages less than 1 kv," *Communications, China*, vol. 10, pp. 29–35, 2013.

[36] R. L. Tanner and J. E. Nanevicz, "Radio noise generated on aircraft surfaces," stanford Res. Inst., Menlo Park, Calif., Final Rept., SRI Project 1267, Contract AF 33(616)-2761; September, 1956.

[37] M. Abdel-Salam and E. Abdel-Aziz, "Improved calculation for corona loss on three-phase power transmission lines," in *Industry Applications Society Annual Meeting, Conference Record of the 1994 IEEE.*

[38] D. Cao, X. Qie, S. Duan, J. Yang, and Y. Xuan, "Observations of VHF source radiated by lightning using short baseline technology," in *Electromagnetic Compatibility (APEMC), 2010 Asia-Pacific Symposium on*, 2010, pp. 1162–1165.

[39] C. Leboeuf, J. Roque, and J. Guegand, *Cours de probabilités et de statistiques.* Paris: Ellipses, Paris, 1981.

[40] P. Seimandi, "Modélisation mathématique et numérique de décharges couronnes pour le contrôle d'écoulements," Ph.D. dissertation, l'Université Toulouse III - Paul Sabatier, 2010.

[41] L. Loeb, *Electrical Coronas, Their Basic Physical Mechanisms.* University of California Press, 1965.

[42] A. Kulikovsky, "Positive streamer between parallel plate electrodes in atmospheric pressure air," *Journal of Physics D: Applied Physics*, vol. 30, pp. 441–450, 1997.

[43] A. Samusenko, D. Sokolov, and Y. Stishkov, "Computer simulation of a negative streamer in uniform electric field," in *Electrical Insulation and Dielectric Phenomena (CEIDP), 2010 Annual Report Conference on.*

[44] J. Chang, P. Lawless, and T. Yamamoto, "Corona discharge processes," *Plasma Science, IEEE Transactions on*, vol. 19, pp. 1152–1166, 1991.

[45] M. Goldman, A. Goldman, and R. Sigmond, "The corona discharge, its properties and specific uses," *Pure Appl. Chem*, vol. 57, pp. 1353–1362, 1985.

[46] P. Peek, *Dielectric phenomena in high voltage engineering.* McGraw-Hill Press, 1929.

[47] M. Khalifa and M. Abdel-Salam, "Improved calculation of corona pulse characteristics," *IEEE Transactions on Power Apparatus and Systems*, vol. PAS-93, pp. 1693–1699, 1974.

[48] W. Janischewskyj and A. Arainy, "Corona characteristics of simulated rain," *Power Apparatus and Systems, IEEE Transactions on*, vol. PAS-100, pp. 539–551, 1981.

[49] B. Rakoshdas, "Pulses and radio-influence voltage of direct-voltage corona," *Power Apparatus and Systems, IEEE Transactions on*, vol. 83, pp. 483–491, 1964.

[50] M. Abdel-Salam, A. Fattah, M. Saied, and M. Tharwat-El-Mohandes, "Positive corona pulse characteristics from two interacting needles in air," *Industry Applications, IEEE Transactions on*, vol. IA-21, pp. 912–918, 1985.

[51] M. Boutlendj and N. Allen, "Current-density distribution on a plane cathode in DC glow and streamer corona regimes in air," *Electrical Insulation, IEEE Transactions on*, vol. 28, pp. 86–92, 1993.

[52] B. Khaddour, P. Atten, and J. Coulomb, "Numerical solution and experimental test for corona discharge between blade and plate," *Magnetics, IEEE Transactions on*, vol. 43, pp. 1193–1196, 2007.

[53] M. Madani and T. Miller, "Current density distribution measurement of negative point-to-plane corona discharge," *Instrumentation and Measurement, IEEE Transactions on*, vol. 47, pp. 907–913, 1998.

[54] P. Wilson and M. Ma, "Field radiated by electrostatic discharges," *Electromagnetic Compatibility, IEEE Transactions on*, vol. 33, pp. 10–18, 1991.

[55] A. C. Polycarpou, *Introduction to the Finite Element Method in Electromagnetics.* Morgan & Claypool publishers, USA, 2006.

[56] P. P. Silvester and R. L. Ferrari, *Finite Elements For Electrical Engineers*, second edition ed. Cambridge University Press, Cambridge, 1990.

[57] J. Jin, *The Finite Element Method in Electromagnetics.* John Wiley & Sons, INC., USA, 1993.

[58] J. N. Reddy, *An introduction to the finite element method*, third edition ed. McGraw-Hill, USA, 2006.

[59] J. Reitz, F. Milford, and R. Christy, *Foundations of Electromagnetic Theory.* Addison-Wesley, 1987.

[60] C. Thajudeen, A. Hoorfar, and F. Ahmad, "Measured complex permittivity of walls with different hydration levels and the effect on power estimation of TWRI target returns," *Progress In Electromagnetics Research B*, vol. 30, pp. 177–199, 2011.

[61] E. Rothwell and M. Cloud, *Electromagnetics, Second Edition.* CRC Press, 2009.

[62] S. Chen, Y. Sun, and H. Xie, "Characteristics of electromagnetic wave radiated from corona discharge," in *Electromagnetic Compatibility. 2001 IEEE International Symposium on*, 2001, pp. 1279–1282.

[63] S. Nayak and M. Thomas, "A novel technique for the computation of radiated EMI due to corona on HV transmission lines," in *Electromagnetic Compatibility, 2003 IEEE International Symposium on*, vol. 2, 2003, pp. 738–742.

[64] T. Hoshino, M. Hikita, and H. Okobo, "Radiation mechanism of electromagnetic wave from partial discharge analyzed by half-wave dipole antenna model," in *Proceeding of the 10th international symposium on high voltage engineering*, 1997, pp. 189–192.

[65] D. Middleton, "Non-Gaussian noise models in signal processing for telecommunications: new methods an results for class A and class B noise models," *Information Theory, IEEE Transactions on*, vol. 45, pp. 1129–1149, 1999.

[66] J. Max, *Méthodes et techniques de traitement du signal et applications aux mesures physiques, Tome 1.* Masson, Paris, 1985.

[67] N. Malik and A. A. Al-rainy, “Stastical variation of DC corona pulse amplitudes in point-to-plane air gaps,” *Electrical Insulation, IEEE Transactions on*, vol. EI-22, pp. 825–829, 1987.

[68] A. Oppenheim and R. Schafer, *Discrete-Time Signal Processing.* Prentice-Hill, 1989.

[69] A. Peterson, S. Ray, and R. Mittra, *Computational Method for Electromagnetics.* IEEE Press, New York, 1998.

[70] M. Gupta, Ed., *Electrical noise: fundamentals and sources.* IEEE Press, New York, 1977.

[71] B. Souny, “Etude de la protection électrostatique d’un réseau de trois antennas du type Kathrein,” Rapport d’étude pour DGAC-DSNA-DTI, ENAC/LETA, 2007.

TITLE :

Study of corona discharges on VHF antennas caused by a natural electrostatic field

---

SUMMARY :

In civil aviation, communications between pilots and air trafic controllers are of primary importance. A jamming has been experienced on ground stations working in the VHF frequency-band (118-134 MHz). This has impaired air-ground communications. This phenomenon is due to Corona discharges occurring on the antenna pylon when there is a strong ambient electrostatic field. The aim of this PhD is to develop a model to predict the noise on the antenna induced by corona discharges, for a given geometry and ambient field.

Firstly, we localize the places where corona discharges most likely occur via an electrostatic simulations. Then, we propose and validate an elementary dipole model to represent the radiation of corona discharges in the frequency domain. Finally we evaluate the interference introduced by corona discharges at the antenna ports by means of simulations in the frequency domain. The simulation results are compared with measurements.

KEY WORDS : Corona discharge, VHF antenna, Interference

AUTEUR : Mingtian WANG

TITRE :
Etude des décharges corona sur des antennes VHF soumises à un champ électrostatique naturel

DIRECTEUR DE THESE : Jean-Pierre BŒUF et Alexandre CHABORY

LIEU ET DATE DE SOUTENANCE : Amphithéâtre Boucher, ENAC, le 3 avril 2014 à 10h30

RESUME

En aviation civile, les communications entre pilotes et contrôleurs aériens sont d'une importance primordiale. Un brouillage a été observé sur des stations sol fonctionnant dans la gamme VHF (118-134 MHz), qui a perturbé les communications air-sol. Ce phénomène est dû à des décharges corona qui se produisent sur le pylône lors d'un fort champ électrostatique ambiant. Le but de cette thèse est de développer un modèle pour prédire le bruit dû aux décharges corona pour une géométrie et un champ ambiant connus.
Premièrement, nous localisons les lieux où les décharges se produisent le plus probablement via des simulations électrostatiques. Puis, nous proposons et validons un modèle de dipôle élémentaire pour représenter le rayonnement des décharges. Enfin, nous évaluons les niveaux d'interférence introduits par les décharges corona aux ports des antennes au moyen de simulations dans le domaine fréquentiel. Les résultats de simulation sont comparés avec des mesures.

MOTS-CLES : Décharge corona, Antenne VHF, Interférence

DISCIPLINE ADMINISTRATIVE : Electromagnétisme et Systèmes Haute Fréquence

---

INTITULE ET ADRESSE DE L'U.F.R. OU DU LABORATOIRE :

TELECOM/EMA, ENAC
7, Avenue Edouard Belin
31055 Toulouse Cedex 4